Politecnico
di Torino

Department of Applied Science and Technology
Master's Degree in "Physics of Complex Systems"

Master's Thesis

developed at the Department of Science and Industry Systems,
University of South-Eastern Norway,
Kongsberg

SEMICLASSICAL ANALYSIS OF VOLTAGE-BIASED SERIES OF TWO JOSEPHSON JUNCTIONS: ATTRACTORS AND CHAOS.

Supervisors:	Candidate:
Prof. Vittorio Penna	Davide Stirpe
Prof. Francesco Pietro Massel	

Academic Year 2022-2023

Abstract

The main purpose of this thesis is to analyze the superconducting phase dynamics emerging from a semiclassical description of a superconducting circuit composed of two Josephson junctions in series, in the presence of an external voltage source. The topology of the circuit identifies two superconducting leads and a central superconducting island, whose phase is the only one evolving in a non-trivial way. The semiclassical Lagrangian is derived from the lumped element description of the superconducting circuit and, consequently, the Hamiltonian and the equations of motion are obtained. The external voltage's presence is considered by implementing a constrained Lagrangian in which the voltage is considered a constraint. Further algebraic manipulations of the equations of motion lead to a non-linear second-order differential equation controlling the evolution of the superconducting phase of the system. The Resistively and Capacitatively Shunted Junction model has been used to take account of non-superconducting phenomena, such as quasiparticle excitations, by introducing the dissipation in the system.

The dynamical equation of the superconducting phase can be easily mapped into the dynamical equation of a vertically and periodically driven rotor, i.e. a zero-gravity Kapitza pendulum: the correspondence between the dimensionless dynamical parameters of the two problems are drawn. The connection between mechanical pendulums and JJ-based superconducting circuits is something that has been already discussed in the literature, but the discussion seems to be focused just on the relation existing amid the single voltage-biased Josephson junction and the force-driven pendulum. As far as it is known, no correspondence between a superconducting circuit like the one under analysis in this thesis and the Kapitza pendulum has been derived before. This mechanical system exhibits a wide dynamical landscape comprised of different attractors when it is analyzed in terms of the gravitational and driving amplitude parameters.

Numerical simulations are performed to find solutions and attractors of the dynamical equation. The different physical nature of KP and SC suggest to choose a parameters space comprised of the dimensionless driving amplitude and the initial condition for the superconducting phase, differently from what is usually done for KP. The characteristic KP attractors have been detected and their distribution in the stability diagrams has been found. The attractors generate regions having a clear fractal geometry, showing sensitivity to initial conditions, emblematic of chaos. Moreover, the limit-cycles solutions present variability in terms of the number of nods, known as multiple-nodding behavior, showing a very intricate internal chaotic structure in the stability diagram: Hausdorff's dimensions of these regions have been computed, revealing that they have non-integer values. In the end, the regime of validity of such a semiclassical regime has been discussed, comparing the superconducting circuit with the superconducting Single Electron Transistors (SSET), two devices having the same lumped element description. What has been found is that, in order to observe the semiclassical phase dynamics the regime has to be opposite to the one in which SSETs operate.

Contents

List of Figures

List of Tables

List of abbreviations

1. **JJ**
   Josephson junction
2. **KP**
   Kapitza pendulum
3. **SC**
   Superconducting circuit under analysis: voltage-biased series of two Josephson junctions
4. **RCSJ**
   Resistively and Capacitatively Shunted Junction model
5. **SET**
   Single Electron Transistor
6. **SSET**
   Superconducting SET
7. **SQUID**
   Superconducting Quantum Interference Device
8. **EOM**
   Equation Of Motion

Chapter 1

Introduction

1.1 Superconductivity and superconducting circuits

Superconductivity is one of the most studied fields in Physics. The first experiments suggesting the existence of this phenomenon were carried out in Leiden Laboratory by Onnes and they were focused on low-temperature experiments on Hg. The scientist found out that the metallic resistance vanishes at very low temperatures, and, at first glance, it seemed to confirm the Drude hypothesis of resistivity dropping at low T due to an inefficient electron-lattice interaction. However, the experiments revealed that the resistivity behaviour is ohmic up to a specific temperature value T_c, called critical temperature, below which the resistivity abruptly drops to values very close to zero: this suggested the presence of a phase transition. In the following years, different superconducting metals and many effects related to superconductivity were discovered: one was the Meissner effect (Meissner and Ochsenfeld [1933]), consisting of the magnetic field extrusion from the metal when the temperature is below the critical one, and the Isotope effect, giving the dependence of the critical temperature on the mass of the metal. In 1935, Fritz London suggested a phenomenological theory describing the Meissner effect(London and London [1935]), then extended by Landau-Ginzburg (Ginzburg et al. [2009]), in which for the first time superconductivity was described as a "macroscopic observation of quantum laws". Only in 1957, a microscopic theory describing superconductivity was successfully introduced by Bardeen, Cooper and Schrieffer (Bardeen et al. [1957]): it was called BCS theory in honour of its authors. It claims that, when the temperature is below a (metal-dependent) threshold value, the electrons in the metal couple to form Cooper pairs (CPs), couples of electrons with opposite spins and momenta, having zero total spin and obeying the Bose-Einstein distribution. The mechanism producing the pairing between electrons at low temperature was proposed by Fröhlich [1950] and it is due to the fact that the electron-phonon interaction acts as an apparent electron-electron interaction for those electrons lying within an energetic shell close to the Fermi energy level. In the electronic ground state, CPs have a characteristic size (distance between the electrons) close to the superconducting correlation length $\xi \simeq 10^{-4}$cm, giving as a result large overlapping among CPs wave functions and a condensate of CPs. The

BCS theory is a powerful model that gives a good estimation of the critical temperature, the temperature dependence of the superconducting energy gap, the derivation of the Isotope effect and many other interesting features of superconductivity. Among these phenomena, Josephson effect is one of the most studied and the one with the largest applicability. This effect, observable when the distance between two superconducting electrodes is $d < 10^{-5}$cm, describes the experimental observation of CPs tunnelling from one electrode to the other with non-zero probability, in such a way to produce a superconducting current (in short, super-current), even when no external electric or magnetic field are applied: The mathematical description of this phenomenon was proposed by Josephson in 1962 and, for this reason, it was renamed as Josephson effect (Josephson [1962]).

The phenomenon of CPs tunnelling can be controlled in a device called Josephson junction (JJ), comprised of two superconducting electrodes delimited by a thin insulating material, i.e. a dielectric material, forming a superconducting-insulating-superconducting junction (SIS in short). It can be described by an equivalent circuit comprised of an intrinsic capacitance in parallel to a non-linear inductor, called Josephson element: the constitutive equations of the JJs are called Josephson relations. The JJ is the main ingredient of the so-called superconducting quantum circuits, devices in which macroscopic quantum effects are observable. These devices have become of great interest in the last thirty years due to their wide flexibility and applicability. Indeed, JJ-based circuits can be exploited, for instance, in quantum computation and quantum information (for instance, see Arute et al. [2019], Blais et al. [2020]), in microwave photonics (Gu et al. [2017]) and they can be applied in many different fields of physics, such as experiments concerning fundamental quantum mechanical laws (Tomaszewski et al. [2018]), JJs array for condensed matter theory experiments (Martinoli and Leemann [2000], Cataliotti et al. [2001]), sensing and metrology (Fagaly [2006]). The widespread application of JJs is essentially due to several different reasons. First, the JJ-based superconducting circuits have macroscopic physical dimensions and they can operate at milli-Kelvin temperatures and they can be easily combined with resistances, inductors or capacitors. Second, they have discrete anharmonic energy levels, allowing the superconducting circuits to behave like atoms: for this reason, the superconducting circuits are called superconducting artificial atoms. The greatest advantage of using JJs is that the energetic levels of a superconducting circuit can be tuned much more easily than the real atoms case. The JJs parameters can be tuned through the application of external voltages, currents or electromagnetic fields, making them ideal for a wide range of experiments and research. The anharmonicity of the energetic level is a crucial aspect of the superconducting circuits and it is a direct consequence of the non-linearity of the JJs, i.e. it is considered as a non-linear inductor. This non-linearity brings a non-equally spaced energetic spectrum for the superconducting circuits, making them suitable for the implementation of quantum bits (qubits), the quantum information units. The specific topology of these qubits determines the difference between designs, such as charge (Pashkin et al. [2009]), flux (Steffen et al. [2006]) and phase (Martinis et al. [2002]) qubits. The implementation of such devices requires a fully quantum control of the JJs non-linearities, in the sense that the anharmonic energy levels need to be quantized in order to realize a qubit. However, it is possible to observe interesting consequences of the non-linear JJs dynamics even at the semiclassical level, like

in the case of the Aharonov-Bohm effect (Aharonov and Bohm [1959]).
More details about the JJs, qubits and superconducting circuits are reported in Chap.2.

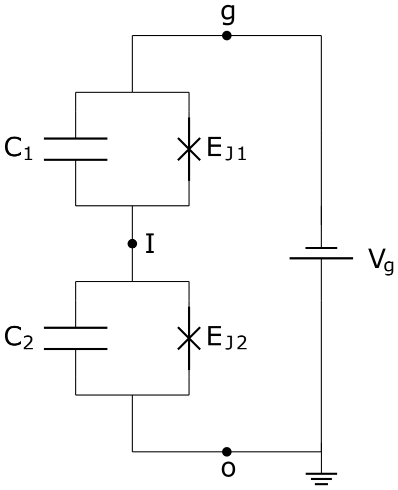

Figure 1.1: Superconducting circuit composed by two JJs in series, linked to an external voltage source.

The semiclassical analysis of superconducting circuits is a crucial aspect of this work. This thesis aims indeed to perform a semiclassical analysis of a particular superconducting circuit. This device is composed of two S-I-S JJs in series, linked to an external voltage source V_g. A schematic representation of the circuit under analysis in this thesis (in short SC throughout the text) is reported in Fig. 1.1. In this circuit three relevant nodes have been highlighted: g and o, representing two superconducting leads while the electrode I can be considered as a superconducting island surrounded by insulating materials. The semiclassical Lagrangian and Hamiltonian description of the lumped description of the SC (obtained following what done in Girvin [2011], Vool and Devoret [2017]), involving the flux and the voltage as Lagrangian variables, have a kinetic contribution due to the intrinsic capacitances and the potential is given by the Josephson elements energies. The procedure for taking into account the external voltage in the EOMs is slightly different from the standard treatments, like the one proposed by Devoret (Vool and Devoret [2017]), since here the Lagrangian is considered as constrained by the voltage through the introduction of a Lagrangian multiplier. The equations of motion (EOMs) will lead to a non-linear second-order differential equation describing the time evolution of the island phase.
The semiclassical treatment of the SC is discussed in Chap. 3.

The emergence of the non-linearities of the phase at semiclassical level requires the control of the physical parameters of the system. In particular, the modulation of the single electron charging energy E_C and Josephson energy E_J is important to control the working regime of the circuit. The ratio between these two quantities contributes to the characteristic impedance $\mathcal{Z} \simeq \sqrt{\frac{E_J}{E_C}}$ of the circuit. One can easily recognize that the topology of the SC is equivalent to one of a superconducting single electron transistor (SSET), i.e. they

share the superconducting lead-island-lead structure. The usual working regime of a SSET is ideal for implementing single-CP pumps or, in general, superconducting circuits exploiting single-CP effects: a SSET operates in Coulomb blockade regime, reached for an impedance $\mathcal{Z} \gg R_K$ much larger than the resistance quantum. The semiclassical analysis abovementioned requires control of the non-linearity of a SSET at the level of the phase, formally conjugated to the charge. Thus, the ideal framework in which the phase dynamics could be observed is different from the Coulomb blockade: when the characteristic impedance $\mathcal{Z}$ is lower than the resistance quantum, the phase of the system can have low uncertainty, at the expenses of the charge. This could represent the ideal semiclassical regime in which the non-linear phase dynamics could be observed in a SSET.
The regime of validity of the semiclassical analysis is discussed in Sec. 2.5.

1.2 Kapitza pendulum dynamics

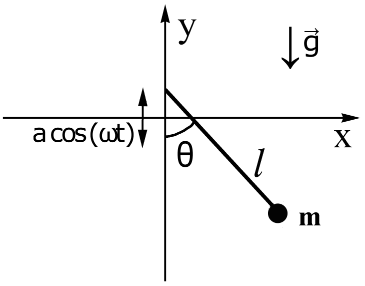

Figure 1.2: Schematic representation of a Kapitza pendulum exposed to gravity with vertical pivot oscillation.

The dynamical equation ruling the semiclassical evolution of the superconducting phase can be easily mapped into the equation of a zero-gravity Kapitza pendulum (KP). This mechanical device is a rigid rod of length l, having a mass m attached to the free end, while its pivot is forced to oscillate periodically along the gravity direction $\vec{g}$ (see Fig. 1.2): θ is the angle measured from the reference gravity direction The pivot oscillates periodically with a driving amplitude a and a driving frequency ω, whereas $\omega_0 = \sqrt{\frac{g}{l}}$ is the proper frequency. The correspondence between the SC and the KP is discussed in Chap. 4.

The KP represents a generalization of the simple pendulum and it exhibits intricate and chaotic dynamics: the literature on this theme is quite rich. Their dynamics have some similarities, such as the presence of a stable attractor at $\theta = 0$, but for some particular values of the driving frequency and amplitude, the inverted position $\theta = \pi$ becomes stable, whereas it is always unstable for the simple pendulum. The stabilization of the inverted position in the KP has been studied through the so-called dynamic stabilization proposed by Stephenson [1908], which ensures that a high-frequency pivot oscillation is needed to stabilize the inverted position. A more rigorous analytical argument has been proposed by Kapitza [1951], where he operates a separation of the angular motion in slow and fast components, averaging then with respect to the fast motion. This procedure leads to a dynamical equation for the slow component showing an effective potential which acquires two minima, at the normal and inverted position, for a particular range of the dynamical parameters. More recent works have improved the dynamical stabilization given by Kapitza by focusing on the behavior of the solutions in terms of the dimensionless driving amplitude $m = \frac{a}{l}$ and the dimensionless gravity $k = \frac{\omega_0^2}{\omega^2}$. For instance, in Butikov [2011], the Kapitza's dynamical stabilization has been improved and upper and lower boundaries of the region of stability are derived, in the diagram m-k, for the inverted position. Another interesting way to stabilize the inverted position is through the friction: in Bartuccelli et al. [2001], it has been proved a theorem stating that the presence of a small damping factor, along with a small driving amplitude, can prevent the KP from falling to the normal position, stabilizing the inverted one. The KP can be also trapped in periodic oscillations around the fixed point, forming trajectories called limit-cycles. These attractors have been observed in many works related to KP dynamics (see, for instance, Bartuccelli et al. [2002], Butikov [2002]). In the latter, the limit-cycles are explained in terms of the parametric resonance: when two driving cycles occur during an integer number of natural KP oscillations, the driving supplies the system with energy, compensating the damping caused by the friction and locking the pendulum in a periodic oscillation around the inverted position. The physical structure of these trajectories is strongly related to the concept of nod. In Acheson [1995], a nod is defined as a point of the trajectory, analyzed by an observer moving as the pivot, in which the pendulum inverts its motion. He shows that these limit-cycles have a multiple-nodding behavior, i.e. different values of dynamical parameters give limit-cycles with different numbers of nods. In this and many other works, it has been observed that KP give rise to a large family of such multiple-nodding trajectories. In Acheson's work, double-nodding has been detected, meaning that this kind of trajectory nods twice in each half-side of the periodic oscillation. Triple-nodding trajectories have been also detected and the existence of quadruple-nodding has been discussed but not formally derived. However, it is known that no upper limit in the multiple-nodding behavior exists: higher orders of multiple-nodding have been detected by Bartuccelli et al. [2001], but the explicit multiple-nodding description has not been given.

The non-linearity of the mechanical KP gives rise to remarkable chaotic dynamics which have made the KP the reference system for investigating the chaos. In many works, the emergence of chaos has been studied in terms of the dimensionless driving amplitude m and the dimensionless frequency k: within this dynamical picture, the system exhibits strong sensitivity to the initial conditions. This property is highlighted by fractal basins of attraction, non-zero Lyapunov exponent (see Bartuccelli et al. [2001]), intricate stability diagrams (see Carbo et al. [2010]) and other phenomena related to chaos such as bifurcation and period-doubling (Kim and Hu [1998]).

1.3 Dynamics of the superconducting circuits

The semiclassical analysis of the superconducting circuits has been already carried out and, even in this case, the literature related to this theme is quite rich. Indeed, superconducting circuits can exhibit chaotic dynamics due to the non-linearity of the JJs. However, the study of the chaos in the dynamics of JJs seems to be mainly focused on superconducting devices composed of a single JJ.

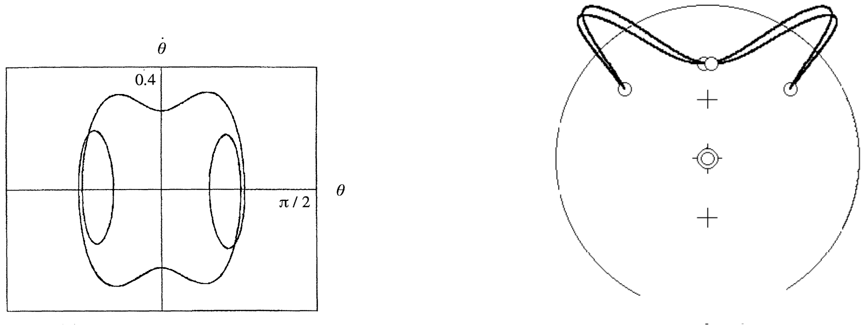

(a) (b)

Figure 1.3: Example of a limit-cycle trajectory around the inverted position of the KP, taken from Butikov [2002]. According to Acheson's definition, it is a double-nodding limit-cycle. (a) Trajectory in the phase-space; (b) physical representation of the limit-cycle observed from a fixed observer.

In addition, these single JJ circuits behave, from the dynamical point of view, as a simple pendulum driven by an external time-dependent force. Single JJ devices have been used for sensing (Golod et al. [2010]) or for high-frequency chaos generation in communications (Dana et al. [2001]). The damped and driven simple pendulum is a dynamical problem showing various attractors and chaotic dynamics. Indeed, the single JJ dynamics exhibits chaotic stability diagrams, bifurcation and period-doubling (Zhang et al. [2011]), fractal basin of attraction (Gwinn and Westervelt [1986]) and chaotic Hopf bifurcations leading to limit-cycles (Sobolewski et al. [1988]) and stability diagrams showing strong sensitivity to the initial conditions (Iansiti et al. [1985]).

The analysis performed in this thesis differs from this body of work because the superconducting circuit considered here is composed of two JJs in series and its superconducting phase is described by a dynamical equation that can be mapped into the one of a zero-gravity KP. As far as it is known, the correspondence between such a device with the KP has not been drawn before, since no trace has been found in the dedicated literature. What has been done then is to analyze, through numerical integration of the dynamical equation, the dynamics of the superconducting phase of the SC for different values of the phase initial condition in terms of the external voltage V_g, through the dimensionless amplitude $\bar{\epsilon}$, in such a way to investigate how the voltage affects the island super-current. The parameters space used in this description differs from the one typically used for KP, since its dynamics and attractors are mainly studied in terms of gravity (no gravitational counterpart is present in the SC equation) and driving amplitude. The attractors emerging from the dynamical equation are essentially the same as KP — 0-stable, π-stable, unstable and limit-cycle — even if they exhibit an intricate and fractal distribution in the parameters space, forming different regions having a particularly fractal geometry and showing sensitivity to initial condition. In addition, the limit-cycles show a wide picture of multiple-nodding solutions, allowing the identification of sub-regions in the stability diagram. The estimation of Hausdorff's dimension

of regions and sub-regions related to the attractors has been performed to have more insights into the chaoticity and the sensitivity to initial condition of such dynamics.
All the details about the numerical simulations, the dynamics and the chaotic stability diagram are discussed in Chap. 5.

Chapter 2

Superconducting circuits

2.1 Josephson junction

The Josephson effect can be observed when two superconducting electrodes are placed at a distance $d < 10^{-5}$cm. In that situation, CPs can eventually tunnel from one electrode to the other with a non-zero probability of producing a superconducting current (in short, super-current). The latter, under the physical condition fixed above, depends only on the difference $\varphi = \varphi_1 - \varphi_2$ between the phases of the two wave functions $\psi_1 = N_1 e^{i\varphi_1}$ and $\psi_2 = N_2 e^{i\varphi_2}$ describing the two superconducting electrodes. The explicit dependence between the super-current and ϕ is sinusoidal and its expression represents the first Josephson relation:

$$I_{\mathrm{s}} = I_{\mathrm{c}} \sin\left(\varphi\right), \tag{2.1}$$

where I_{c} is the Josephson critical current. No external electric field is needed to produce such a current. Instead, when an external voltage is applied across the two electrodes, the phase difference of the system acquires a linear dependence on the voltage $\mathcal{V}$: the explicit formula gives the second Josephson relation

$$\dot{\varphi} = \frac{(2e)}{\hbar}\mathcal{V} = \frac{2\pi}{\Phi_0}\mathcal{V}, \tag{2.2}$$

where $\Phi_0 = \frac{(2e)}{h}$ is the superconducting quantum of flux.

The Josephson effect can be exploited to implement specific superconducting device called Josephson junctions (JJs). The S-I-S junctions (SIS stands for superconducting-insulator-superconducting) are characterized by a dielectric layer between the two electrodes, usually oxide such as aluminium oxide. This configuration of the superconducting electrodes produces a potential barrier that the CPs need to overcome in order to tunnel the barrier and produce a super-current: these two physical phenomena observed in the JJ require a lumped element representation given by a capacitor (resembling the parallel plate capacitor formed by the two electrodes) in parallel with a nonlinear inductor (modelling the super-current), as reported in the Fig. 2.1. From the classical electromagnetic theory, it is known that a normal inductor is characterized by a linear response function between the flux across that element and the current flowing in it. At the level of the JJ, following what is done in Vool

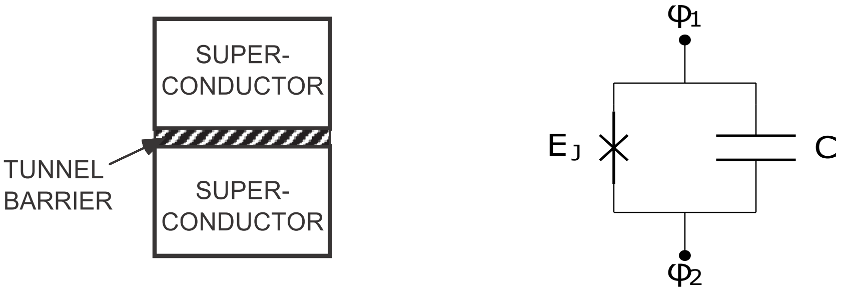

Figure 2.1: On the left: schematic representation of three different components of a JJ, respectively from the top one superconducting electrode, a dielectric tunnel barrier and again a superconducting electrode. On the right: CJ model for a JJ, where a nonlinear inductor and a capacitor describe respectively the superconducting current and the charge storage measures in a JJ.

and Devoret [2017], the flux across the junction can be related to the voltage across the junction through the definition $\phi(t) = \int_0^t dt' v_J(t')$, giving

$$v_J(t) = \dot{\phi}(t), \tag{2.3}$$

and thus, exploiting the second Josephson relation, $\dot{\varphi}(t) = \frac{2\pi}{\Phi_0} v_J = \frac{2\pi}{\Phi_0}\dot{\phi}(t)$ one obtains that

$$\phi = \frac{\Phi_0}{2\pi}\varphi, \tag{2.4}$$

i.e. phase is proportional to the flux through a proportionality constant $2\pi/\Phi_0$. From this result rewrite the second Josephson relations in $I = I_C \sin\left(\frac{2\pi}{\Phi_0}\phi\right)$. For small flux, the Josephson element behaves like a classical linear inductor, due to the first order expansion $I = \left[\frac{2\pi I_C}{\Phi_0}\right]\phi = L_J^{-1}(0)\phi$, which gives the expression of the Josephson inductance $L_J(0) = \frac{\Phi_0}{2\pi I_C}$. The energy of the Josephson element is then given by

$$U_{\mathrm{J}}(\phi) = -E_{\mathrm{J}}\cos\left(\varphi\right), \tag{2.5}$$

not quadratic as the linear inductor case. The prefactor E_J represents the Josephson Energy, the parameters controlling the CPs tunnelling strength in a JJ. The critical current I_J and the Josephson energy E_J are related through the formula $E_{\mathrm{J}} = \frac{\Phi_0}{2\pi} I_{\mathrm{c}}$.

Even though superconductivity is a phenomenon macroscopically measurable, its intrinsic nature is purely quantum. Therefore, the derivation of the Josephson relations in Eqs. (2.1)-(2.2) and the Josephson element's energy in Eq. (2.5) requires the application of quantitative quantum mechanical arguments. In the following discussion, the derivation of the Josephson relations and the Josephson energy is provided, following what has been done in Vool and Devoret [2017], Girvin [2011], Kockum and Nori [2019]: the details are reported in Appendix A.

Here, for the sake of simplicity, an isolated Josephson junction is considered, like the one sketched in Fig. 2.1. Considering the discussion made above about superconductivity, the ground state of the system is composed of a macroscopic CPs condensate that drastically reduces the number of degrees of freedom needed to describe the system, allowing thus to use the CPs number on the two superconducting electrodes $N_1(t)$ and $N_2(t)$ as dynamical variables. From the fact that the junction is isolated, it is obvious that $N_{tot} = N_1(t) + N_2(t)$ is a conserved quantity. Therefore, the difference $N(t) = N_1(t) - N_2(t)$, describing the number of tunnelled CPs, can be exploited as a degree of freedom describing the tunnelling process through the junction. Consequently, The total amount of charge tunnelled through the junction is simply given by $Q(t) = (-2e)N(t)$. Introducing a quantum mechanical description simply means promoting the physical observables to operators and defining a proper set of states describing the system's configurations in terms of the degrees of freedom. Thus, in this case, $|m\rangle = |N_1 - m, N_2 + m\rangle$ is the state describing the tunnelling of m CPs through the barrier, forming a basis $\{|m\rangle\}_{m\in\mathbb{N}}$. Consequently, the physical operators can be decomposed on that basis. For instance, the CPs number operator $\hat{N}$ can be written in such a basis as $\hat{N} = \sum_{m=0}^{\infty} m|m\rangle\langle m|$, i.e. the states $|m\rangle$ are eigenstates of such a number operator. The Hamiltonian describing the superconducting tunnelling process can be taken to be equivalent to the one describing the nearest-neighbour hopping in a 1-dimensional lattice. Taking such a Hamiltonian becomes a reasonable approximation whether just the single CP tunnelling is considered, neglecting higher-order contributions. Therefore, it is reasonable to describe the junction with a two-site 1-dimensional lattice and the CP's tunnelling with the Tight-Binding hopping Hamiltonian

$$\hat{\mathcal{H}} = -\frac{E_J}{2}\sum_m |m+1\rangle\langle m| + |m\rangle\langle m+1|, \tag{2.6}$$

in such a way to describe the tunnelling of a single CP only from left to right or vice-versa: $|m+1\rangle$ is the state indicating that one CP has been tunnelled from the top electrode to the bottom one. Introducing a proper phase operator in this single-mode system is not completely straightforward. It has been proved by Susskind and Glogower [1964] that, whether the number operator has an integer positive spectrum, its conjugated phase operator does not exist. Several different expedients have been suggested in order to avoid this. In the work mentioned above, the trigonometric operators

$$\cos(\hat{\varphi}) = \frac{1}{2}\left[\hat{e}^{i\varphi} + \hat{e}^{-i\varphi}\right] \tag{2.7}$$

$$\sin(\hat{\varphi}) = \frac{1}{2i}\left[\hat{e}^{i\varphi} - \hat{e}^{-i\varphi}\right] \tag{2.8}$$

have been introduced, considering $\hat{e}^{\pm i\varphi}$ as symbolic expressions not representing the exponentiation of a true phase operator. Another interesting solution is the one suggested in Pegg and Barnett [1989], consisting in the definition of phase states related to a number operator defined on a reduced $s+1$ space, taking then s in the infinite limit:

$$|\varphi\rangle = \lim_{s\to\infty}\frac{1}{(s+1)^{1/2}}\sum_{m=0}^{s} e^{in\varphi}|m\rangle. \tag{2.9}$$

In this space, the operators in Eqs.(2.7)-(2.8) are exponentials of the Hermitian operator $\hat{\varphi}$ and they plays the role of lowering and raising operators: $e^{\pm i\varphi}|m\rangle = |m \pm 1\rangle$ The states (2.9) are the eigenstates of the Hamiltonian (2.6). This can be shown by defining on-site creation and destruction operators $a_1, a_1^\dagger$ and $a_2, a_2^\dagger$ acting on the single-site wave functions. The Hamiltonian can be rewritten as

$$\hat{\mathcal{H}} = -\frac{E_J}{2\sqrt{N_1 N_2}}\left[\hat{a}_1^\dagger \hat{a}_2 + \hat{a}_1 \hat{a}_2^\dagger\right]. \tag{2.10}$$

The application of the Hamiltonian to the phase states Eq. (2.9) gives the cosine operator

$$\hat{\mathcal{H}}|\varphi\rangle = -E_J\left[\frac{e^{i\hat{\varphi}} + e^{-i\hat{\varphi}}}{2}\right]|\varphi\rangle = -E_J\cos(\hat{\varphi})|\varphi\rangle \tag{2.11}$$

and, consequently, the eigenvalues of this operator represent the Josephson element's energy given in Eq.(2.1).

The First Josephson Relation establishes the phase-current response function of a JJ. It can be derived by defining the current operator $\hat{I} = (-2e)\dot{\hat{N}}$, where $\hat{N}$ evolves accordingly to the known Heisenberg equation

$$i\hbar\dot{\hat{N}} = \left[\hat{N}, \hat{\mathcal{H}}\right] = \left[\hat{N}_1, \hat{\mathcal{H}}\right] - \left[\hat{N}_2, \hat{\mathcal{H}}\right] \tag{2.12}$$

which gives the final expression for the current operator

$$\hat{I} = \frac{2\pi E_J}{\Phi_0\sqrt{N_1 N_2}}\left[\frac{\hat{a}_1^\dagger \hat{a}_2 - \hat{a}_1 \hat{a}_2^\dagger}{2i}\right] = \frac{I_C}{\sqrt{N_1 N_2}}\left[\frac{\hat{a}_1^\dagger \hat{a}_2 - \hat{a}_1 \hat{a}_2^\dagger}{2i}\right] \tag{2.13}$$

Again, the application of this operator to the phase states reveals the sine operator

$$\hat{I}|\varphi\rangle = I_c\left[\frac{e^{i\hat{\varphi}} - e^{-i\hat{\varphi}}}{2i}\right]|\varphi\rangle = I_c\sin(\hat{\varphi})|\varphi\rangle, \tag{2.14}$$

whose eigenvalue equation gives the First Josephson relation.

When an external electric field is applied to the junction, for instance through the application of a constant voltage V, the linear term $U = -(2e)\mathcal{V}\hat{N}$, measuring the Coulomb force exerted on the CPs, appears in the Hamiltonian. This term makes the cosine operator not commuting with Hamiltonian. The Heisenberg equation for the cosine operator gives the time evolution of the phase operator

$$i\hbar\frac{d}{dt}\cos(\hat{\varphi}) = \left[\cos(\hat{\varphi}), \hat{H}\right] = -(2e)\mathcal{V}\left[\cos(\hat{\varphi}), \hat{N}\right] \rightarrow \dot{\hat{\varphi}} = \frac{2\pi}{\Phi_0}\mathcal{V}, \tag{2.15}$$

which represents, in the end, the Second Josephson relation.

2.2 Quantization of a circuit: the Cooper Pairs box

The Josephson relations (2.1)-(2.2), related to the Josephson element which models the super-current of Cooper Pairs (CPs) in the JJ, has been proved through a phenomenological quantization procedure. The proper way to quantize a circuit consists of a standard mathematical procedure suggested in Girvin [2011], Kockum and Nori [2019]. The starting point is writing down the Lagrangian, then deriving the Hamiltonian and, in the end, applying the standard quantization. In particular, the passage from the Lagrangian to the Hamiltonian in the case of voltage-biased circuits has been provided through a mathematical standard procedure developed by Devoret in Vool and Devoret [2017], which will be discussed shortly in this section, but the extended calculations are in Appendix 2.2. Here, this standard Lagrangian and Hamiltonian formalisms will be implemented, as an example, the Cooper pairs box (CPB) (see Fig. B). The quantization of its Hamiltonian will become the starting point for the general discussion about the superconducting qubits. First, in order to write down the Lagrangian of the circuit, the individuation of meaningful nodes in the circuit is required. In the lumped element description of the CPB, the reference nodes are 1 and 2 across the gate capacitor C_{g}, indicated with the corresponding fluxes ϕ_1 and ϕ_2: they have been taken as generalized coordinate variables in the Lagrangian formalism. They are defined in such a way that the flux of node i is directly related to the node voltage v_i through the Eq. (2.3) and the phase is directly related to the flux through Eq. (2.4): explicitly, $\dot{\phi}_{\mathrm{i}}(t) = v_{\mathrm{i}}(t)$ and $\varphi_{\mathrm{i}} = \frac{2\pi}{\Phi_0}\phi_{\mathrm{i}}$ with $i = 1, 2$. The potential term in the CPB's Lagrangian is the energy of the Josephson element $\mathcal{U} = -E_{\mathrm{J}} \cos\left(\frac{2\pi}{\Phi_0}\phi_2\right)$. Following Devoret's procedure, the voltage source is substituted with an ideal zero-impedance capacitor C_{A} and then, after the passage from the Lagrangian to the Hamiltonian, its capacitance will be taken in the infinite limit. Thus, the kinetic part of the Lagrangian, i.e. not taking into account the Josephson element, can be described by the circuit reported in Fig. 2.3. The Lagrangian kinetic term relies on three contributions coming from the capacitors. Explicitly:

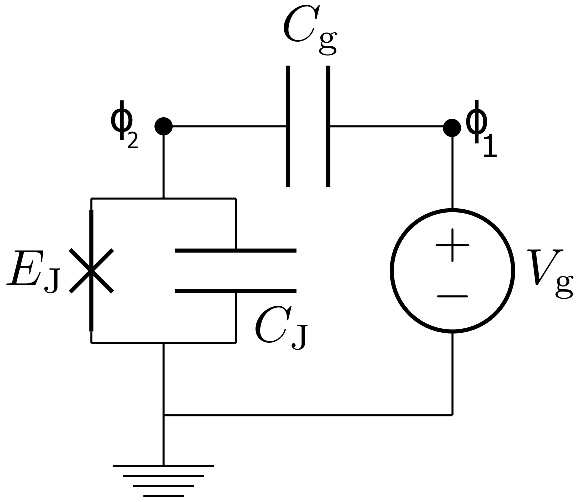

Figure 2.2: Circuit describing the CPB. V_g is a direct voltage source,C_g is the gate capacitor and the last element represents the JJ: C_J models the intrinsic capacitance, while E_J defines the non-linear Josephson element. ϕ_1 and ϕ_2 indicated the fluxes of the two reference nodes 1 and 2.

$$\begin{aligned}\mathcal{T} = \mathcal{T}\left(\phi_1, \phi_2, \dot{\phi}_1, \dot{\phi}_2\right) =& \frac{1}{2}C_{\mathrm{A}}\dot{\phi}_1^{\,2} + \frac{1}{2}C_{\mathrm{g}}\left(\dot{\phi}_1 - \dot{\phi}_2\right)^2 + \frac{1}{2}C_{\mathrm{J}}\dot{\phi}_2^{\,2} = \\ & \frac{1}{2}\dot{\vec{\phi}}^T \hat{C} \dot{\vec{\phi}},\end{aligned} \tag{2.16}$$

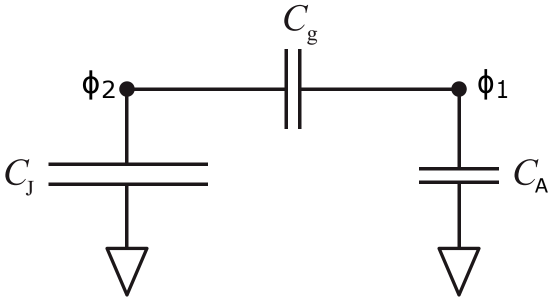

Figure 2.3: Devoret's representation of the CPB circuit: the voltage source is substituted with a zero-impedance capacitor C_A.

where $\vec{\dot{\phi}} = \begin{pmatrix} \dot{\phi}_1 \\ \dot{\phi}_2 \end{pmatrix}$ and $\hat{C} = \begin{pmatrix} C_\mathrm{g} + C_\mathrm{A} & -C_\mathrm{g} \\ -C_\mathrm{g} & C_\mathrm{J} + C_\mathrm{g} \end{pmatrix}$ is the CPB capacitance matrix. The Lagrangian variables conjugated to $\vec{\phi}$ are the charges $\vec{Q} = \nabla_{\dot{\phi}}\mathcal{T} = \hat{C}\vec{\dot{\phi}}$, which can be used to derive the CPB Hamiltonian through the Legendre transformation of the Lagrangian

$$\mathcal{H} = \mathcal{T}(\vec{\phi}, \vec{Q}) - \mathcal{L}(\vec{\phi}, \vec{\dot{\phi}}(\vec{Q})). \tag{2.17}$$

In the end, taking the limit $C_\mathrm{A} \to \infty$, the Hamiltonian converges to the expression

$$\mathcal{H} = 4E_{\mathrm{C}_\Sigma} \left(n_2 - n_\mathrm{g}\right)^2 - E_\mathrm{J} \cos\left(\varphi_2\right), \tag{2.18}$$

given that $E_{\mathrm{C}_\Sigma} = \frac{e^2}{2C_\Sigma}$ represents the electron charging energy for $C_\Sigma = C_\mathrm{J} + C_\mathrm{g}$. The term n_g represents the gate charge, defined as $n_\mathrm{g} = -\frac{C_\mathrm{g} V_\mathrm{g}}{2e}$: the deposition of such a charge is the way in which Devoret's procedure introduces the voltage source in the CPB Hamiltonian. The Hamiltonian can be easily quantized promoting the Hamiltonian conjugated variables to operators, $n_2 \to \hat{n}$ and, more cautiously $\varphi_2 \to \hat{\varphi}$, being aware that in this formalism just periodic functions like $e^{i\hat{\varphi}}$ can be promoted to operators without ambiguity. Then, one can simbolically impose the commutation relation $[\hat{\varphi}, \hat{n}] = i$ and the uncertainty principle $\Delta\varphi\Delta N \geq \frac{1}{2}$. The quantum version of the CPB Hamiltonian is the following one:

$$\hat{\mathcal{H}} = 4E_{\mathrm{C}\Sigma} \left(\hat{n} - n_\mathrm{g}\right)^2 - E_\mathrm{J} \cos\left(\hat{\varphi}\right). \tag{2.19}$$

2.3 Superconducting qubits

The fields in which the JJs play a crucial role are quantum computation and quantum information. Indeed, due to their great versatility, the JJs have been implemented in the design of a specific quantum device called qubit, where the acronym stands for quantum-bit, recalling the concept of binary digit used in classical information theory and in computer science. The latter is known to be a computational binary variable taking exclusively values 0 or 1. A qubit represents a generalization of this concept, in the sense that it consists of a quantum superposition $|\psi\rangle = \alpha|0\rangle + \beta|1\rangle$ of the states $|1\rangle$ and $|0\rangle$, resembling the classical units discussed before. Given the normalization constraint on the complex coefficients $|\alpha|^2+|\beta|^2=1$, the general state $|\psi\rangle$ represents one point on the unitary Bloch sphere (see Fig. 2.4) having states $|0\rangle$ $|1\rangle$ at the opposite poles. Computers based on this technology have the potential to sharply enhance and speed up computations with respect to a classical computer, making crucial contributions in a huge amount of scientific and research fields (see Nielsen and Chuang [2010]).

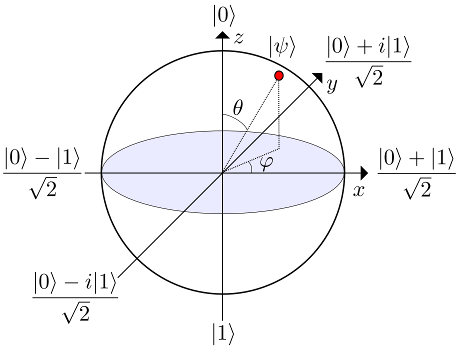

Figure 2.4: Representation of qubits states in the Bloch sphere. A qubit is identified by a wave function given by all the possible linear combinations of the ground state $|0\rangle$ and the first excited one $|1\rangle$ of a two-level quantum system. Given the normalization constraint, the qubit states can be represented as points on a bi-dimensional sphere surface, having states $|0\rangle$ and $|1\rangle$ at opposite poles.

From the physical point of view, the implementation of a qubit requires the isolation of a two-state quantum system composed of the ground state $|0\rangle$ along with the first excited one $|1\rangle$, where these two pure states identify the classical binary states 0 and 1. This characteristic is easily found in the first two atomic energetic levels, which can be isolated from the rest of the energy spectrum due to the nonlinearity of the energetic spectrum, i.e. different transition energies between the levels. However, the manipulation of atomic levels is really hard to perform. The JJ can supply the nonlinearities required for the implementation of a good qubit, along with great tunability of its physical parameters. For this reason, it has become a very useful tool in the realization of qubits, foremost for its anharmonic energy spectrum given by the cosinusoidal potential energy typical of the superconducting tunnelling phenomenon: the energy levels produced within the potential given by Eq. (2.5) do not have the same transition frequencies (see Fig. 2.5) and this allows to isolate the ground and the first excited states.

Their great adaptability allows the JJs to be arranged in many different configurations and the two-state system can be isolated in different ways, depending on which working regime of the JJ is used. The regime in which the JJ operates depends on the Josephson energy E_J and the charging energy E_C related to some relevant capacitance C in the circuit through the characteristic impedance $\mathcal{Z}$ of the JJ, given by the expression (Wendin [2017], Girvin [2011])

$$\mathcal{Z} \sim R_k\sqrt{2\frac{E_C}{E_J}}, \tag{2.20}$$

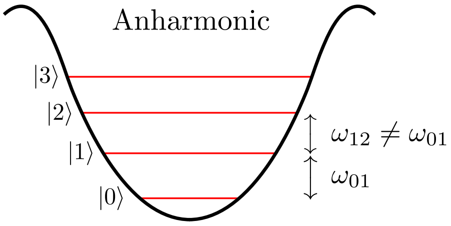

Figure 2.5: The energy levels coming from an anharmonic potential are not equally spaced, meaning that the transition frequencies between adjacent levels are different. This ensures a good isolation of a two-level quantum system, suitable to design a qubit.

where $R_k = \frac{h}{(2e)^2}$ is the superconducting quantum of resistance. When $\frac{E_J}{E_C} \gg 1$, meaning $\mathcal{Z} \ll R_k$, the phase is a well-defined quantity and the charge's number is highly undetermined, whereas for $\frac{E_J}{E_C} \ll 1$, i.e. $\mathcal{Z} \gg R_k$, the regime is opposite and the charge's number becomes undetermined in favour of the phase. Thus, manipulations of that ratio can be used to arrange different circuit designs and architectures in order to reproduce many different JJ-based qubits. A straightforward classification relies upon three main groups indicated in Fig. 2.6 defined, from the left to the right, the charge qubit, flux qubit and phase qubit.

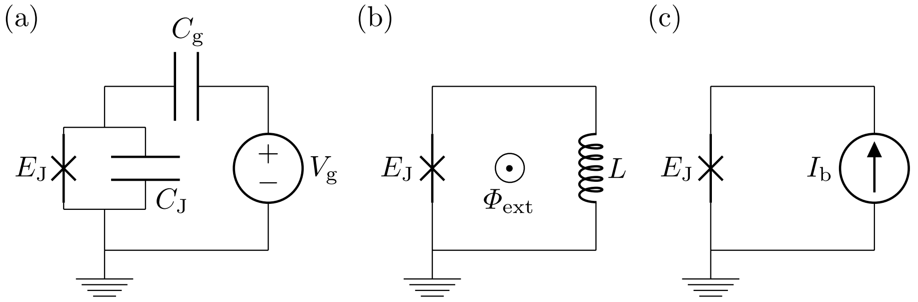

Figure 2.6: Three main qubit design: (a) charge qubit, having same lumped element description of a CPB, (b) flux qubit, controlled by an external flux Φ_{ext} through the inductor L, (c) phase qubit, controlled in current through and external current source I_b.

The charge qubit is one of the first ever implemented superconducting qubits (Pashkin et al. [2009], Duty et al. [2004], Wallraff et al. [2004]) and its circuit is equivalent to a CPB, described by the quantum Hamiltonian (2.19) and sketched in Fig. 2.6a. The latter, when rewritten on the basis of number operator eigenstates, takes the form

$$\hat{\mathcal{H}} = 4E_C \sum_m (m - n_g)^2 |m\rangle\langle m| - E_J \sum_m \left[|m+1\rangle\langle m| + |m\rangle\langle m+1| \right]. \tag{2.21}$$

For $E_J \ll E_C$ (large characteristic impedance $\mathcal{Z}$), the diagonal term becomes dominant and the spectrum is essentially parabolic around one integer value of n_g (see Fig. 2.7a). These energetic levels are essentially periodic in the gate charge's number with a period $\Delta n_g = 1$. The structure of the energy bands depends on the degree of anharmonicity which exponentially decreases with the ratio $\frac{E_J}{E_C}$. Increasing such a ratio, the charge qubit changes its spectrum by becoming a Quantronium (spectrum in Fig. 2.7b and example of application in Vion et al. [2002]), and finally in a Transmon, in Fig. 2.7d (Koch et al. [2007]). The latter shows flattened energetic bands making the Transmon insensitive to charge fluctuations.

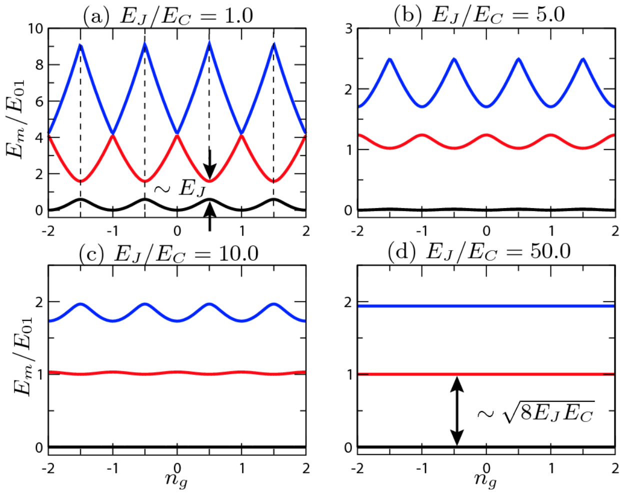

Figure 2.7: The ratio $\frac{E_J}{E_C}$ modulates the anharmonicity of the qubit: the lower the ratio, the higher the anharmonicity. (a) typical spectrum of a charge qubit with $\frac{E_J}{E_C} = 1.0$, (b) The charge qubits can differ for the typical spectrum of a charge qubit, (b) Quantronium spectrum with $\frac{E_J}{E_C} = 5.0$, (c)-(d) Transmon regime for $\frac{E_J}{E_C} = 10.0$ and 50.0. For the Transmon, at the degeneracy points $n_g = n \pm \frac{1}{2}$, where n is some integer, the transition frequency between the ground and the first excited state goes like the Josephson plasma frequency Ω_J.

A flux qubit consists of a large superconducting loop linked to a JJ (see Fig. 2.4b): this prototype of qubit requires an LJ lumped element description, where the loop is a flux-sensitive inductor. Indeed, if the charge qubit is controlled by the external voltage, the flux qubit is tuned by the external flux. In this architecture, the inductance needs to be large in order to isolate a two-state quantum system, giving, on the other hand, huge problems in the maintenance of quantum coherence in the system, a problem still present in all the qubit cases. This can be mitigated by introducing three JJs, two with identical Josephson energy and one having a modulated energy αE_J (Hita-Pérez et al. [2021], Chiorescu et al. [2003]). The spectrum of this kind of qubits presents a good separation of the two lowest energetic levels from the rest of the spectrum, creating effectively a two-level quantum system (Orlando et al. [1999]).

The last prototype of JJ-based qubits is the Phase qubit. It is composed of a very large current-biased JJ, having a very large value of the ratio $\frac{E_J}{E_C}$. In this architecture, the Hamiltonian is (see Martinis [2009])

$$\mathcal{H} = \frac{2\pi}{\Phi_0} \frac{\hbar^2 Q^2}{2C_J(2e)^2} - \frac{\Phi_0}{2\pi} I_b \varphi - E_J \cos(\varphi), \tag{2.22}$$

where I_b is the current bias and the charge on the intrinsic capacitance Q is the momentum conjugated to the phase φ. The degree of anharmonicity of the spectrum is quite low in this configuration, but a two-level quantum system can be created taking just the two lowest energy levels. In addition, this qubit shows to be insensitive to charge noise.

Qubit	C	C_J	E_J/E_C	Z
	fF	fF		Ω
Phase qubit	$0-800$	$\sim 0-6000$	10^4 - 10^6	1.5-15
Flux qubit	0	3	10	450
Charge qubit	0.68	~ 0	0.018	$\sim 10-4$
Quantronium	2.8	~ 0	1.27	1300
Transmon	$15-40$	~ 0	$10-50$	~ 250

Table 2.1: Main qubits designs. The characteristics are taken from Martinis et al. [2002] for the phase qubit, Steffen et al. [2006] for the flux qubit, Pashkin et al. [2009] for the charge qubit, Vion et al. [2002] for the quantronium and Paik et al. [2011] for the transmon.

2.4 SSET and Coulomb blockade

The manipulation of a single electron has become possible in the last decades, giving a strong contribution to metrology and the redefinition of the Ampere in the International System of Units. The Single Electron Transistor (SET) is an example of an electronic device exploiting single electron effects to control a single unitary charge e efficiently. In the same device, when the metals in the electrodes are in a superconductive state, the control of a single CP charge $2e$ is possible: this configuration of the SET is called Superconducting SET (SSET). The latter is interesting in the discussion of this Thesis because the superconducting circuit under analysis in this work (see Fig. 1.1) and the SSET (see Fig. 2.8) share the same lumped element description: in particular, both these devices can be thought as three-island systems. Given that the SSET is a well-studied device, the comparison between these two devices can be exploited to understand in which working regime the SSET exhibits semiclassical dynamics.

As already anticipated, the SSET is a particular case of SET. The latter is a device of two metal-insulator-metal (N-I-N) tunnel junctions with capacitance C_L and C_R, respectively connected to direct voltage sources V_L and V_R. The two junctions delimit a metallic island directly connected to a voltage source V_G, called voltage gate, in series with the gate capacitor C_G. The gate voltage strictly controls the number n of electrons on the island. One electron can eventually tunnel from the island to one of the two metallic electrodes, or it can produce a net current from the right to the left of the device: this current is determined by the voltage difference $V_L - V_R$ between the two electrodes. In

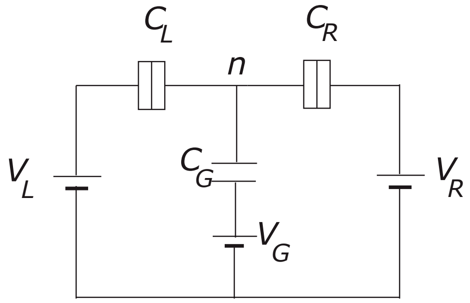

Figure 2.8: Circuit representing a SET or a SSET, depending on the state of the metallic junctions L and R: in the SET the junctions are composed by normal state metals while the junctions in the SSET are comprised of superconducting metals. The figure is taken from Pekola et al. [2013]. A direct comparison with the superconducting circuit under analysis in Fig. 1.1 shows that the two devices have the same lumped element description.

particular, an electron can tunnel through the barrier only if the voltage difference applied to the junction is enough for the electron to overcome the potential barrier between the electrodes, representing the electrostatic repulsion between electrons which prevents the electron from tunnelling: such repulsive energy is the single electron charging energy E_C. Controlling the tunnelling of a single electron requires the E_C to become relevant and this could be achieved, for instance, by taking junctions of small dimensions and low capacitance. When the charging energy takes large values and the system's thermal energy is smaller than the energy level spacing, this can prevent electron tunnelling through the tunnelling junction, producing a configuration called Coulomb Blockade. Considering the tunnelling junction in Fig. 2.9a, the Coulomb blockade regime takes place when the energetic cost $\Delta E = E_f - E_i$ for a positive electron to tunnel through the junction is positive: if a charge $Q = CV$ is already stored, the initial energy of the capacitor is $E_i = \frac{Q^2}{2C}$, but when an electron is transferred from one electrode to the other, the final energy becomes $E_\mathrm{f} = \frac{(Q-e)^2}{2C} = E_\mathrm{i} + E_\mathrm{C} - eV$. Thus, the Coulomb blockade regime holds when $\Delta E > 0 \rightarrow V < \frac{E_C}{e}$, i.e. when the voltage is smaller than a threshold value given by the ratio between the bare charging energy and the electronic charge. Coulomb blockade still holds if the quantum fluctuations are considered, but such energy fluctuations δE need to be smaller than the charging energy. The quantum fluctuations can be derived through the uncertainty inequality $\delta E \cdot \tau \geq \frac{\hbar}{2}$ (see Wasshuber [1997]), where $\tau = R_p C$ is electron relaxation time in presence of a total resistance $R_p = \left(\frac{1}{R_T} + \frac{1}{R}\right)^{-1} \simeq R_T$ given by the parallel of some resistive load R and the normal tunnelling resistance R_T (see Fig.2.9b). Thus, quantum fluctuations are not able to break the Coulomb blockade if

$$R_T > R_e = \frac{\hbar}{e^2} \tag{2.23}$$

i.e. if the normal state tunnelling resistance is larger than the resistance quantum $R_e = 4108\Omega$.

The consideration about the Coulomb blockade regime can be generalized

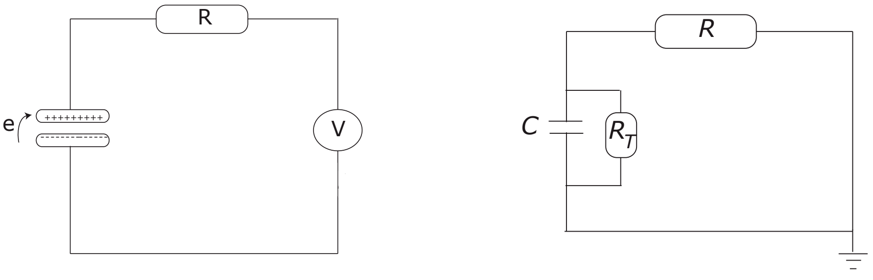

(a) (b)

Figure 2.9: Two different representations of a normal state tunnelling junction, representing the main element in the composition of a SET. (a) Tunnel junction described by its intrinsic capacitor, resembling the electrons potential barrier, linked to an external voltage source and to a resistive load R; (b) the same junction loaded with R and having an intrinsic normal tunnelling resistance R_T.

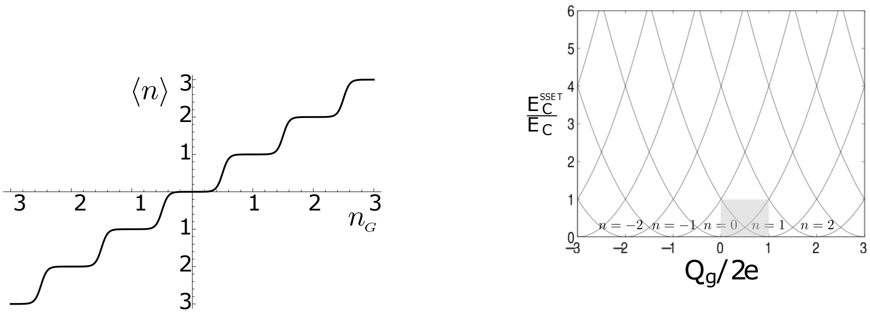

(a) (b)

Figure 2.10: (a) Expectation value of the island charge operator in a SSET. Variations of the gate charge n_g make the expectation value vary of a single unit at the time, producing a staircase function with plateaus symmetrically centred around integer gate charges. (b) The spectrum of a SSET. It is comprised of parabolas centred in integer values n_g of the gate charge, each of them corresponding to an eigenstate of the island charge operator. Varying the gate charge n_g up to a semi-integer value, the island charge can vary by $\pm 2e$, i.e. one CP can be transferred outside or inside the island.

to the generic SET in Fig. 2.8. The single electron charging energy of such a device takes the form $E_C^{SET}(n, Q_G) = (ne - Q_G)^2 / C_{set} = 2E_C \left(n - \frac{Q_G}{e}\right)^2$, where $C_{\mathrm{SET}} = C_L + C_R + C_G$ and $Q_G = C_L V_L + C_R V_R + C_G V_G$ is the gate charge (Heikkilä [2013]). Its energy spectrum consists of a succession of parabolas, each of them having the vertex in a different integer value of the island charge n: changing Q_G, it is possible to manipulate the island charge. In the end, a single electron current flows (from left to right side) whether the conditions

$-eV_R < \delta E_C^{set}(n) < eV_L$, where $\Delta E_C^{SET}(n) = 2E_C\left(n + \frac{1}{2} - \frac{Q_G}{e}\right)$.

In a SSET the tunnelling of CPs is considered and, clearly, this transport phenomenon is dissipationless: the electrodes are superconducting state metals with an insulating layer, so essentially a JJ. When the temperature is sufficiently low, quasiparticle excitations cannot take place and thus the main measurable effect is the tunnelling of a single CP from one electrode to the other, changing the total amount of charge on the superconducting electrodes by $2e$: the SSET's island Hamiltonian, considering only the tunnelling across only one junction, has a form very close to the one of the CPB in Eq. (2.7), composed by a kinetic term (modulated by the charging energy E_{C}) and by the tunnelling energy (weighted by the Josephson energy E_{J}), contributing to the potential. Even in the SSET case the Coulomb blockade is needed to control the system at the level of the single CP: in order to have tunnelling of a single CP, as suggested in Pekola et al. [2013], the kinetic part needs to dominate the energy of the system, is such a way that the inequality $E_{\mathrm{C}} \ll E_{\mathrm{J}}$ is valid. From the quantum mechanical point of view, the capacitive energy of the junction, operator diagonal in the number states, becomes dominant and the potential part given by the Josephson element's energy can be treated as a perturbation: the spectrum is composed of a series of parabolas, function of the gate charge n_{g} and centred in different integer values of n, as reported in Fig.2.10a. Adiabatic changes of the gate charge n_{g} can move the system energy in a degeneration point of the spectrum $n_{\mathrm{g}} = n \pm \frac{1}{2}$ (n can be any integer value), and there the charge n of the island can change by ± 1, in the sense that a single CP can be transferred inside or outside the island: the characteristic dependence between $\langle n \rangle$ and n_{g} is close to the staircase in Fig. 2.10b, but in the case of SSET the distance in charge between two plateaus is $2e$ and not the simple electronic charge unit.

Coulomb blockade regime holds when zero-point fluctuations of the charge operator are sufficiently low to control the charge tunnelling efficiently. From the quantum mechanical point of view, the flux and the charge are conjugated variables, in such a way that their zero-point fluctuations fulfil the uncertainty product $Q_{\mathrm{ZPF}}\phi_{\mathrm{ZPF}} = \frac{\hbar}{2}$ and their expressions are (Girvin [2011])

$$Q_{ZPF} = 2e\sqrt{\frac{1}{4\pi\frac{\mathcal{Z}}{R_{\mathcal{K}}}}}, \tag{2.24}$$

$$\phi_{ZPF} = \Phi_0\sqrt{\frac{1}{4\pi}\frac{\mathcal{Z}}{R_K}}, \tag{2.25}$$

modulated by the characteristic impedance of the junction

$$\mathcal{Z} \sim R_K\sqrt{2\frac{E_C}{E_J}}. \tag{2.26}$$

where $R_K = \frac{h}{(2e)^2} \approx 1027\Omega$ is the superconducting resistance quantum. In order to have low uncertainty in the charge the condition $Q_{ZPF} \ll 2e \rightarrow \mathcal{Z} \ll R_K$ must hold, given that the Coulomb blockade regime is achieved when $E_{\mathrm{J}} \ll E_{\mathrm{C}}$. In the end, a SSET needs the quantization of the CPs'charge which holds when the superconducting junctions in the SSET have a characteristic impedance larger than the superconducting resistance quantum, i.e. $\mathcal{Z} \gg R_K$, a condition which can be physically realized by taking junctions with very small capacitance, achievable taking junction with very small section.

The Coulomb blockade of SSETs has been implemented in the design of CPs pumps, acting very similarly to a charge qubit. The JJs characterized by a strong Coulomb blockade. Just to point out a few examples found in the literature, it is worth mentioning the work of Hoehne et al. [2012]. Here, the device's structure is composed of a SQUID linked to a JJ, individuating a superconducting island and two superconducting leads in the same way as the SC. One CP has been transferred from one lead into the island, and consequently to the second lead. The characteristic impedance of the JJ, computed from the physical JJs dimensions through Eq. (2.26), is $\mathcal{Z} \approx 3358\Omega$, allowing this device to behave as a charge qubit. The single CP pumping device found in the work of Bouchiat et al. [1998] share the same lumped element description of the SC: here, a single CP has been transferred in a superconducting lead-island-lead configuration characterized by an impedance $\mathcal{Z} \approx 5135\Omega$. It is worth just to mention also the works of Niskanen et al. [2003] and Niskanen et al. [2005].

2.5 Semiclassical regime and Coulomb blockade in SSET

The main result of the semiclassical analysis, as already reported in the Introduction, is that the island phase of the SC in Fig. 1.1 in this regime has very intricate dynamics. The observation of such dynamics is, in principle, possible only in a regime, in which the superconducting island phase has the lowest possible quantum mechanical indetermination. Considering only one of the two JJ of the circuit, the zero-point-fluctuations of the phase can be explicitly derived by Eq. (2.25) recalling that the phase coincides with the flux except less than a multiplicative factor $\frac{2\pi}{\Phi_0}$:

$$\varphi_{ZPF} = \sqrt{\pi \frac{\mathcal{Z}}{R_K}}. \tag{2.27}$$

This uncertainty needs to be minimized, leading to the condition $\mathcal{Z} \ll R_K$, or $E_\mathrm{C} \ll E_\mathrm{J}$. The last inequality means that the tunnelling contribution is the leading one, so the capacitative energy is subdominant. This condition looks different form the usual regime of the SSETs.

It is straightforward to see that, even though they share almost the same lumped-element description, the SSET and the SC have diametrically opposite working regimes. Indeed, the former works for $\mathcal{Z} \gg R_K$ ($E_C \gg E_J$), where the charge is completely determined at the expense of the phase and the control of a single CP is possible. Conversely, for observing the semiclassical dynamics of the semiclassical voltage-biased series of two JJs, the working regime is $\mathcal{Z} \ll R_K$ ($E_C \ll E_J$), giving lowest-uncertainty phase and high indetermination of the charge. In conclusion, it seems that a device, having the same lumped-element description of the SC, can reproduce a semiclassical non-linear dynamics of the phase at low impedance, whereas it behaves similarly to a SSETS at high impedance. The physical dimensions of the junctions are important in the determination of the junction's impedance and, consequently, in the determination of the working regime of the device. If in the case of the SSETs a low capacitance value can be set up limiting the junction's section, the semiclassical regime can be achieved by building junctions with very large sections, even macroscopic. Another possible setting could be to add a large shunting capacitance in parallel to the intrinsic one. In conclusion, the physical parameters of the voltage-biased JJs series for reproducing the semiclassical results have to be similar to the ones of the phase qubits.

Supposing to take the inter-space between the two superconducting electrodes to be almost equal for all the devices (order of 1 nm), the ratio $r = \frac{E_J}{E_C}$ can be tuned just changing the section Σ of the junctions. Thus, the suitable range of Σ that can be suggested to reproduce the working regime of a phase or a flux qubit needs to fulfill $10^4 < r < 10^6$, where the upper and lower bounds have been taken from Tab. 2.1 and Wendin [2017]. The denominator of the ratio can be approximated by the standard formula $E_C = 2\epsilon \frac{\Sigma}{de^2}$, where $\epsilon = \epsilon_r \epsilon_0$ is the dielectric constant of the junction. The expression of the Josephson energy is $E_J = \frac{\Phi_0}{2\pi} I_C$. The critical current can be derived from first-principles as it has been done in Ambegaokar and Baratoff [1963], where the upper limit for the junction's super-current is $I_C = \frac{\Delta(0)\pi}{2R_N}$. Assuming that the normal resistance R_N scales exponentially with the electrodes inter-space $R_N = R_{N0} e^{\frac{d}{\zeta}}$ and this scaling is modulated through the physical distance $\zeta = 2\pi \left(\sqrt{\frac{2m_e W}{\hbar^2}} \right)^{-1}$, where W is the metallic (aluminium) working function. Assembling all the formulas, one finally arrives at the expression for the junction's section

$$\Sigma(r) = r \cdot \frac{4e^3 R_{N0}}{h\epsilon\Delta(0)} de^{\frac{d}{\xi}}. \tag{2.28}$$

Given that the working point for a flux or a phase qubit is around $10^4 < r < 10^6$, the corresponding suitable section' range is within 10^{-2} mm$^2 < \Sigma < 1$ mm^2.

Chapter 3

Semiclassical analysis of the superconducting circuit

3.1 Undetermined Lagrangian multiplier method

The description of a voltage-biased superconducting circuit, needs a particular mathematical treatment. One of the possible procedures, discussed in Sec. 2.2 and exposed in Vool and Devoret [2017], relies on the substitution of the voltage source with a buffer capacitor, whose capacitance is taken to be large, even infinite, after all the standard calculations. The converging Hamiltonian expression correctly takes into account the external voltage on the superconducting circuit through the definition of a voltage-dependent gate charge n_{g}. Through this method, the CPB Hamiltonian has been correctly derived.

What is going to be discussed here is an alternative scheme for accounting external voltages, based on a set of "undetermined" Lagrangian multipliers related to specific holonomic constraints coming from the presence of voltage sources in the circuit. These Lagrangian multipliers, $\{\lambda_{\mathrm{k}}(t)\}_{k=1,\ldots,\mathcal{N}}$ with $\mathcal{N}$ being the number of voltage constraints, could have a physical interpretation, but it neglected in this work: here, they are introduced just to take account of voltage sources in the Lagrangian and their expression will be fixed by reimposing the constraints on the multipliers-dependent EOMs. The "undetermined" attribute comes exactly from the latter aspect. The constraints, instead, come out from Kirchhoff's voltage rule, for which the sum of all the potential differences around one loop is equal to zero $\sum_{i=1}^{N} v_i = 0$. Since in the case of a superconducting circuit the nodes voltages, enclosed in a vector $\vec{v}$, are related to the Lagrangian velocities though the relation $\vec{v} = \dot{\vec{\phi}}$ (see Eq. (2.4)), the derivative constraints $f_{\mathrm{k}}(\dot{\vec{\phi}}, t) = 0$ represent integrable holonomic constraints, with $\{f_{\mathrm{k}}(\dot{\vec{\phi}}, t)\}_{k=1,\ldots,\mathcal{N}}$ being linear combinations of the derivatives. The latter can be directly integrated into time-dependent functions $\{g_{\mathrm{k}}(\vec{\phi}, t)\}_{k=1,\ldots,\mathcal{N}}$, defined as $f_{\mathrm{k}}(\dot{\vec{\phi}}, t) = \dot{g}_{\mathrm{k}}(\vec{\phi}, t)$, giving rise to new constraints such as $g_{\mathrm{k}}(\vec{\phi}, t) = \mathcal{C}$ (without loss of generality, the constant $\mathcal{C}$ can be taken equal to zero), now strictly dependent on the coordinate variables $\vec{\phi}$, and new Lagrangian multipliers $\{\alpha_k(t)\}_{\mathrm{k}=1,\ldots,\mathcal{N}}$. Given an unconstrained Lagrangian $\mathcal{L}_0$, in the presence of such coordinate-function holonomic constraints, the expected Euler-Lagrangian Equation for the generic degree of freedom i takes the following form (Hand and Finch [1998]):

$$\frac{\partial \mathcal{L}_0}{\partial \phi_i} - \frac{d}{dt}\frac{\partial \mathcal{L}_0}{\partial \dot{\phi}_i} + \sum_k \alpha_k(t) \frac{\partial g_{\mathrm{k}}(\vec{\phi}, t)}{\partial \phi_i} = 0. \tag{3.1}$$

A straightforward manipulation rewrites the Euler-Lagrange equations as

$$\frac{\partial}{\partial \phi_i}\left(\mathcal{L}_0 + \sum_k \alpha_k(t) g_{\mathrm{k}}(\vec{\phi}, t)\right) - \frac{d}{dt}\frac{\partial}{\partial \dot{\phi}_i}\left(\mathcal{L}_0 + \sum_k \alpha_k(t) g_{\mathrm{k}}(\vec{\phi}, t)\right) = 0. \tag{3.2}$$

Thus, the coordinate holonomic constraints have been absorbed in the Lagrangian

$$\mathcal{L}_1 = \mathcal{L}_0 + \sum_{k=1}^{\mathcal{N}} \alpha_k(t) g_k(\vec{\phi}, t), \tag{3.3}$$

leading to the Euler-Lagrange equations describing the superconducting circuit.

The issue is that Lagrangian (3.3) does not contain the desirable derivative constraints, but rather the coordinate holonomic constraints. However, it is possible to prove that by choosing a specific relation between the two Lagrangian multipliers $\lambda_k(t)$ and $\alpha_k(t)$, the Lagrangian with velocities-dependent constraints

$$\mathcal{L}_2 = \mathcal{L}_0 + \sum_{k=1}^{\mathcal{N}} \lambda_k(t) f_k(\vec{\dot{\phi}}, t) \tag{3.4}$$

leads to the desired Euler Lagrange Equations (3.1) describing the system. This can be easily proved by substituting the constraints $f_k(\vec{\dot{\phi}}, t)$ with $\dot{g}_k(\vec{\phi}, t)$ and then applying the chain derivative chain rule. Explicitly

$$\begin{aligned} \mathcal{L}_2 =& \mathcal{L}_0 + \sum_{k=1}^{\mathcal{N}} \lambda_k(t) \dot{g}_k(\vec{\phi}, t) = \\ & \mathcal{L}_0 + \frac{d}{dt}\sum_{k=1}^{\mathcal{N}} \lambda_k(t) g_k(\vec{\phi}, t) - \sum_{k=1}^{\mathcal{N}} \dot{\lambda}_k(t) g_k(\vec{\phi}, t). \end{aligned} \tag{3.5}$$

The Euler-Lagrange Equations are invariant under the summation of total derivative terms to the Lagrangian, like the one coming from the last line of Eq. (3.5), so it can be neglected. Then, if one chooses $\dot{\lambda}_k(t) = -\alpha_k(t)$, Langrangians (3.3) and (3.4) become equivalent, in the sense that they reproduce the same Euler-Lagrange Equation, i.e. the same EOMs. This can be proved by considering the actions related to the two Lagrangians $\mathcal{L}_1$ and $\mathcal{L}_2$ (Landau and Lifschic [1978])

$$\mathcal{S}_1 = \int_{t_1}^{t_2} dt' \left[\mathcal{L}_0 + \sum_{k=1}^{\mathcal{N}} \alpha_k(t') g_k(\vec{\phi}, t')\right], \tag{3.6}$$

$$\mathcal{S}_2 = \int_{t_1}^{t_2} dt' \left[\mathcal{L}_0 + \frac{d}{dt'}\sum_{k=1}^{\mathcal{N}} \lambda_k(t') g_k(\vec{\phi}, t') - \sum_{k=1}^{\mathcal{N}} \dot{\lambda}_k(t') g_k(\vec{\phi}, t')\right]. \tag{3.7}$$

$$\tag{3.8}$$

By integrating the total time derivative term and recalling the choice $\dot{\lambda}_k(t) = -\alpha_k(t)$, the expression of the second Lagrangian becomes

$$\begin{aligned}\mathcal{S}_2 &= \mathcal{S}_1 + \sum_{k=1}^{\mathcal{N}} \lambda_k(t_2) g_k(\vec{\phi}(t_2), t_2) - \sum_{k=1}^{\mathcal{N}} \lambda_k(t_1) g_k(\vec{\phi}(t_1), t_1) = \\ &= \mathcal{S}_1 + \mathcal{K}(t_2) - \mathcal{K}(t_1)\end{aligned} \tag{3.9}$$

essentially given by the action of $\mathcal{L}_1$ and a constant contribution of the type $\mathcal{K}(t_2) - \mathcal{K}(t_1)$. In conclusion, the Lagrangians $\mathcal{L}_1$ and $\mathcal{L}_2$ lead to the same Euler-Lagrange Equations.

Since the voltage constraint of the superconducting circuit in Fig. (3.1) is essentially a function of the derivatives, the constrained Lagrangian used in the semiclassical analysis is of the kind of Eq. (3.5) instead of the standard Eq. (3.3).

3.2 Superconducting phase equation

3.2.1 Semiclassical Lagrangian

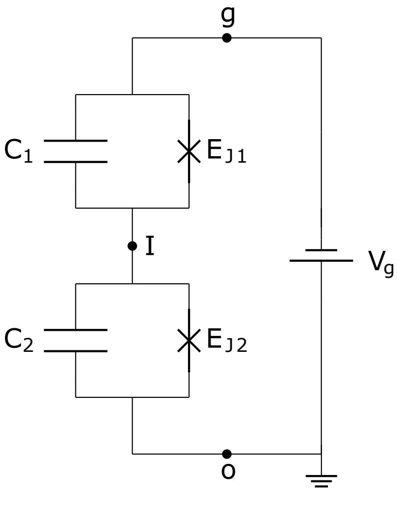

Figure 3.1: Superconducting circuit composed of two JJs in series, linked to an external voltage source. The node *o* is grounded.

The SC, having the lumped element description reported in Fig. 3.1, represents a series of two JJs. This architecture produces a three-part superconducting device composed of two superconducting leads directly linked to the voltage source V_g, indicated by the circuit points g and o, and a superconducting island I delimited by the dielectric material of the two JJs. Following the standard procedure for writing down the SC Lagrangian (Girvin [2011], Vool and Devoret [2017]), it is a function of the node fluxes ϕ_g, ϕ_I and ϕ_o, taken as coordinate variables, and also of the node velocities $\dot{\phi}_\mathrm{g}$, $\dot{\phi}_\mathrm{I}$ and $\dot{\phi}_\mathrm{o}$. These variables can be enclosed in the vectors

$$\vec{\phi} = \begin{pmatrix} \phi_\mathrm{g} \\ \phi_\mathrm{I} \\ \phi_\mathrm{o} \end{pmatrix}, \tag{3.10}$$

$$\vec{\dot{\phi}} = \begin{pmatrix} \dot{\phi}_{\mathrm{g}} \\ \dot{\phi}_{\mathrm{I}}. \\ \dot{\phi}_{\mathrm{o}} \end{pmatrix}, \tag{3.11}$$

which are related to the local voltages through the definition given by Eq. (2.4):

$$\vec{v} = \begin{pmatrix} v_{\mathrm{g}} \\ v_{\mathrm{I}} \\ v_{\mathrm{o}} \end{pmatrix} = \vec{\dot{\phi}}. \tag{3.12}$$

In this formalism, the kinetic energy contribution is given by the intrinsic JJs capacitors C_1 and C_2. The two Josephson elements provide a cosinusoidal potential tuned by the Josephson energies E_{J1} and E_{J2}. The external voltage source V_{g} will be taken into account by writing down a constraint Lagrangian having a structure similar to the one in Eq. (3.4). Therefore, the basic unconstrained Lagrangian $\mathcal{L}_0$, i.e. not considering the voltage source V_{g}, has the following expression:

$$\begin{aligned} \mathcal{L}_0(\vec{\phi}, \vec{\dot{\phi}}) &= \mathcal{T}(\vec{\dot{\phi}}) + \mathcal{U}(\vec{\phi}) \\ &= \frac{1}{2} C_1 (\dot{\phi}_{\mathrm{g}} - \dot{\phi}_I)^2 + \frac{1}{2} C_2 (\dot{\phi}_I - \dot{\phi}_o)^2 \\ &+ E_{J1} \cos\left(\frac{2\pi}{\Phi_0}(\phi_{\mathrm{g}} - \phi_I)\right) + E_{J2} \cos\left(\frac{2\pi}{\Phi_0}(\phi_I - \phi_o)\right). \end{aligned} \tag{3.13}$$

Through the application of Kirchhoff's law on the main circuital loop of the circuit in Fig. 3.1, it follows that $\dot{\phi}_{\mathrm{g}} - \dot{\phi}_o = V_{\mathrm{g}}$, determining the holonomic constraint $\mathcal{V}(\dot{\phi}_{\mathrm{g}}, \dot{\phi}_{\mathrm{o}}) = \dot{\phi}_{\mathrm{g}} - \dot{\phi}_o - V_{\mathrm{g}} = 0$. At first glance, $\mathcal{V}$ does not look to be an integrable holonomic constraint, being just a function of the derivative and not of the coordinate. However, being a linear function of the derivatives, it can be easily tracked back to a holonomic constraint, function of the coordinate, by noticing that

$$\begin{aligned} &\mathcal{V} = \dot{\phi}_{\mathrm{g}} - \dot{\phi}_o - V_{\mathrm{g}} == \frac{d\mathcal{F}}{d\phi_g}\frac{d\phi_o}{dt} - \frac{d\mathcal{F}}{d\phi_o}\frac{d\phi_o}{dt} - \frac{d\mathcal{F}}{dt} = 0 \\ &\to d\mathcal{F} = d\left(\phi_g - \phi_o - V_g t\right) = 0. \end{aligned} \tag{3.14}$$

Thus, $\mathcal{F}(\phi_g, \phi_o, t)$ represents the holonomic constraint related to the integrable holonomic constraint $\mathcal{V}(\dot{\phi}_g, \dot{\phi}_o)$. Following what has been discussed in Sec. 3.1, the Lagrangian of the system can be constrained with the derivative constraint $\mathcal{V}(\dot{\phi}_g, \dot{\phi}_o)$, giving the same true EOMs that one obtains implementing the holonomic constraint $\mathcal{F}(\phi_g, \phi_o, t)$ in Eq. (3.14). The final expression of the constrained Lagrangian is thus straightforwardly derived through the Eq. (3.4):

$$\begin{aligned} \mathcal{L}(\vec{\phi}, \vec{\dot{\phi}}) &= \mathcal{L}_0 + \mathcal{Q} \cdot \mathcal{V}\left(\dot{\phi}_{\mathrm{g}}, \dot{\phi}_o\right) \\ &= \frac{1}{2} C_1 (\dot{\phi}_{\mathrm{g}} + \dot{\phi}_I)^2 + \frac{1}{2} C_2 (\dot{\phi}_I - \dot{\phi}_o)^2 \\ &+ E_{J1} \cos\left(\frac{2\pi}{\Phi_0}(\phi_{\mathrm{g}} - \phi_I)\right) + E_{J2} \cos\left(\frac{2\pi}{\Phi_0}(\phi_I - \phi_o)\right) \\ &+ \mathcal{Q}\left(\dot{\phi}_{\mathrm{g}} - \dot{\phi}_o - V_{\mathrm{g}}\right), \end{aligned} \tag{3.15}$$

where $\mathcal{Q}$ is the Lagrangian multiplier associated to the constraint $\mathcal{V}(\dot{\phi}_{\mathrm{g}}, \dot{\phi}_{\mathrm{o}})$. The variables conjugated to the fluxes are the nodes charges

$$\vec{Q} = \nabla_{\dot{\vec{\phi}}}\mathcal{L} = \begin{pmatrix} Q_{\mathrm{g}} \\ Q_{\mathrm{I}} \\ Q_{\mathrm{o}} \end{pmatrix}, \tag{3.16}$$

derived differentiating the Lagrangian with respect to the derivatives variables. The expressions of the momenta are the following ones:

$$\begin{cases} Q_{\mathrm{g}} = \frac{\partial \mathcal{L}}{\partial \dot{\phi}_{\mathrm{g}}} = C_1(\dot{\phi}_{\mathrm{g}} - \dot{\phi}_I) + Q \\ Q_o = \frac{\partial \mathcal{L}}{\partial \dot{\phi}_o} = -C_2(\dot{\phi}_I - \dot{\phi}_o) - Q \\ Q_I = \frac{\partial \mathcal{L}}{\partial \dot{\phi}_I} = -C_1(\dot{\phi}_{\mathrm{g}} - \dot{\phi}_I) + C_2(\dot{\phi}_I - \dot{\phi}_o). \end{cases} \tag{3.17}$$

The matrix stemming from the last system of equations is singular, so not invertible. The singularity is given by the fact that the last line in Eq. (3.17) is simply minus the sum of the two other equations, in such a way that the sum of the total charges vanishes, i.e.

$$Q_{\mathrm{g}} + Q_{\mathrm{I}} + Q_{\mathrm{o}} = 0. \tag{3.18}$$

Thus, the inversion of the system of equation in Eq. (3.17) can be done by leaving the flux derivatives as functions of $\dot{\phi}_{\mathrm{I}}$:

$$\begin{cases} \dot{\phi}_{\mathrm{g}} = \dot{\phi}_{\mathrm{I}} + \frac{Q_{\mathrm{g}} - \mathcal{Q}}{C_1} \\ \dot{\phi}_{\mathrm{o}} = \dot{\phi}_{\mathrm{I}} - \frac{Q_{\mathrm{o}} + \mathcal{Q}}{C_2}. \end{cases} \tag{3.19}$$

3.2.2 Hamiltonian and EOMs

The SC Hamiltonian is obtained through Legendre transform of the Lagrangian Eq. (3.15):

$$\mathcal{H}(\vec{\phi}, \vec{Q}) = \sum_{k \in [o,I,g]} \left[Q_k \cdot \dot{\phi}_k(\vec{Q}, \dot{\phi}_{\mathrm{I}}) \right] - \mathcal{L}. \tag{3.20}$$

Algebraic manipulations (reported in Appendix D) lead to the SC Hamiltonian

$$\begin{aligned} \mathcal{H} =& \frac{1}{2C_1}\left(Q_{\mathrm{g}} - \mathcal{Q}\right)^2 + \frac{1}{2C_2}\left(Q_{\mathrm{o}} + \mathcal{Q}\right)^2 \\ &+ E_{J_1}\cos\left(\frac{2\pi}{\Phi_0}(\phi_{\mathrm{g}} - \phi_I)\right) - E_{J_2}\cos\left(\frac{2\pi}{\Phi_0}(\phi_{\mathrm{I}} - \phi_o)\right) \\ &+ \mathcal{Q}V_g. \end{aligned} \tag{3.21}$$

At this point, some considerations have to be made. First, it is worth to recall the relation between phase and flux found in Eq. 2.4, which gives

$$\vec{\varphi} = \begin{pmatrix} \varphi_{\mathrm{g}} \\ \varphi_{\mathrm{I}} \\ \varphi_{\mathrm{o}} \end{pmatrix} = \frac{2\pi}{\Phi_0}\vec{\phi}. \tag{3.22}$$

less than a negligible constant. Second, the charges $\vec{Q}$ are associated with the total amount of CPs charge present in each node of the circuit, so they are simply integer multiples of the elementary CPs charge $2e$. Therefore, the following change of variables can be applied to the Hamiltonian

$$\vec{n} = \begin{pmatrix} n_{\rm g} \\ n_{\rm I} \\ n_{\rm o} \end{pmatrix} = \frac{\vec{Q}}{2e}. \tag{3.23}$$

The last consideration is that Eq. (3.18) gives the freedom to neglect one node from the Hamiltonian: one of the three charge variables can be written as a function of the other two. Since the nod o is grounded and, from now on, it is assumed $\varphi_0 = \dot{\varphi}_o = \ddot{\varphi}_o = 0$, it is convenient to neglect completely the node (gauge freedom) in the Hamiltonian by taking $n_o = -(n_I + n_g)$. Then, implementing all these considerations in the Hamiltonian, i.e. inserting the two changes of variable defined in Eqs. (3.22)-(3.23) into Eq. (3.21) along with $\mathcal{N} = \frac{\mathcal{Q}}{2e}$, the final expression of the SC's Hamiltonian becomes

$$\begin{aligned} \mathcal{H} =& 4E_{C_1}(n_{\rm g} - \mathcal{N})^2 + 4E_{C_2}(n_I + n_g - \mathcal{N})^2 \\ & - E_{J_1}\cos(\varphi_{\rm g} - \varphi_I) - E_{J_2}\cos(\varphi_I) + (2e\mathcal{N})V_{\rm g}, \end{aligned} \tag{3.24}$$

Remarkably, the coefficients of the kinetic terms represent the charging energy of a single CP in the two JJs, i.e. $E_C = \frac{e^2}{2C}$.

The redefinition of the Poisson Bracket (see Appendix D) in terms of the conjugated variables $\vec{n}$ and $\vec{\varphi}$ gives Hamilton's equation, i.e. EOMs for the CPs number

$$\begin{cases} \dot{n}_{\rm g} = \{n_g, \mathcal{H}\} = -\frac{1}{\hbar}\frac{\partial \mathcal{H}}{\partial \varphi_g} = -\frac{E_{J_1}}{\hbar}\sin(\varphi_{\rm g} - \varphi_I) \\ \dot{n}_I = \{n_I, \mathcal{H}\} = -\frac{1}{\hbar}\frac{\partial \mathcal{H}}{\partial \varphi_I} = \frac{E_{J_2}}{\hbar}\sin(\varphi_I), \end{cases} \tag{3.25}$$

and for the phase

$$\begin{cases} \dot{\varphi}_{\rm g} = \{\varphi_g, \mathcal{H}\} = \frac{1}{\hbar}\frac{\partial \mathcal{H}}{\partial n_g} = \frac{8E_{C_1}}{\hbar}(n_{\rm g} - \mathcal{N}) + \frac{8E_{C2}}{\hbar}(n_I + n_g - \mathcal{N}) \\ \dot{\varphi}_{\rm I} = \{\varphi_I, \mathcal{H}\} = \frac{1}{\hbar}\frac{\partial \mathcal{H}}{\partial n_I} = \frac{8E_{C_2}}{\hbar}(n_I + n_g - \mathcal{N}). \end{cases} \tag{3.26}$$

3.2.3 Dynamical equation

The EOMs in Eq. (3.26) can not be considered good dynamical equations for several reasons. First, the Lagrangian multiplier $\mathcal{N}$ has to be determined by reimposing the constraint $\dot{\varphi}_g = \frac{2\pi}{\Phi_0}V_g$ on the EOM given by the first line in Eq. (3.26). Reminding to the Appendix D for the details of the calculations, if the two junctions are considered identical, i.e. same Josephson energy $E_{J1} = E_{J2} = E_J$ and total charging energy $E_C = \frac{e^2}{2(C_{J1}+C_{J2})}$, algebraic manipulations of the EOMs given by Eqs. (3.25)-(3.26) lead to a dynamical equation for the redefined phase $\varphi_\Delta = \varphi_I - \frac{\varphi_g}{2}$ with expression

$$\ddot{\varphi}_\Delta = -2\Omega_J^2 \cos\left(\frac{\varphi_{\rm g}(t)}{2}\right)\sin(\varphi_\Delta), \tag{3.27}$$

where $\Omega_J = \frac{\sqrt{8E_J E_C}}{\hbar}$ is the Josephson plasma frequency and $\varphi_g(t) = \omega_g t$ ($\varphi_g(0) = 0$).

This dynamical equation reflects the CSJ model, corresponding to the SC's circuit depicted in Fig. 3.1. Through that lumped element description only dissipationless superconducting currents can be taken into account, in such a way

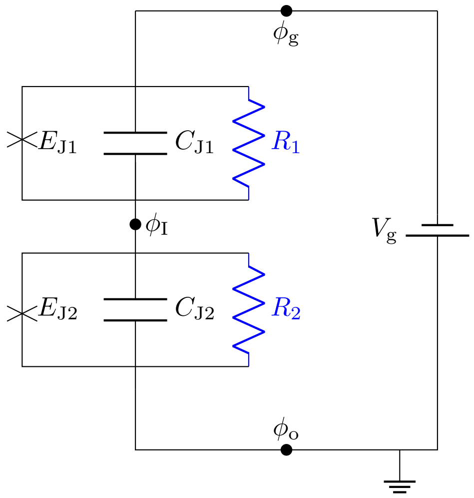

Figure 3.2: Lumped element description of the SC, where the two JJs are described through the RSCJ model: the junction is described as the parallel of Josephson element, intrinsic capacitance and resistance. The latter takes into account linear dissipation effects of the junctions by introducing a friction-like term in the dynamical equation of the phase.

that electrons in the electrodes could be only found tied forming CPs in the condensed ground state of the system. However, this represents an ideal situation, given that the superconducting gap Δ is finite even at zero temperature. Moreover, from a practical point of view, thermal fluctuations are even possible, possibly exciting the CPs in normal-state electrons, i.e. fluctuations could break a certain number of CPs, releasing free electrons that eventually conduct normally under the action of an external electric field. As a consequence, these normal-state electrons could produce an ohmic current, leading to the appearance of dissipative behaviors in the JJ. In order to take account of this kind of dissipation, a shunting resistor can be added to the CJ lumped element representation, resulting in the circuit in Fig. 3.2, and consequently, the RCSJ model (Blackburn et al. [2016]) is used for its description. What comes out from this treatment is the emergence in Eq. (D.21) of a dissipative contribution like $-\gamma\dot{\varphi}_\Delta$ (more details in Appendix E), a friction-like term linear in the superconducting phase derivative. Indeed, the final form of the superconducting phase equation is given by

$$\ddot{\varphi}_\Delta = -2\Omega_J^2 \cos\left(\frac{\varphi_g(t)}{2}\right)\sin\left(\varphi_\Delta\right) - \Gamma\dot{\varphi}_\Delta, \tag{3.28}$$

where the dissipative coefficient $\Gamma = \frac{2}{R(C_{J1}+C_{J2})}$.

It is convenient to recast Eq. (3.28) in its dimensionless form. Considering that φ is already dimensionless, rescaling time is enough to achieve a dimensionless equation. The natural time length for rescaling is the period T_g of the oscillatory term $\cos(\frac{\omega_g}{2}t)\sin(\varphi_\Delta)$, provided by the inverse of the frequency $T_g = 2\frac{2\pi}{\omega_g} = \frac{2\Phi_0}{V_g}$. Explicitly, when the rescaling $\tau = \omega t$ is applied, Eq. (3.28) takes the dimensionless form

$$\frac{d^2\varphi_\Delta}{d\tau^2} = \bar{\epsilon}\cos(\tau)\sin(\varphi_\Delta) - \gamma\frac{d\varphi_\Delta}{d\tau}, \tag{3.29}$$

with the dimensionless parameters

$$\bar{\epsilon} = 8\frac{\Omega_{\mathrm{J}}^2}{\omega_{\mathrm{g}}^2} = \frac{64E_{\mathrm{C}}E_{\mathrm{J}}}{(2e)^2V_{\mathrm{g}}^2}, \tag{3.30}$$

and

$$\gamma = \frac{2}{\omega_g R(C_{\mathrm{J1}} + C_{\mathrm{J2}})}. \tag{3.31}$$

Chapter 4

Kapitza pendulum and the superconducting circuit

4.1 Kapitza pendulum

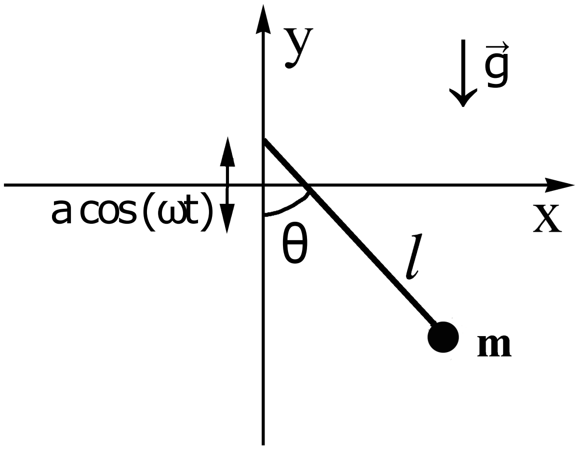

Figure 4.1: Schematic representation of a mechanical KP: a pendulum of length l and a mass m, exposed to gravity and having a deviation angle θ, measured with respect to the vertical axis, and a periodically oscillating pivot. The axis y corresponds to the vertical direction along which there is gravity and pivot oscillation, whereas the x axis is perpendicular to the driving oscillation of the KP.

The Kapitza pendulum (KP) refers to an extensively studied mechanical problem, taking its name from the Russian physicist Piotr Kapitza, who first addressed some specific dynamical issues of the system. A schematic representation of a KP is reported in Fig. 4.1. Physically, it consists of a rigid rod of length l with a mass m attached to its free-to-move end, while the other end is a pivot constrained to oscillate with a periodical vibration $y_0(t) = a\cos(\omega t)$ with amplitude a and oscillation frequency ω: the KP is a vertically and periodically driven pendulum. The pivot's oscillation takes place along the y direction, i.e. the gravitational direction. The latter is taken as the reference axis for measuring the deviation angle θ of the pendulum: it represents the dynamical variable of the system and it usual takes values on a circles $\theta \in [0, 2\pi]$. The gravitational force generates a torque $\mathcal{M}_g = -mgl\sin(\theta)$ and, considering the non-inertial reference frame of the pendulum, the virtual force $-m\ddot{y_0}(t) = m\omega^2 y_0(t)$ contributes with a torque $\mathcal{M}_p = -m\ddot{z}l\sin(\theta) = -mal\omega^2\cos(\omega t)\sin(\theta)$. When $y_0(t) > 0$, in the positive half oscillation, the effect of the non-inertial force is to reduce the gravitational force, whereas the gravity is strengthened in the semi-oscillation $y_0(t) < 0$. The dynamical equation describing the time evolution of the KP angle θ in the non-inertial frame, introducing a dissipation term $-\gamma\dot{\theta}$ due to the friction, can be derived from the Newton's second law $\mathcal{M}_g + \mathcal{M}_p = ml^2\ddot{\theta}$:

$$\ddot{\theta} = -\Big(\omega_0^2 + \frac{a}{l}\omega^2\cos(\omega t)\Big)\sin(\theta) - \Gamma\dot{\theta}, \tag{4.1}$$

where $\omega_0 = \sqrt{\frac{g}{l}}$ is the proper frequency of the pendulum. Rescaling time as $\tau = \omega t$ in Eq. (4.1) is sufficient to obtain the dimensionless dynamical equation

$$\frac{d^2\theta}{d\tau^2} = -\left(k + m\cos(\omega t)\right)\sin(\theta) - \gamma\frac{d\theta}{d\tau}, \tag{4.2}$$

with the dimensionless parameter $k = \frac{\omega_0^2}{\omega^2}$, the dimensionless driving amplitude $m = \frac{a}{l}$ and $\Gamma = \frac{\gamma}{\omega}$. When the pivot's oscillation is not considered the KP converges to a simple pendulum. Indeed, when the driven oscillation $a = 0$, Eq. (4.2) becomes

$$\frac{d^2\theta}{d\tau^2} = -\omega_0^2\sin(\theta) - \gamma\frac{d\theta}{d\tau}, \tag{4.3}$$

i.e. the equation of a damped simple pendulum.

4.2 Correspondence between Kapitza pendulum and superconducting circuit

The superconducting phase equation (3.29) shows an expression resembling the dynamical equation ruling the time evolution of the KP angle. Drawing a connection between these two dynamical equations means that they share the same dynamical evolution, i.e. the SC, at semiclassical level, behaves actually as a planar rotor with moving pivot. It has to be clarified to what extent these two problems can be mapped one into the other. In particular, the relations between the mechanical and the superconducting parameters have to be found. In order to achieve a concrete mapping between the models, the dimensionless expressions of the two dynamical equations have to be considered. For the sake of simplicity, both equations are reported and aligned below (the dissipative parts are neglected for the moment):

$$l\ddot{\theta} = -\left(g + a\omega^2\cos(\omega t)\right)\sin(\theta), \tag{4.4}$$

$$\ddot{\varphi}_\Delta = -2\Omega_J^2\cos\left(\frac{\omega_{\mathrm{g}}}{2}t\right)\sin\left(\varphi_\Delta\right) \tag{4.5}$$

Observing these two equations, it is straightforward to see that they have a dimensionless degree of freedom (respectively the mechanical KP angle θ and the superconducting phase φ_Δ), same structural dependence on time, but different functional dependence on the other dynamical parameters. Moreover, the number of dynamical parameters for the two models seem to be different: the mechanical problem is controlled by gravity g, driving amplitude $a\omega^2$ and the driving frequency ω, considering the length l as a physical dimension, whereas in the superconducting case ω_g is the only dynamical parameter with the Josephson plasma frequency which is determined by the physical dimensions of the JJs. However, for both problems, the real number of independent parameters can be reduced. Considering only the KP Eq. (4.5), dividing by the non-vanishing rod length l, the gravitational and driving parameters respectively become $\frac{g}{l}$ and $\frac{a\omega^2}{l}$. The dimensionless form of KP equation can be simply achieved by rescaling the time through the relation $\tau = \omega t$. Applying this rescaling to Eq. (4.5), aligning the obtained result with the rescaled dynamical equation of the SC

$$\frac{d^2\theta}{d\tau^2} = -\left(\frac{\omega_0^2}{\omega^2} + \frac{a}{l}\cos(\tau)\right)\sin(\theta) \to \frac{d^2\theta}{d\tau^2} = -\left(k + m\cos(\tau)\right)\sin(\theta) \tag{4.6}$$

$$\frac{d^2\varphi_\Delta}{d\tau^2} = -\frac{8\Omega_J^2}{\omega_g^2}\cos(\tau)\sin(\varphi_\Delta) \to \frac{d^2\varphi_\Delta}{d\tau^2} = -\bar{\epsilon}\cos(\tau)\sin(\varphi_\Delta), \tag{4.7}$$

and recalling that the dimensionless parameters takes the form $k = \frac{\omega_0^2}{\omega^2}$ and $m = \frac{a}{l}$ for KP whereas $\bar{\epsilon} = \frac{8\Omega_J^2}{\omega_g^2}$ for SC, it is straightforward to realize that the KP equation can be mapped in the SC equation if the following relations between the parameters hold:

$$\begin{aligned} k &= 0 \\ m &= \bar{\epsilon}. \end{aligned} \tag{4.8}$$

Through this equivalence, finding the angular trajectories, i.e. solutions of Eq. (4.2), corresponds to finding the time evolution of the superconducting phase φ_Δ. For the fact that the latter is related to the super-current flowing across the island, the initial conditions for the KP mechanical angle $\theta(0)$ are in correspondence with the initial value of the island super-current. The same is true also for the initial conditions of the derivatives, in such a way that imposing initial conditions on the angular velocity $\dot{\theta}(0)$ for KP is equivalent to setting the initial island voltage $\varphi_\Delta(0) = \varphi_I(0) + \frac{\varphi_\mathrm{g}(0)}{2} = \varphi_I(0)$ for the SC. The fact that it has been chosen $\varphi_g(0) = 0$ for the SC means, in the usual KP-SC correspondence, that for KP the pivot oscillation has zero initial phase.

From a practical point of view, a zero-gravity KP can be reproduced by a vertically driven pendulum placed in a plane perpendicular to the gravitational acceleration $\vec{g}$, and even in the lack of gravity, the line across which the pivot oscillates can be used as reference direction: the KP angles can be measured from this axis. The orientation of this axis, i.e. fixing the inverted and normal position of the pendulum, can be, in principle, arbitrary since the absence of gravity does not individuate any reference orientation in the planar KP. However, the orientation of the reference axis can be fixed by assuming that the pole $\theta = \pi$ relies on the semi-axis individuated by the first positive quarter-oscillation of the pivot: this assumption a priori will be then justified through the results of the numerical simulations. Final considerations about the symmetry of the problem suggest that the solutions of Eq. (4.7) could be invariant under reflection with respect to the pivot oscillation axis, i.e. in the case of the planar KP, the latter consists in $\begin{cases} x' = -x \\ y' = y \end{cases}$ (with reference to the Fig. 4.1) or, otherwise, $\theta' = -\theta$ leaves the dynamics unchanged. Given the resemblance between the KP and the SC Eqs. (4.6)-(4.6) for the parameters in Eq. 4.8, they will be generically referred to as dynamical equation in the following discussion.

In conclusion, a schematic comparison between the KP and the SC problems is reported in Tab. 4.1.

Mechanical KP	Superconducting voltage-biased JJs series
$\theta(t)$	$\varphi_\Delta(t)$
$\theta(0)$	$\varphi_\Delta(0) = \varphi_I(0)$
$\dot\theta(0)$	$\dot\varphi_\Delta(0)$
$m \propto a$	$\bar\epsilon \propto V_{\mathrm{g}}^{-2}$
$k \propto g$	—

Table 4.1: Correspondence between the variables, initial conditions and dynamcial parameters of the mechanical KP and the SC.

Chapter 5

Dynamics of the superconducting phase

5.1 Numerical simulations

The dynamical equation for the phase φ_Δ

$$\ddot{\varphi}_\Delta = -\bar{\epsilon}\cos(\tau)\sin(\varphi_\Delta) - \gamma\dot{\varphi}_\Delta \tag{5.1}$$

is a non-linear equation which can be exactly solved, in terms of Mathieu's functions, only in the isochronic approximation $\sin(\varphi_\Delta) \approx \varphi_\Delta$. In order to have an insight on the solutions $\varphi_\Delta(t)$ of the full model (5.1), numerical simulations need to be performed. The initial conditions need to be chosen according to the superconducting context where Eq. (5.1) has been derived. Therefore, given the correspondence between the $g = 0$ KP and the superconducting circuit and the symmetries of the problem, it appears natural to consider the superconducting phase as an angular variable on a bi-dimensional circle, taking values $\varphi_\Delta(0) \in \left[\frac{\pi}{2}, \pi\right]$, i.e. this choice of initial conditions means that numerical simulations will be performed in the first quadrant of the x-y plane of KP (see Fig. 4.1). On the other hand, the nature of the solutions coming from those initial conditions depends just on the dynamical parameter present in Eq. (5.1): $\bar{\epsilon} = 8\frac{\Omega_\mathrm{J}^2}{\omega_\mathrm{g}^2} = \frac{64E_\mathrm{C}E_\mathrm{J}}{(2e)^2V_\mathrm{g}^2}$. From the latter, it is straightforward to see that voltage V_g determines the dynamical behavior, through the parameter $\bar{\epsilon}$, of the solutions $\varphi_\Delta(t)$ related to the time evolution of the island super-current. Thus, in the end, $\varphi_\Delta(0)$ along with $\bar{\epsilon}$ are the natural parameters space for investigating the dynamical equation for superconducting island phase of the two voltage-biased JJs in series. The role of the dissipation in the dynamics is not analyzed in this work, even though γ is a dynamical parameter strongly affecting the dynamical properties of the solutions. For convenience, it will be kept fixed at value $\gamma = 10^{-2}$, along with $\dot{\varphi_\Delta}(0) = 0$.

Direct time propagation has been used to perform numerical integration of Eq. (5.1), which can be easily transformed from a second order differential equation to an ODE system

$$\begin{cases} \dot{\varphi}_\Delta = \psi_\Delta \\ \dot{\psi}_\Delta = -\bar{\epsilon}\cos(\tau)\sin(\varphi_\Delta) - \gamma\psi_\Delta \end{cases} \tag{5.2}$$

using then a fourth-order Runge-Kutta integration method.

The main purpose of numerical integrations is obtaining a clear and complete picture of the attractors coming out from the dynamics of Eq. (5.2) (implicitly, of Eq. (5.1)) and comparing the results with the ones known for the KP. Numerically, the attractors of the dynamical equation can be found through a specific numerical procedure: each solution is essentially labelled with its specific attractor. This characterization of the dynamical equation solutions is crucial to understand what is the distribution of the attractors in the stability diagrams obtained from the bidimensional parameters space ($\bar{\epsilon}$, $\varphi_\Delta(0)$). The accuracy of such distributions of the attractors in the stability diagrams depends on how many simulations of the dynamical equation are performed: the higher the number of simulations made for $\varphi_\Delta(0)$ and $\bar{\epsilon}$, the higher the accuracy of the attractors distribution and the resolution of the stability diagrams.
More details about the numerical procedures can be found in Appendix F.

5.2 Attractors and stability diagrams

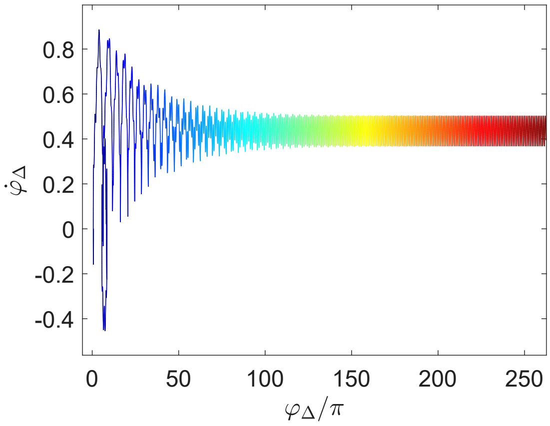

Figure 5.1: Unstable solution for $\bar{\epsilon} = 0.58$ and $\varphi_\Delta(0) = 0.8\pi$. The change in color of the plot from dark blue to black indicates the direction of time in all the plots. Here, the trajectory does not remain in a neighborhood of one of the fixed points. In the mechanical equivalent description, it is like the pendulum continues to constantly rotate with an angle exceeding the range $[0, 2\pi]$.

The solutions of the ODE system in Eq. (5.2) individuate orbits in the phase-space constituted by the velocity $\dot{\varphi}_\Delta(t)$ and the phase $\varphi_\Delta(t)$. The representation of the solutions in the phase-space allows to recognize the asymptotic attractors to which the trajectories tend. This analysis makes it clear that four different attractor types emerge from the dynamical equation. Not surprisingly, the upper and the lower fixed points, i.e. the normal and inverted position, respectively given by $\varphi_\Delta = 0$ and π, are observed to be stable and unstable, depending on the choice of the parameters. An example of unstable solutions is reported in Fig. 5.1. This kind of solution is characterized by a damped oscillation which, after a certain amount of time, continues to rotate indefinitely, exceeding many

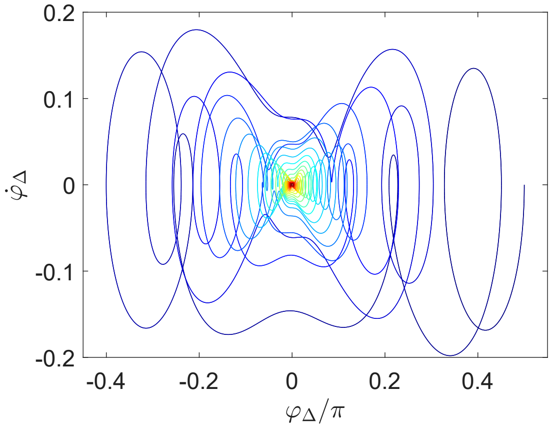

(a)

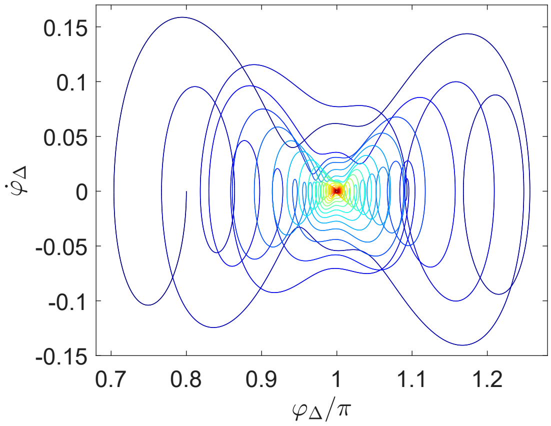

(b)

Figure 5.2: Trajectories in the phase-space of two stable (a)-(b) solutions. The change in color of the plot from dark blue to black indicates the direction of time in all the plots. (a) 0-stable solution for $\bar{\epsilon} = 0.27$ and $\varphi_\Delta(0) = 0.5\pi$. (b) π-stable solution for $\bar{\epsilon} = 0.27$ and $\varphi_\Delta(0) = 0.8\pi$.

times the circular angles $[0, 2\pi]$. At the level of the Eq. (5.2), the oscillatory term appears to sustain the rotation, becoming dominant with respect to the dissipation.

For certain values of the parameters, some trajectories become stable around the phase-space fixed points $(0, 0)$ and $(0, \pi)$, i.e. the normal and inverted position: when a solution converges to the former, it has a $0-$stable attractor, while the convergence to the latter implies a $\pi-$stable attractor. Two examples are reported in Fig. 5.2: they start from their respective initial conditions and, in both cases, the phase exhibits damped oscillation with decreasing amplitude: the trajectories, in the phase-space, are converging to their respective fixed points. Here, the dissipation seems to overcome the oscillating driving, giving an asymptotic damping leading the trajectory to essentially contract towards

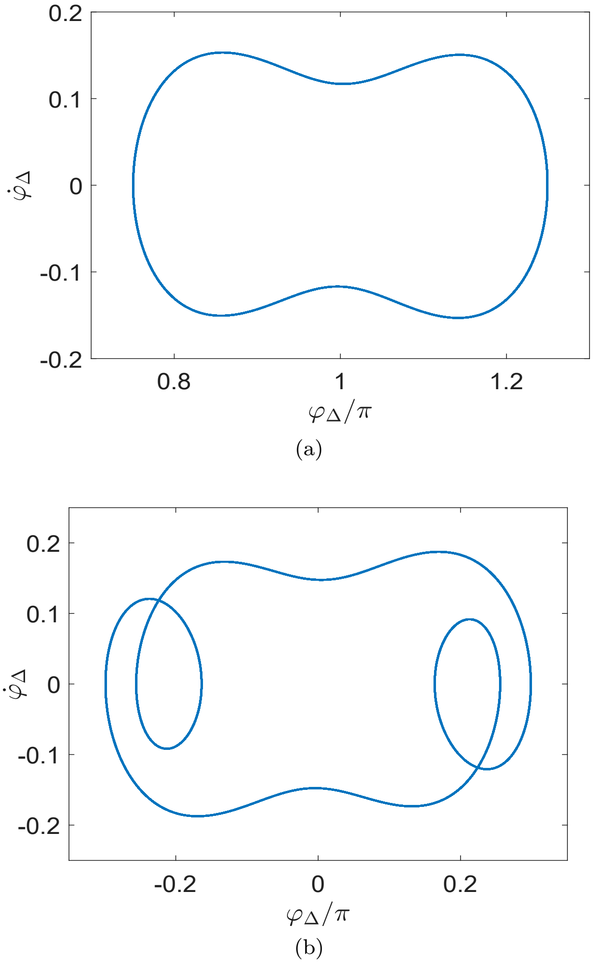

Figure 5.3: Two examples of $n-$cycles solutions: (a) $1-$cycle for $\bar{\epsilon} = 0.5$, $\varphi_\Delta(0) = 0.7\pi$; (b) $3-$cycle for $\bar{\epsilon} = 0.37$, $\varphi_\Delta(0) = 0.54\pi$.

the fixed point. Recalling the KP correspondence, in these trajectories the rigid rod is essentially going upward and downward alongside the driving oscillation, periodically sustained just by the pivot movement. The 0-stable and the π-stable solutions found here are essentially of the same kind of the ones in the general KP problem.

The limit-cycles are the last type of attractors encountered in the superconducting phase dynamics: some examples of these attractors are reported in Figs. 5.3-5.4. Their appearance is expected for the fact that the dynamical equation is an explicit function of time. Different values of the parameters lead to limit-cycles having a different number of nods, where the nod is defined as the physical point in which the periodic trajectory changes velocity, i.e. it is the phase-space point where the orbit intercepts the $\dot{\varphi}_\Delta(t) = 0$ axis. From now on, the limit-cycle trajectories emerging from the dynamics will be called $n-$cycles, where n is the number of times the trajectory nods on the right or the

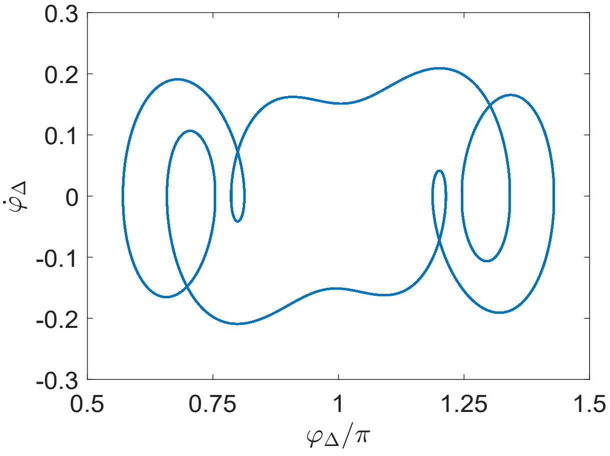

(a)

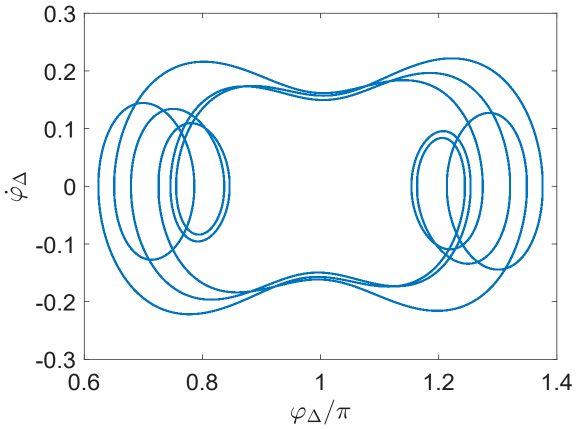

(b)

Figure 5.4: Two examples of $n-$cycles solutions: (a) $5-$cycle for $\bar{\epsilon} = 0.318828$, $\varphi_\Delta(0) = 0.727783\pi$; (b) $9-$cycle for $\bar{\epsilon} = 0.385088$, $\varphi_\Delta(0) = 0.827393\pi$.

left side of the fixed point, exactly equivalent to the number of nods observed during half oscillation period. The kinds of attractors emerging from the dynamical equation are, as expected, the same of the KP. What is interesting to investigate then is how these attractors are distributed in the stability diagrams composed of 1024×1024, i.e. order of 10^6, simulations given by choosing a parameters space comprised of 1024 equidistant points of $\bar{\epsilon} \in [0.01, 0.60]$ and 1024 equidistant points of $\varphi_\Delta(0) \in \left[\frac{\pi}{2}, \pi\right]$. The results of these simulations is the stability diagram reported in Fig. 5.5. Each point of this diagram represents a simulation performed for specific values of $\varphi_\Delta(0)$ and $\bar{\epsilon}$ and its corresponding coloured label indicates its asymptotic attractor.

It is straightforward to see that the attractors generate four distinct regions. Above $\bar{\epsilon} = 0.3$ one can find essentially $0-$stable (light blue) or π-stable (orange) attractors and the border dividing the regions is linear, while below this value the dynamics become very intricate, and the stability is replaced by an

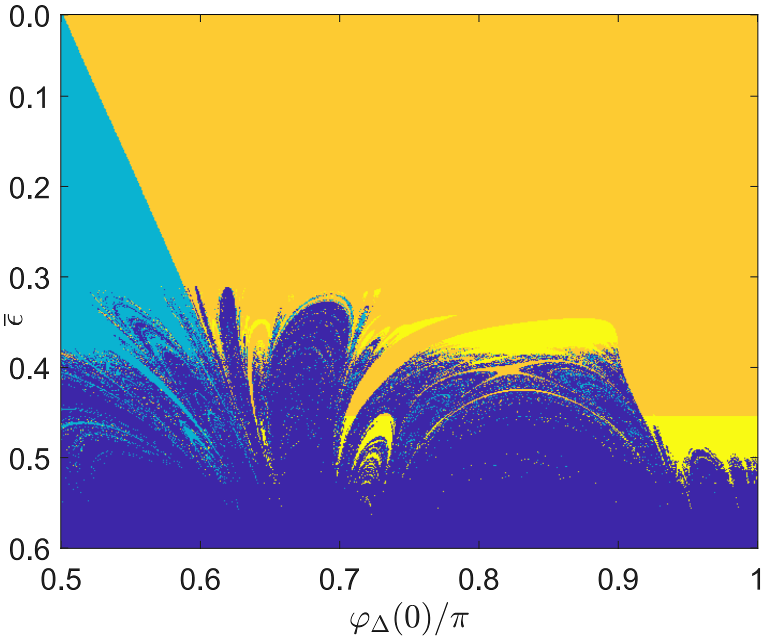

Figure 5.5: Stability diagram of the parameters space comprised of 1024×1024 points for $\varphi_\Delta \in \left[\frac{\pi}{2}, \pi\right]$ in the horizontal axis and $\bar{\epsilon} \in [0.30, 0.58]$ in the vertical axis. The space is divided into four regions by the attractors, each of them labelled by a different color: dark blue stands for unstable, light blue for 0-stable, orange for π-stable and yellow for limit cycles solutions.

increasing instability (dark blue) mixed to periodic limit-cycles (yellow). In the lower half-space, the transition between different attractors appears very discontinuous and here the system seems very sensitive to the initial conditions: a small perturbation of the parameters could change drastically the solutions, and consequently the dynamical behavior of the phase. In order to have a clearer picture of the phase dynamics in the lower part of the diagram, further simulations have been performed in such a way to obtain the stability diagram at higher resolution reported in Fig. 5.6. In this stability diagram the parameters space is comprised of $2048 \times 896 \sim 2 \cdot 10^6$ solutions, having a parameters space of $\bar{\epsilon} \in [0.30, 0.58]$ and $\varphi_\Delta(0) \in \left[\frac{\pi}{2}, \pi\right]$.

5.3 Fractal dimensions

From the stability diagram in Fig. 5.6 it is possible to grasp the strong sensitivity of the system to the initial conditions, especially considering that the regions are highly disconnected and their borders are disjoint: all these aspects are signature of chaos. In order to quantify the chaoticity of the systems in this portion of the parameters space, the Hausdorff's dimensions of the region's borders has been estimated by means of the Box counting method, for which the Hausdorff's dimension δ_H is given by

$$\delta_H = \lim_{r^{-1} \to \infty} \frac{\log(\mathcal{N}_{\mathcal{B}}(r))}{\log(r^{-1})} \tag{5.3}$$

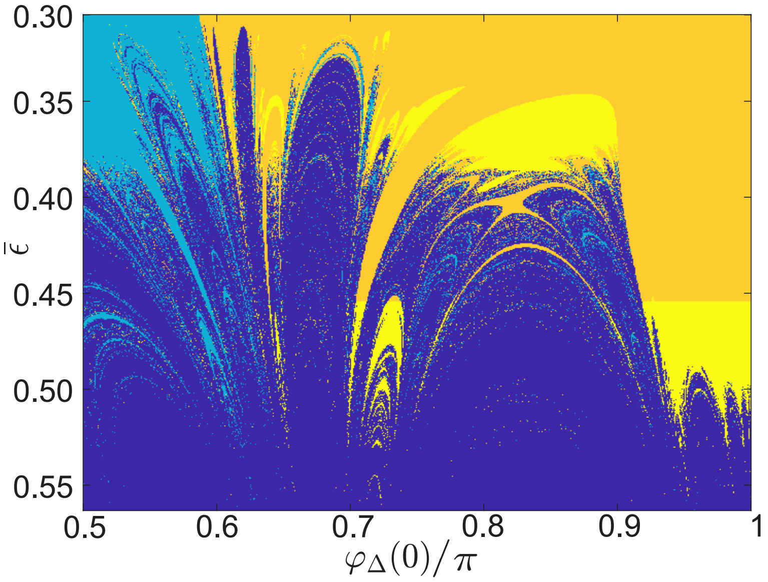

Figure 5.6: stability diagram comprised of 896×2048 points for $\varphi_\Delta \in \left[\frac{\pi}{2}, \pi\right]$ in the horizontal axis and $\bar{\epsilon} \in [0.30, 0.58]$ in the vertical axis. The space is divided into four regions by the attractors, each of them labelled by a different color: dark blue stands for unstable, light blue for 0-stable, orange for π-stable and yellow for limit cycles solutions.

where $\mathcal{N}_\mathcal{B}(r)$ is the number of non-intersecting square boxes $\mathcal{B}_r$ of linear length r needed to cover the borders of the regions. The discreteness of the parameters space does not allow exact calculation of the limit in Eq. (5.3) and, thus, the Hausdorff's dimension has been estimated as the angular coefficient of the Linear Regression curve $[log(\mathcal{N}_\mathcal{B}(r))] \simeq \bar{\delta}_H \cdot \left[\log(r^{-1})\right] + \eta_H$, where $\eta_H = o(\log(r^{-1}))$. The linear interpolation formulas for the four attractors (the plots are reported in Figs.F.2-F.3 in Appendix F) are:

- $[\log(\mathcal{N}_\mathcal{B}(r))] = 1.327 \left[\log\left(r^{-1}\right)\right] + 1.778$ for the $0-$stable solutions, giving a fractal dimension $\delta_H^0 = 1.327 \pm 0.007$;
- $[\log(\mathcal{N}_\mathcal{B}(r))] = 1.307 \left[\log\left(r^{-1}\right)\right] + 1.402$ for the $\pi-$stable solutions, giving a fractal dimension $\delta_H^\pi = 1.307 \pm 0.006$;
- $[\log(\mathcal{N}_\mathcal{B}(r))] = 1.520 \left[\log\left(r^{-1}\right)\right] + 0.876$ for unstable solutions, giving a fractal dimension $\delta_H^{unst} = 1.520 \pm 0.006$;
- $[\log(\mathcal{N}_\mathcal{B}(r))] = 1.201 \left[\log\left(r^{-1}\right)\right] + 1.679$ for the limit-cycle solutions, giving a fractal dimension $\delta_H^{cycle} = 1.201 \pm 0.004$.

5.4 Analysis of the limit-cycles

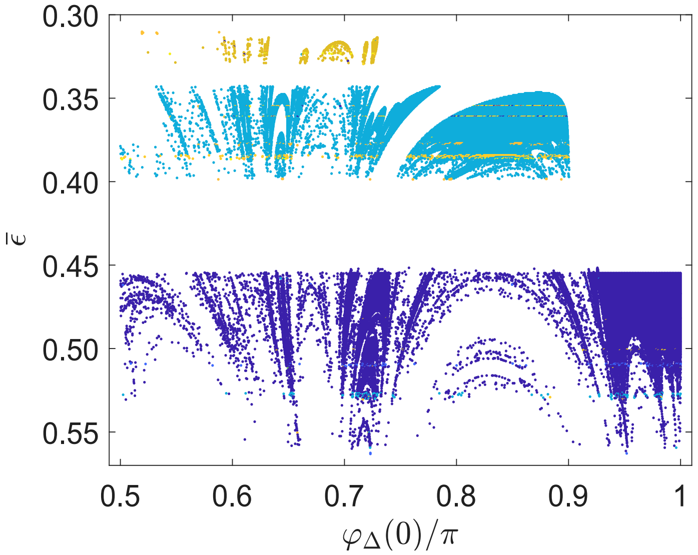

(a)

Figure 5.7: Diagram composed only by the limit-cycle solutions (labelled in yellow in Fig. 3a), where all the other attractors are discarded and depicted in white. Here, the multiple-nodding behavior of the limit-cycles is reported and, by means of different color label, they are classified in terms of their number of nods $2n$. The most recurring numbers of nods are 2 (dark blue), 6 (light blue) and 10 (orange), each of them occurring in three divided subregions. However, the limit-cycle region exhibit stripes for some specific values of $\bar{\epsilon}$ in which more complex trajectories are found.

It has been already mentioned the fact that the dynamical equation exhibits a wide landscape of limit-cycles having different multiple-nodding behavior. These periodic trajectories have been indicated as $n-$cycles, where n is the number of nods in a half-period oscillation, in such a way that the total number of nods in a complete periodic oscillation is $2n$. The definition of nods, found in the literature, is somewhat different from the one considered in this work. For instance, in the definition of the multiple-nodding behavior provided in Acheson [1995], the nods, i.e. the points in which the velocity changes sign, are counted by an observer moving up and down with the pivot, so by a non-inertial observer. In this work, a nod is considered as the point in the phase space in which the trajectory touches the $\dot{\varphi}_\Delta(t) = 0$ axis in the phase-space. Thus, the determination of the $2n$ total number of nods of the trajectory requires, from one side, the analysis of the trajectories in the Fourier space for the determination of the cycle period and, from the other side, the counting of the nods within such a period (see Appendix F for the details about numerical procedures). The counting results are reported in absolute and relative frequency in Tab. 5.1, where in the leftmost column the number n of half-oscillation nods is reported. Interestingly, this table suggests that the most frequent trajectories are $1-$cycles and $3-$cycles (see Figs. 5.3a- 5.3b), which fill almost completely the limit-cycle

Table 5.1: Number of nods, absolute and relative frequency measured in the analysis of the limit-cycles emerging from the stability diagram in Fig.5.6.

n cycle	Relative frequency	Absolute frequency
1	49.58	73915
2	0.20	294
3	47.14	70279
4	0.01	14
5	0.89	1325
6	0.58	870
7	0.01	16
9	1.33	1985
10	0.001	2
11	0.001	1
15	0.21	326
18	0.03	46

region in Fig. 5.6. The sum of all the others contributes to almost the 3% of the entire limit-cycle region. As it has been done for the main dynamical attractors — $0-$stable, $\pi-$stable, unstable and limit-cycle — the distribution of these multiple-nodding trajectories has been drawn in the parameters space. For the sake of clearness and in order to better highlight the limit-cycle solutions, all the attractors except the latter have been removed from the parameters space and the remaining limit-cycles trajectories have been labelled with their distinctive number of nods $2n$ through different colors. This particular stability diagram of the n-cycle regions, along with two insets, are reported in Figs. 5.7-5.8. As expected, $1-$cycles and $3-$cycles are the most represented and, along with a small $5-$cycle (see Fig. 5.4a) region around $\bar{\epsilon} \simeq 0.325$, divide the limit-cycles into three main subregions, respectively separated by a gap. However, higher-nodding trajectories have been found within these subregions. Some of them form clusters, like the wide $9-$cycle (see Fig. 5.4b) collection shown in orange in the inset in Fig. 5.8a, or the two stripes for $\bar{\epsilon} = 0.354838865, 0.361176755$ exhibiting an apparently disordered and very dense $n-$cycle succession, characterized by a large variety of values of n. In order to give an idea of the different $n-$cycle density in such stripes, the distribution of numbers of nods in the first stripe is reported in Fig. 5.9.

Even in this case, the geometry of these sub-regions in the parameters space seems highly fractal. Thus, following what has been done for the main attractors, Hausdorff's dimensions of the $n-$cycles borders have been determined with the same procedure used before, based on the box counting method: the linear regression estimation gives the following fractal dimensions for the subregions borders:

- $\delta_H^{1cycle} = 1.182 \pm 0.124$ for $1-$cycle;
- $\delta_H^{2cycle} = 0.870 \pm 0.184$ for $2-$cycle;
- $\delta_H^{3cycle} = 1.304 \pm 0.110$ for $3-$cycle;
- $\delta_H^{4cycle} = 0.261 \pm 0.106$ for $4-$cycle;

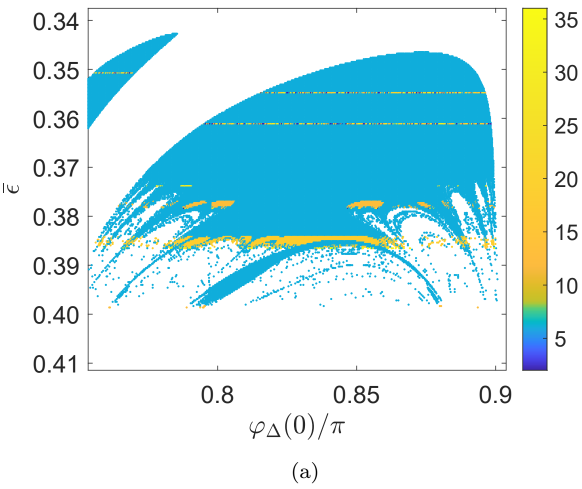

(a)

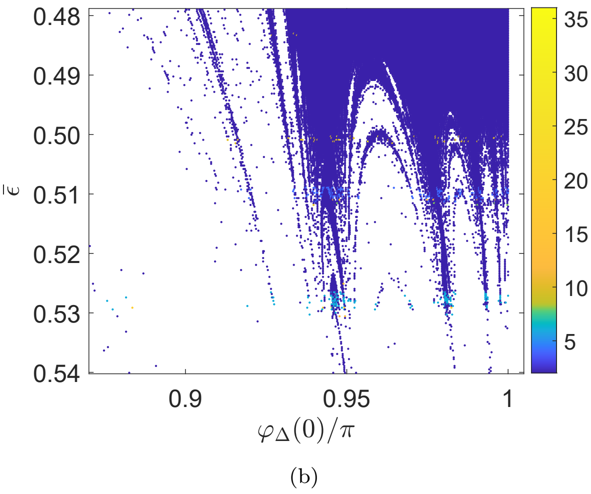

(b)

Figure 5.8: Two different insets of the limit-cycle region reported in Fig. 5.7. In (b) it is possible to see stripes of 9−cycle solutions and for $\bar{\epsilon} = 0.354838865, 0.361176755$ two narrow stripes with a large variety of $n-$cycles.

- $\delta_H^{5cycle} = 1.026 \pm 0.056$ for 5−cycle;
- $\delta_H^{6cycle} = 0.728 \pm 0.282$ for 6−cycle;
- $\delta_H^{7cycle} = 0.323 \pm 0.100$ for 7−cycle;
- $\delta_H^{9cycle} = 0.952 \pm 0.126$ for 9−cycle;
- $\delta_H^{10cycle} = 0.099 \pm 0.088$ for 10−cycle;
- $\delta_H^{11cycle} = 0.140 \pm 0.080$ for 11−cycle;

- $\delta_H^{15cycle} = 0.503 \pm 0.015$ for 15−cycle;
- $\delta_H^{18cycle} = 0.440 \pm 0.093$ for 18−cycle.

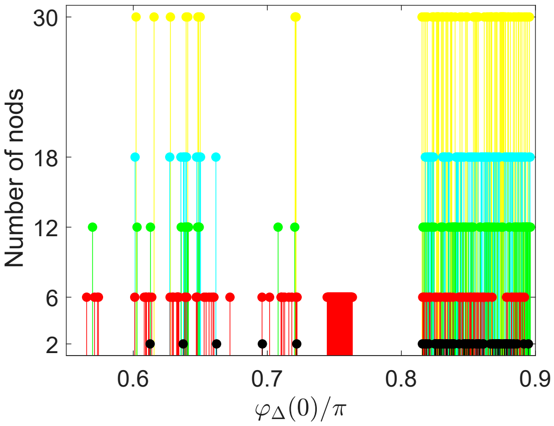

Figure 5.9: The distribution of the numbers of nods in terms of the initial phase $\varphi_\Delta(0)$ is shown in correspondence to the stripe emerging at $\bar{\epsilon} = 0.354838865$ as seen in Fig. 5.8a. A similar distribution can be obtained for the stripe at $\bar{\epsilon} = 0.361176755$.

Chapter 6

Conclusions

The aim of this thesis is to analyze, at a semiclassical level, a superconducting circuit composed of a series of two JJs in series, linked to an external voltage source. The semiclassical equations of motion, derived from the Lagrangian constrained by the external voltage, have been rearranged in such a way to give a dynamical equation for the superconducting island phase. This dynamical equation has been mapped into the equation of a rotor with moving pivot, meaning that the superconducting circuit under analysis behaves like a zero-gravity Kapitza pendulum. This connection seems, as far as it is known, as a novelty in the field of the Josephson junction's dynamics studies because no mention of this correspondence has been found in the literature related to this topic. There, the connection between superconducting circuits with a single Josephson junction and the force-driven pendulum has been drawn in many works and what has been found in this thesis could be seen as an extension of this well-studied correspondence.

A very large literature on the Kapitza pendulum dynamics has been found and the dynamical properties of this mechanical problem seem well-understood. In particular, the system dynamics have been well-investigated as a function of gravity and the oscillation driving amplitude: the dynamical landscape emerging from this choice of parameters exhibits several different attractors and a significant chaotic attitude. From the point of view of the superconducting circuit under analysis, this set of parameters is not meaningful because the systems have different physical natures. For the superconducting circuit, the chosen dynamical parameters are the dimensionless driving amplitude $\bar{\epsilon}$ and the initial value of the phase $\varphi_{\Delta}(0)$, in such a way to analyze how the external voltage affects the superconducting island current: with this parameters space, the comparison of results in the KP literature can be done just partially. Numerical simulations have given the typical KP attractors but the obtained stability diagrams are different from the one usually observed in the usual Kapitza description because of the different parameters space used here. The distribution of the attractors in the stability diagrams shows a very intricate chaotic behavior and strong sensitivity to the initial conditions: Hausdorff's dimensions of the different regions of the attractors have been computed, having values in the range $1.201 < \delta_H < 1.520$, i.e. very irregular and discontinuous borders of those regions, meaning that a small variation of the parameters can lead to a complete different type of solution of the superconducting phase. Another remarkable result is the evidence of multiple-nodding behavior (Acheson [1995]) of the limit-cycles. These trajectories differ in their distinctive number of nods, in the same multiple-nodding fashion encountered in the Kapitza pendulum dynamics. However, this feature of the limit-cycles discriminates many fractal sub-regions within the limit-cycle region in the stability diagram: Hausdorff's dimensions of these sub-regions still have non-integer values in the range $0.140 < \delta_H^{cy} < 1.304$, signalling again high sensitivity to initial conditions, leading to chaotic dynamics.

The superconducting circuit under analysis has the same lumped element description of a SSET. However, the semiclassical dynamics of the phase can emerge from a circuit like the SSET only in the specific physical regime in which the Josephson energy dominates the charging energy, i.e. $E_J \gg E_C$ giving a junction impedance lower than the quantum resistance ($\mathcal{Z} \ll R_K$), essentially the opposite regime in which a SSET normally operates, i.e. Coulomb blockade regime, holding for $E_J \ll E_C$ ($\mathcal{Z} \gg R_K$). From the practical point of view, a small impedance be achieved by adding a large shunting capacitance or by taking even macroscopic junctions: the ideal range of values of the Josephson junction's section $10^{-2} < \Sigma < 1$ mm^2 has been estimated.

The analysis above discussed can be improved from different points of view. The most interesting advancements could concern the numerical simulations. What has been done in this thesis is investigating the superconducting phase dynamics maintaining a fixed value of the dissipation parameter $\gamma = 10^2$, i.e. the dissipation does not play any role in this analysis of the dynamics. However, just a few simulations are sufficient to show that the dynamics and the trajectories are affected by variation of the dissipation. For instance, the dynamical parameters space could be improved to a three-dimensional space comprehending the dissipation parameters. It could be investigated the way in which the distribution of the attractors in the stability diagram changes, like the one in Fig. 5.6, in relation to different dissipative coefficients and to what extent the fractal geometry is altered. Moreover, it could be interesting to understand in which way the different dissipation regimes affect the limit-cycles attractors and their multiple-nodding behavior.

Appendix A

Josephson relations

The Hamiltonian describing the Cooper pairs tunnelling, at least considering single CP's tunnelling as the leading process, is equivalent to the Tight-Binding Hamiltonian describing the nearest-neighbour hopping in a one-dimensional lattice composed just of two sites, 1 and 2:

$$\hat{\mathcal{H}} = -\frac{E_J}{2}\sum_m |m+1\rangle\langle m| + |m\rangle\langle m+1|, \tag{A.1}$$

where $|m\rangle) = |N_1 + m\rangle|N_2 - m\rangle$ is a quantum state describing the flow of m Cooper pairs through the junction, N_1 and N_2 are explicitly the numbers of CPs in the two superconducting electrodes. The number operator, measuring the number of tunnelled CPs, is $\hat{N} = \sum_{m=-\infty}^{+\infty} m|m\rangle\langle m|$. The Hamiltonian operator can be easily expressed in terms of creation and annihilation operators

$$\hat{\mathcal{H}} = -\frac{E_J}{2\sqrt{N_1 N_2}}\left[\hat{a}_1^\dagger \hat{a}_2 + \hat{a}_1 \hat{a}_2^\dagger\right], \tag{A.2}$$

recalling that the action of the single-site operators are $\hat{a}_1|N_1\rangle = \sqrt{N_1}|N_1 - 1\rangle$ and $\hat{a}_1^\dagger|N_1\rangle = \sqrt{N_1+1}|N_1+1\rangle$ for the site 1 and equal expressions hold for site 2. In this picture the single electrode number operators become

$$\hat{N}_1|N_1\rangle = \hat{a}_1^\dagger \hat{a}_1|N_1\rangle = N_1|N_1\rangle, \tag{A.3}$$

$$\hat{N}_2|N_2\rangle = \hat{a}_2^\dagger \hat{a}_2|N_2\rangle = N_2|N_2\rangle, \tag{A.4}$$

$$\tag{A.5}$$

and the operator counting the number of CPs tunnelled from left to right takes the form

$$\hat{N} = \hat{N}_1 - \hat{N}_2, \tag{A.6}$$

giving

$$\hat{N}|N_1, N_2\rangle = (N_1 - N_2)|N_1, N_2\rangle = m|N_1, N_2\rangle. \tag{A.7}$$

It is straightforward to see that the Hamiltonian does not act diagonally on the states $|N_1, N_2\rangle$, since

$$-\frac{E_J}{2\sqrt{N_1 N_2}}\left[\hat{a}_1^\dagger \hat{a}_2 + \hat{a}_1 \hat{a}_2^\dagger\right]|N_1, N_2\rangle = \tag{A.8}$$

$$= -\frac{E_J}{2}|N_1+1, N_2-1\rangle - \frac{E_J}{2}|N_1-1, N_2+1\rangle. \tag{A.9}$$

As usual for a single-mode physical system, it could be convenient to introduce an observable conjugated to the number operator $\hat{N}$ which diagonalizes the Hamiltonian in Eq. (A.1) and fulfils the commutator $[\hat{\varphi}, \hat{N}] = i$. However, it has been proved that such a phase operator and phase states are not quantum mechanical meaningful (Susskind and Glogower [1964]). The fact that the eigenvalues of $\hat{N}$ go from 0 to $+\infty$ makes it impossible to define any phase operator having the properties required to be conjugated of $\hat{N}$. One of the possible solutions, suggested in Pegg and Barnett [1989], is to restrict the number operator to a $s+1$ space, given that s is the maximum eigenvalue of $\hat{N}$, and consequently define a phase state

$$|\varphi\rangle = \lim_{s\to\infty} \frac{1}{(1+s)^{1/2}} \sum_{m=0}^{s} e^{im\varphi}|m\rangle, \tag{A.10}$$

The application of the Hamiltonian on the phase states gives the Josephson element's energy Eq. (2.5). Explicit calculations give

$$-\frac{E_J}{2}\left(\hat{a}_1^\dagger \hat{a}_2 + \hat{a}_1 \hat{a}_2^\dagger\right)|\varphi\rangle = \tag{A.11}$$

$$-\frac{E_J}{2} \lim_{s\to\infty} \frac{1}{(1+s)^{1/2}} \sum_{m=0}^{s} e^{im\varphi}\left(\hat{a}_1^\dagger \hat{a}_2 + \hat{a}_1 \hat{a}_2^\dagger\right)|m\rangle = \tag{A.12}$$

$$-\frac{E_J}{2} \lim_{s\to\infty} \frac{1}{(1+s)^{1/2}} \sum_{m=0}^{s} e^{im\varphi}\{|m+1\rangle + |m-1\rangle\}, \tag{A.13}$$

which, recalling the definition of the operators $e^{\pm i\hat{\varphi}}$ (given in Pegg and Barnett [1989]) as creation and destruction operator

$$e^{\pm i\hat{\varphi}}|m\rangle = |m \pm 1\rangle, \tag{A.14}$$

give the eigenvalues equation of the Hamiltonian

$$\hat{H}|\varphi\rangle = -E_J \cdot \lim_{s\to\infty} \frac{1}{(1+s)^{1/2}} \sum_{m=0}^{s} e^{im\varphi}\left[\frac{e^{i\hat{\varphi}} + e^{-i\hat{\varphi}}}{2}\right]|m\rangle = \tag{A.15}$$

$$= -E_J \cos(\hat{\varphi})|\varphi\rangle = -E_J \cos(\varphi)|\varphi\rangle \tag{A.16}$$

where $\cos(\hat{\varphi}) = \left(e^{i\hat{\varphi}} + e^{-i\hat{\varphi}}\right)/2$ is the cosine operator.

The First Josephson Relation consists of the non-linear expression relating the flux and the superconducting current flowing through the junction. The current operator is simply given by $\hat{I} = (-2e)\dot{\hat{N}}$, where $\dot{\hat{N}}$ is the operator representing the time derivative of the number of tunnelled Cooper pairs. Its explicit expression fulfills the Heisenberg equation

$$i\hbar\dot{\hat{N}} = \left[\hat{N}, \hat{\mathcal{H}}\right], \tag{A.17}$$

where the commutator $\left[\hat{N}, \hat{\mathcal{H}}\right] = \hat{\mathcal{H}}\hat{N} - \hat{N}\hat{\mathcal{H}}$ is explicitly computed

$$\begin{split}\left[\hat{N}, \hat{\mathcal{H}}\right] = \left[\hat{N}_1 - \hat{N}_2, \hat{\mathcal{H}}\right] = \left[\hat{N}_1, \hat{\mathcal{H}}\right] - \left[\hat{N}_2, \hat{\mathcal{H}}\right] = \\ -\frac{E_J}{2\sqrt{N_1 N_2}}\left\{\left[a_1^\dagger a_1, a_1^\dagger a_2 + a_1 a_2^\dagger\right] - \left[a_2^\dagger a_2, a_1^\dagger a_2 + a_1 a_2^\dagger\right]\right\}.\end{split} \tag{A.18}$$

Recalling the standard commutation relations $\left[a_i^\dagger, a_j\right] = \delta_{ij}$ and $\left[a_i^\dagger, a_j^\dagger\right] = [a_i, a_j] = 0$, the four types of commutators appearing in the commutator (A.17) simplifies as

$$\begin{aligned}&\left[\hat{a}_i^\dagger \hat{a}_i, \hat{a}_i^\dagger \hat{a}_j\right] = \hat{a}_i^\dagger \left[\hat{a}_i, \hat{a}_i^\dagger \hat{a}_j\right] + \left[\hat{a}_i^\dagger, \hat{a}_i^\dagger \hat{a}_j\right] \hat{a}_i = \\ &= \hat{a}_i^\dagger \hat{a}_i^\dagger \left[\hat{a}_i, \hat{a}_j\right] + \hat{a}_i^\dagger \left[\hat{a}_i, \hat{a}_i^\dagger\right] \hat{a}_j + \hat{a}_i^\dagger \left[\hat{a}_i^\dagger, \hat{a}_j\right] \hat{a}_i + \left[\hat{a}_i^\dagger, \hat{a}_i^\dagger\right] \hat{a}_j \hat{a}_i = \\ &= \hat{a}_i^\dagger \hat{a}_j\end{aligned} \tag{A.19}$$

$$\begin{aligned}&\left[\hat{a}_i^\dagger \hat{a}_i, \hat{a}_i \hat{a}_j^\dagger\right] = \hat{a}_i^\dagger \left[\hat{a}_i, \hat{a}_i \hat{a}_j^\dagger\right] + \left[\hat{a}_i^\dagger, \hat{a}_i \hat{a}_j^\dagger\right] \hat{a}_i = \\ &= \hat{a}_i^\dagger \hat{a}_i \left[\hat{a}_i, \hat{a}_j^\dagger\right] + \hat{a}_i^\dagger \left[\hat{a}_i, \hat{a}_i\right] \hat{a}_j^\dagger + \hat{a}_i \left[\hat{a}_i^\dagger, \hat{a}_j^\dagger\right] \hat{a}_i + \left[\hat{a}_i^\dagger, \hat{a}_i\right] \hat{a}_j^\dagger \hat{a}_i = \\ &= -\hat{a}_i \hat{a}_j^\dagger\end{aligned} \tag{A.20}$$

$$\begin{aligned}&\left[\hat{a}_i^\dagger \hat{a}_i, \hat{a}_j \hat{a}_i^\dagger\right] = \hat{a}_i^\dagger \left[\hat{a}_i, \hat{a}_j \hat{a}_i^\dagger\right] + \left[\hat{a}_i^\dagger, \hat{a}_j a_i^\dagger\right] \hat{a}_i = \\ &= \hat{a}_i^\dagger \hat{a}_j \left[\hat{a}_i, \hat{a}_i^\dagger\right] + \hat{a}_i^\dagger \left[\hat{a}_i, \hat{a}_j\right] \hat{a}_i^\dagger + \hat{a}_j \left[\hat{a}_i^\dagger, \hat{a}_i^\dagger\right] \hat{a}_i + \left[\hat{a}_i^\dagger, \hat{a}_j\right] \hat{a}_i^\dagger \hat{a}_i = \\ &= \hat{a}_i \hat{a}_j^\dagger\end{aligned} \tag{A.21}$$

$$\begin{aligned}&\left[\hat{a}_i^\dagger \hat{a}_i, \hat{a}_j^\dagger \hat{a}_i\right] = \hat{a}_i^\dagger \left[\hat{a}_i, \hat{a}_j^\dagger \hat{a}_i\right] + \left[\hat{a}_i^\dagger, \hat{a}_j^\dagger \hat{a}_i\right] \hat{a}_i = \\ &= \hat{a}_i^\dagger \hat{a}_j^\dagger \left[\hat{a}_i, \hat{a}_i\right] + \hat{a}_i^\dagger \left[\hat{a}_i, \hat{a}_j^\dagger\right] \hat{a}_i + \hat{a}_j^\dagger \left[\hat{a}_i^\dagger, \hat{a}_i\right] \hat{a}_i + \left[\hat{a}_i^\dagger, \hat{a}_j^\dagger\right] \hat{a}_i \hat{a}_i = \\ &= -\hat{a}_i^\dagger \hat{a}_j\end{aligned} \tag{A.22}$$

Thus, expression (A.17) becomes

$$\left[\hat{N}, \hat{\mathcal{H}}\right] = -E_J \left[\hat{a}_1^\dagger \hat{a}_2 - \hat{a}_1 \hat{a}_2^\dagger\right] \tag{A.23}$$

and the current operator acquires the expression

$$\hat{I} = -\frac{(2e)E_J}{i\hbar} \left[\hat{a}_1^\dagger \hat{a}_2 - \hat{a}_1 \hat{a}_2^\dagger\right] = -\frac{2\pi E_J}{\Phi_0} \left[\frac{\hat{a}_1^\dagger \hat{a}_2 - \hat{a}_1 \hat{a}_2^\dagger}{i}\right]. \tag{A.24}$$

The application of the current operator on the phase states in Eq. (A.10) reveals the sine operator and gives the First Josephson relation:

$$\hat{I}|\varphi\rangle = \frac{2\pi E_J}{\Phi_0} \sin(\hat{\varphi})|\varphi\rangle = I_C \sin(\varphi)|\varphi\rangle \tag{A.25}$$

The derivation of the Second Josephson Relation requires considering an external field applied to the Josephson junction through a constant voltage $\mathcal{V}$, in order for the Hamiltonian (A.1) to acquire a term linear in the number operator:

$$\begin{aligned}\hat{\mathcal{H}} &= \hat{\mathcal{H}}_0 - (2e)\mathcal{V}\hat{N} = \\ &= \frac{E_J}{2} \left[\hat{a}_1^\dagger \hat{a}_2 + \hat{a}_1 \hat{a}_2^\dagger\right] - (2e)\mathcal{V} \left[\hat{a}_1^\dagger \hat{a}_1 + \hat{a}_2^\dagger \hat{a}_2\right]\end{aligned} \tag{A.26}$$

The appearance of the new quadratic is such that the cosine operator does not commute with the Hamiltonian, so its time-evolution can be explicitly computed through the usual Heisenberg equation and the commutation relations (A.19)-(A.20)-(A.21)-(A.22), the relation

$$\begin{aligned}\frac{d}{dt}\cos(\hat{\varphi}) &= -\frac{i}{\hbar}\left[\cos(\hat{\varphi}), \hat{\mathcal{H}}\right] = \frac{(2e)i\mathcal{V}}{\hbar E_J}\left[\hat{\mathcal{H}}_0, \hat{N}\right] = \\ &= \frac{(2e)i}{\hbar}\mathcal{V}\left[\hat{a}_1^\dagger \hat{a}_2 - \hat{a}_1 \hat{a}_2^\dagger\right] = \frac{(2e)}{\hbar}\mathcal{V}\sin(\hat{\varphi})\end{aligned} \tag{A.27}$$

Furthermore, exploiting the derivation chain rule

$$\frac{d}{dt}\cos(\hat{\varphi}) = \sin(\hat{\varphi})\dot{\hat{\varphi}}, \tag{A.28}$$

the Heisenberg equation (A.27) gives the time evolution of the phase operator

$$\dot{\hat{\varphi}} = \frac{2\pi}{\Phi_0}\mathcal{V}, \tag{A.29}$$

which represents the Second Josephson Relation.

Appendix B

Devoret's procedure on the CPB

The circuit in Fig. B represents the Cooper Pair Box. Introducing the voltage source in the Hamiltonian formalism of the circuit can be done in different ways. Here, the Devoret's procedure will be applied. In shorthand, it consists in considering the voltage source to be fully buffered. Thus, the source is substituted with a buffer capacitor and then, in the final steps of the calculations, the capacitance is sent to infinity. The left expression represents the CPB Hamiltonian. The substitution done by Devoret produces the circuital diagram given in Fig. 2.3, where the buffer capacitor is indicated as C_A. The kinetic contribution to the Lagrangian is fully capacitative, taking the form

$$\mathcal{T} = \mathcal{T}\left(\phi_1, \phi_2, \dot{\phi_1}, \dot{\phi_2}\right) = \frac{1}{2}C_\mathrm{A}\dot{\phi_1}^2 + \frac{1}{2}C_\mathrm{g}\left(\dot{\phi_1} - \dot{\phi_2}\right)^2 + \frac{1}{2}C_\mathrm{J}\dot{\phi_2}^2 = \frac{1}{2}\vec{\dot{\phi}}^T\hat{C}\vec{\dot{\phi}}, \tag{B.1}$$

where the matricial notation has been used in order to simplify the calculations, giving that $\vec{\dot{\phi}} = \begin{pmatrix}\dot{\phi_1}\\ \dot{\phi_2}\end{pmatrix}$ and

$$\hat{C} = \begin{pmatrix} C_\mathrm{g} + C_\mathrm{A} & -C_\mathrm{g} \\ -C_\mathrm{g} & C_\mathrm{J} + C_\mathrm{g} \end{pmatrix}. \tag{B.2}$$

Since the potential term is independent of $\vec{\dot{\phi}}$, the momenta conjugated to the fluxes $\vec{\phi}$ are simply derived differentiating the kinetic energy $\vec{Q} = \nabla_{\dot{\phi}}\mathcal{T} = \hat{C}\vec{\dot{\phi}}$, giving

$$\vec{\dot{\phi}} = \left[\hat{C}\right]^{-1}\vec{Q}, \tag{B.3}$$

where $\hat{C}^{-1}$ represents the inverse capacitance matrix, explicitly given by

$$\hat{C}^{-1} = \left[C_\mathrm{J}(C_\mathrm{g} + C_\mathrm{A}) + C_\mathrm{g}C_\mathrm{A}\right]^{-1}\begin{pmatrix} C_\mathrm{J} + C_\mathrm{g} & C_\mathrm{g} \\ C_\mathrm{g} & C_\mathrm{g} + C_\mathrm{A} \end{pmatrix} = \begin{pmatrix} \frac{1}{C_{11}} & \frac{1}{C_{12}} \\ \frac{1}{C_{21}} & \frac{1}{C_{22}} \end{pmatrix}. \tag{B.4}$$

The kinetic energy in terms of the conjugated momenta becomes

$$\mathcal{T} = \frac{1}{2}\vec{Q}^T\left[\hat{C}\right]^{-1}\vec{Q} = \frac{1}{2C_{11}}Q_1^2 + \frac{1}{2C_{22}}Q_2^2 + \frac{1}{C_{12}}Q_1Q_2. \tag{B.5}$$

Defining $V_{\mathrm{g}} = \frac{Q_2}{C_{12}} \frac{C_{\mathrm{g}}+C_{\mathrm{A}}}{C_{\mathrm{g}}} = \frac{Q_{\mathrm{g}}}{C_{11}}$, the charge on the second node is rewritten as $Q_2 = C_{11} V_{\mathrm{g}}$. Pluggin the last expression in the kinetic energy

$$\begin{aligned} \mathcal{T} =& \frac{1}{2C_{11}} Q_1^2 + \frac{1}{2C_{22}} Q_2^2 + \frac{C_{11}}{C_{12}} Q_1 = \\ =& \frac{1}{2C_{11}} Q_1^2 + \frac{1}{2C_{22}} Q_2^2 + \frac{1}{2C_{12}} Q_1 V_{\mathrm{g}} = \\ =& \underbrace{\frac{1}{2C_{22}} \left(Q_1 + \frac{C_{11} C_{22}}{C_{12}} V_{\mathrm{g}} \right)^2}_{\mathrm{A}} + \underbrace{\frac{1}{2} V_{\mathrm{g}}^2 \left(C_{11} + \frac{C_{11}^2}{C_{12}^2} C_{22} \right)}_{\mathrm{B}} . \end{aligned} \tag{B.6}$$

The contribution A to the kinetic energy can be simplified defining ($Q_{\mathrm{g}} = \frac{C_{11} C_{22}}{C_{12}} V_{\mathrm{g}}$. The latter defines the gate charge n_{g} which, skipping some calculations, becomes $Q_{\mathrm{g}} = -C_g V_{\mathrm{g}}$. The term B also can be reduced to the form $\frac{1}{2} \frac{C_{11} C_{22}}{C_{\mathrm{g}}+C_{\mathrm{A}}} V_{\mathrm{g}}^2$.

Taking the limit $C_{\mathrm{A}} \to \infty$, the inverse capacitance matrix components tend to

$$\frac{1}{C_{11}} \to 0, \tag{B.7}$$

$$\frac{1}{C_{12}} = \frac{1}{C_{21}} \to 0, \tag{B.8}$$

$$\frac{1}{C_{22}} \to \frac{1}{C_{\Sigma}} \frac{1}{C_{\mathrm{J}} + C_{\mathrm{g}}}, \tag{B.9}$$

leading to the divergence of term B, which can though neglect since it is constant, not depending on the Lagrangian variables, and it disappears after energy rescaling. Note that the gate charge Q_{g} remains finite in this limit.

Recalling that the charge variables can be written in terms of the CPs numbers, the final expression of the CPB Hamiltonian is given by

$$\mathcal{H} = 4E_{\mathrm{C}\Sigma} \left(n_1 - n_{\mathrm{g}} \right)^2 - E_{\mathrm{J}} \cos\left(\varphi_1 \right), \tag{B.10}$$

where $E_{\mathrm{C}\Sigma} = \frac{e^2}{2C_{\Sigma}}$, $n_1 = \frac{Q_1}{2e}$ and $n_{\mathrm{g}} = \frac{Q_{\mathrm{g}}}{2e}$.

Appendix C

Devoret's procedure for the SC

In this Appendix, Devoret's procedure is followed for deriving the superconducting phase equation for the two voltage-biased JJs in series depicted in Fig. 1.1. This has been made for a double purpose. Foremost, the application of Devoret's procedure to the superconducting circuit analyzed in this thesis gives a different point of view of the problem. On the other hand, it can be used to check the accuracy of the Lagrangian multipliers methods implemented in?? and whether it has been able to reproduce the correct dynamical equation for the superconducting phase. Essentially, in this procedure the enforcement of the external voltage constraint $V_{\mathrm{g}} = \dot{\phi}_{\mathrm{g}}$ (for the grounding, $\dot{\phi}_o$ has been taken equal to zero from the beginning) in the Hamiltonian is obtained, in the first place, substituting the voltage source with a capacitance C_{g} and taking, after all the calculations, the limit $C_{\mathrm{g}} \to \infty$. Following this scheme, the kinetic term takes the form

$$\mathcal{T} = \frac{1}{2}\dot{\vec{\phi}}^T \mathcal{C} \dot{\vec{\phi}} = \frac{1}{2} C_{\mathrm{g}} \dot{\phi}_{\mathrm{g}}^2 + \frac{1}{2} C_{\mathrm{J1}} \left(\dot{\phi}_{\mathrm{g}} - \dot{\phi}_{\mathrm{I}} \right)^2 + \frac{1}{2} C_{\mathrm{J2}} \dot{\phi}_{\mathrm{I}}^2, \tag{C.1}$$

where $\mathcal{C}$ is the capacitance matrix

$$\mathcal{C} = \begin{pmatrix} C_{\mathrm{J1}} + C_{\mathrm{g}} & -C_{\mathrm{J1}} \\ -C_{\mathrm{J1}} & C_{\mathrm{J1}} + C_{\mathrm{J2}} \end{pmatrix} \tag{C.2}$$

and $\dot{\vec{\phi}} = \begin{pmatrix} \dot{\phi}_{\mathrm{g}} \\ \dot{\phi}_{\mathrm{I}} \end{pmatrix}$.

The Lagrangian $\mathcal{L} = \mathcal{L}(\vec{\phi}, \dot{\vec{\phi}})$ is $\mathcal{L} = \frac{1}{2}\dot{\vec{\phi}}^T \mathcal{C} \dot{\vec{\phi}} - \mathcal{U}$, where the potential part is $\mathcal{U} = -E_{J_1} \cos\left(\frac{2\pi}{\Phi_0} (\phi_{\mathrm{g}} - \phi_{\mathrm{I}}) \right) - E_{J_2} \cos\left(\frac{2\pi}{\Phi_0} \phi_{\mathrm{I}} \right)$. The charge Q_{g} on the lead g and Q_{I} on the island I are the momenta conjugated to the flux, easily obtained by the Lagrangian

$$\vec{Q} = \vec{\nabla}_{\dot{\phi}} \mathcal{L} = \begin{pmatrix} \frac{\partial \mathcal{L}}{\partial \dot{\phi}_{\mathrm{g}}} \\ \frac{\partial \mathcal{L}}{\partial \dot{\phi}_{\mathrm{I}}}, \end{pmatrix} = \mathcal{C} \dot{\vec{\phi}} \tag{C.3}$$

Thus, the Hamiltonian $\mathcal{H} = \mathcal{H}(\vec{Q}, \vec{\phi})$ takes the form

$$\mathcal{H} = \dot{\vec{\phi}}^T \vec{Q} - \mathcal{L} = \frac{1}{2} \vec{Q}^T [\mathcal{C}]^{-1} \vec{Q} + \mathcal{U}, \tag{C.4}$$

where $\mathcal{C}^{-1}$ is the inverse capacitance matrix

$$[\mathcal{C}]^{-1} = \begin{pmatrix} \frac{1}{C_{11}} & \frac{1}{C_{12}} \\ \frac{1}{C_{12}} & \frac{1}{C_{22}}, \end{pmatrix} \tag{C.5}$$

written in terms of the quantities

$$\frac{1}{C_{11}} = \frac{C_{\mathrm{J1}} + C_{\mathrm{J2}}}{C_{\mathrm{J1}}C_{\mathrm{J2}} + C_{\mathrm{g}}(C_{\mathrm{J1}} + C_{\mathrm{J2}})}, \tag{C.6}$$

$$\frac{1}{C_{12}} = \frac{C_{\mathrm{J1}}}{C_{\mathrm{J1}}C_{\mathrm{J2}} + C_{\mathrm{g}}(C_{\mathrm{J1}} + C_{\mathrm{J2}})}, \tag{C.7}$$

$$\frac{1}{C_{22}} = \frac{C_{\mathrm{J1}} + C_{\mathrm{g}}}{C_{\mathrm{J1}}C_{\mathrm{J2}} + C_{\mathrm{g}}(C_{\mathrm{J1}} + C_{\mathrm{J2}})}. \tag{C.8}$$

Explicitly,

$$\mathcal{H} = \frac{1}{2C_{11}}Q_{\mathrm{g}}^2 + \frac{1}{2C_{22}}Q_{\mathrm{I}}^2 + \frac{1}{C_{12}}Q_{\mathrm{g}}Q_{\mathrm{I}} + \mathcal{U}. \tag{C.9}$$

Introducing the nominal bias voltage $V_{\mathrm{g}} = \frac{Q_{\mathrm{g}}}{C_{11}}$ and recalling $n = \frac{Q_{\mathrm{I}}}{2e}$ the Hamiltonian takes the final expression

$$\mathcal{H} = 4E_{\mathrm{C}_{22}}\left(n - \bar{n}_{\mathrm{g}}\right)^2 + \frac{1}{2}\frac{C_{11}C_{22}}{C_{12}}V_{\mathrm{g}}^2 + \mathcal{U}, \tag{C.10}$$

where $\bar{n}_{\mathrm{g}} = -\frac{C_{11}C_{22}}{C_{12}}\frac{V_{\mathrm{g}}}{2e}$ and $E_{\mathrm{C}_{22}} = \frac{e^2}{2C_{22}}$.

In the limit of $C_{\mathrm{g}} \to \infty$, the quantities defined above become

$$\frac{1}{C_{11}} \to 0, \tag{C.11}$$

$$\frac{1}{C_{12}} \to 0, \tag{C.12}$$

$$\frac{1}{C_{22}} \to \frac{1}{C_{\Sigma}} = \frac{1}{C_{\mathrm{J1}} + C_{\mathrm{J2}}}, \tag{C.13}$$

$$E_{\mathrm{C}_{22}} \to E_{\mathrm{C}} = \frac{e^2}{2C_{\Sigma}} = \frac{e^2}{2(C_{\mathrm{J1}} + C_{\mathrm{J2}})}, \tag{C.14}$$

and, as a consequence, the gate charge $\bar{n}_{\mathrm{g}}$ remains finite

$$\bar{n}_{\mathrm{g}} \to -\frac{C_1}{2e}V_{\mathrm{g}}, \tag{C.15}$$

whereas the second term in Eq. (C.10) diverges. However, this energy contribution is constant, since it does not depend on the conjugated variables. Thus, it can be interpreted as a constant shift in the energy and, for this reason, it is neglected.

The final form of the Hamiltonian is

$$\begin{aligned} \mathcal{H} =& 4E_{\mathrm{C}_{\Sigma}}\left(n - \bar{n}_{\mathrm{g}}\right)^2 \\ & - E_{J1}\cos\left[\frac{2\pi}{\Phi_0}(\phi_{\mathrm{g}} - \phi_{\mathrm{I}})\right] - E_{J2}\cos\left(\frac{2\pi}{\Phi_0}\phi_{\mathrm{I}}\right). \end{aligned} \tag{C.16}$$

The equations of motion for n, φ_{g} and φ_{I} are derived through the Poisson's bracket defined in Sec. 3.2.2:

$$\dot{n} = \frac{E_{J1}}{\hbar}\sin(\varphi_{\mathrm{g}} - \varphi_{\mathrm{I}}) - \frac{E_{\mathrm{J}2}}{\hbar}\sin(\varphi_{\mathrm{I}}), \tag{C.17}$$

$$\dot{\varphi}_{\mathrm{g}} = \frac{2\pi}{\Phi_0}V_{\mathrm{g}} = \omega_{\mathrm{g}}, \tag{C.18}$$

$$\dot{\varphi}_{\mathrm{I}} = \frac{8E_{\mathrm{C}_\Sigma}}{\hbar}(n - \bar{n}_{\mathrm{g}}). \tag{C.19}$$

Direct integration of Eq. (C.17) gives that $\varphi_{\mathrm{g}}(t) = \varphi_{\mathrm{g}}(0) + \omega_{\mathrm{g}}t$. Differentiation of Eq. (C.19) gives

$$\ddot{\varphi}_{\mathrm{I}} = \frac{8E_{C_\Sigma}}{\hbar}\dot{n} = -\frac{8E_{\mathrm{C}_\Sigma}}{\hbar^2}\left[E_{\mathrm{J}2}\sin(\varphi_{\mathrm{I}}) - E_{J1}\sin(\varphi_{\mathrm{I}} - \varphi_{\mathrm{g}})\right] \tag{C.20}$$

where the second expression has been obtained through insertion of Eq. (C.17). Supposing now to deal with identical Josephson junctions, i.e. $E_{\mathrm{J}1} = E_{\mathrm{J}2} = E_{\mathrm{J}}$ and $E_{C_\Sigma} \to E_C$

$$\ddot{\varphi}_{\mathrm{I}} = -\frac{8E_{\mathrm{C}}E_J}{\hbar^2}\left[\sin(\varphi_{\mathrm{I}}) - \sin(\varphi_{\mathrm{I}} - \varphi_{\mathrm{g}})\right], \tag{C.21}$$

and then exploiting the trigonometric formula $\sin(A) - \sin(B) = 2\cos\left(\frac{A+B}{2}\right)\sin\left(\frac{A-B}{2}\right)$, the superconducting phase equation takes the final form

$$\ddot{\varphi}_{\Delta} = -2\Omega_{\mathrm{J}}^2\cos\left[\frac{\varphi_{\mathrm{g}}(t)}{2}\right]\sin\varphi_{\Delta}, \tag{C.22}$$

where the Josephson plasma frequency $\Omega_{\mathrm{J}} = \frac{\sqrt{8E_{\mathrm{C}}E_{\mathrm{J}}}}{\hbar}$ naturally emerges from the calculations. Equation (C.22) matches with the analoguos equation derived with the Langrangian multipliers method Eq. (**??**), which means that the latter correctly describes the superconducting circuit under analysis.

Appendix D

SC Hamiltonian and dynamical equation

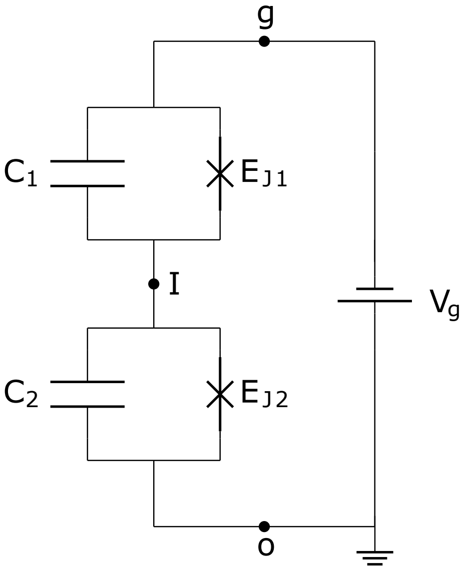

Figure D.1: Superconducting circuit composed of two JJs in series, linked to an external voltage source. The node *o* is grounded.

The complete calculations leading to the SC Hamiltonian are reported in this chapter of the Appendix. First, it is necessary to recall the expression of the constrained SC Lagrangian

$$\begin{aligned}
\mathcal{L}(\vec{\phi},\dot{\vec{\phi}}) &= \mathcal{L}_0 + \mathcal{Q}\cdot\mathcal{V}\left(\dot{\phi}_{\mathrm{g}},\dot{\phi}_o\right)\\
&= \mathcal{T} - \mathcal{U} + \mathcal{Q}\cdot\mathcal{V}\left(\dot{\phi}_{\mathrm{g}},\dot{\phi}_o\right)\\
&= \frac{1}{2}C_1(\dot{\phi}_{\mathrm{g}}+\dot{\phi}_I)^2 + \frac{1}{2}C_2(\dot{\phi}_I-\dot{\phi}_o)^2\\
&+ E_{J1}\cos\left(\frac{2\pi}{\Phi_0}(\phi_{\mathrm{g}}-\phi_I)\right) + E_{J2}\cos\left(\frac{2\pi}{\Phi_0}(\phi_I-\phi_o)\right)\\
&+ \mathcal{Q}\left(\dot{\phi}_{\mathrm{g}}-\dot{\phi}_o-V_{\mathrm{g}}\right),
\end{aligned} \tag{D.1}$$

and the expressions defining the charges, derived inverting the momenta equations:

$$\begin{cases}
\dot{\phi}_{\mathrm{g}} = \dot{\phi}_{\mathrm{I}} + \frac{Q_{\mathrm{g}}-\mathcal{Q}}{C_1}\\
\dot{\phi}_{\mathrm{o}} = \dot{\phi}_{\mathrm{I}} - \frac{Q_{\mathrm{o}}+\mathcal{Q}}{C_2}.\\
Q_g + Q_I + Q_o = 0
\end{cases} \tag{D.2}$$

Achieving the expression of the SC Hamiltonian, obtained through the Legendre Transform of Lagrangian, requires some algebraic manipulations. Explicitly:

$$\begin{aligned}
\mathcal{H}(\vec{\phi},\vec{Q}) = \sum_{k\in[o,I,g]} &\left[Q_k\cdot\dot{\phi}_k(\vec{Q},\dot{\phi}_{\mathrm{I}})\right] - \mathcal{L} =\\
&Q_{\mathrm{g}}\left[\frac{Q_{\mathrm{g}}-\mathcal{Q}}{C_1}+\dot{\phi}_{\mathrm{I}}\right] + Q_{\mathrm{o}}\left[\frac{Q_{\mathrm{o}}+\mathcal{Q}}{C_2}+\dot{\phi}_{\mathrm{I}}\right]\\
&+ Q_{\mathrm{I}}\dot{\phi}_{\mathrm{I}} - \frac{1}{2C_1}\left(Q_{\mathrm{g}}-\mathcal{Q}\right)^2 - \frac{1}{2C_2}\left(Q_{\mathrm{o}}+\mathcal{Q}\right)^2\\
&- \mathcal{Q}\left[\frac{Q_{\mathrm{g}}-\mathcal{Q}}{C_1}+\dot{\phi}_{\mathrm{I}}\right] + \mathcal{Q}\left[\frac{Q_{\mathrm{o}}+\mathcal{Q}}{C_2}+\dot{\phi}_{\mathrm{I}}\right] + \mathcal{Q}V_{\mathrm{g}} + \mathcal{U}\\
&= \frac{1}{2C_1}\left(Q_{\mathrm{g}}-\mathcal{Q}\right)^2 + \frac{1}{2C_2}\left(Q_{\mathrm{o}}+\mathcal{Q}\right)^2 + \mathcal{Q}V_g + \mathcal{U}\\
&+ \left(Q_g+Q_o+Q_I\right)\dot{\phi}_I.
\end{aligned} \tag{D.3}$$

Recalling that from momenta Eqs. (3.17) holds that $\sum_{i=I,g,o} Q_i = 0$, the terms relating to $\dot{\phi}_{\mathrm{I}}$ vanishes as well from the Hamiltonian:

$$\mathcal{H} = \frac{1}{2C_1}\left(Q_{\mathrm{g}}-\mathcal{Q}\right)^2 + \frac{1}{2C_2}\left(Q_{\mathrm{o}}+\mathcal{Q}\right)^2 + \mathcal{Q}V_g + \mathcal{U}. \tag{D.4}$$

The circuital node o is grounded in such a way that its voltage can be neglected, i.e. $\phi_o = \dot{\phi}_o = \ddot{\varphi}_o = 0$. Thus, the role of such a node in the Hamiltonian can be neglected, also in force of the fact that the system in Eq.(D.2) is singular, signalling that one charge can be written in terms of the other two. Exploiting the third line in Eq.(D.2), the charge Q_o can be written as $Q_o = -(Q_g + Q_I)$. Applying the considerations done above about the node o, the changes of variables

$$\vec{Q} = (2e)\vec{n} = (2e)\begin{pmatrix} n_g \\ n_I \\ -(n_g + n_I) \end{pmatrix}, \tag{D.5}$$

$$\mathcal{Q} = (2e)\mathcal{N}, \tag{D.6}$$

$$\vec{\phi} = \frac{2\pi}{\Phi_0}\vec{\varphi} = \frac{2\pi}{\Phi_0}\begin{pmatrix} \varphi_g \\ \varphi_I \\ 0 \end{pmatrix}, \tag{D.7}$$

and the definitions of electron charging energy $E_{C_i} = \frac{e^2}{C_i}$ for $i = 1, 2$, the final expression of the SC Hamiltonian becomes

$$\begin{aligned} \mathcal{H} =& 4E_{C_1}(n_g - \mathcal{N})^2 + 4E_{C_2}(n_g + n_I + \mathcal{N})^2 \\ & - E_{J_1}\cos(\varphi_{\mathrm{g}} - \varphi_I) - E_{J_2}\cos(\varphi_I) + (2e\mathcal{N})V_{\mathrm{g}}. \end{aligned} \tag{D.8}$$

In the Hamiltonian formalism defined by Eq. (D) the variables $\vec{n}$ and $\vec{\varphi}$ are conjugated, just for the fact that they are a simple rescaling of the true conjugated variables $\vec{Q}$ and $\vec{\phi}$. It is convenient, in view of the subsequent derivation of Hamilton's equations, to recast properly the Poisson's brackets. Given two generic functions of the Hamiltonian variables, $f = f(\vec{\varphi}, \vec{n})$ and $g = g(\vec{\varphi}, \vec{n})$, their Poisson's bracket can be rewritten as

$$\{f, g\} = \sum_{i=g,I} \frac{\partial f}{\partial \phi_{\mathrm{i}}}\frac{\partial g}{\partial Q_{\mathrm{i}}} - \frac{\partial f}{\partial Q_{\mathrm{i}}}\frac{\partial g}{\partial \phi_{\mathrm{i}}} = \tag{D.9}$$

$$= \frac{1}{\hbar}\sum_{i=g,I} \frac{\partial f}{\partial \varphi_{\mathrm{i}}}\frac{\partial g}{\partial n_{\mathrm{i}}} - \frac{\partial f}{\partial n_i}\frac{\partial g}{\partial \varphi_{\mathrm{i}}}. \tag{D.10}$$

Consequently, the Hamilton's equations for the degree of freedom k become

$$\dot{n}_{\mathrm{k}} = \{n_{\mathrm{k}}, \mathcal{H}\} = -\frac{1}{\hbar}\frac{\partial \mathcal{H}}{\partial \varphi_{\mathrm{k}}}, \tag{D.11}$$

and

$$\dot{\varphi}_{\mathrm{k}} = \{\varphi_{\mathrm{k}}, \mathcal{H}\} = \frac{1}{\hbar}\frac{\partial \mathcal{H}}{\partial n_{\mathrm{k}}}. \tag{D.12}$$

Computing explicitly the Hamilton's equations The EOMs are easily derived through the redefined Poisson's bracket:

$$\begin{cases} \dot{n_g} = -\frac{E_{J_1}}{\hbar}\sin(\varphi_g - \varphi_I) \\ \dot{n_I} = \frac{E_{J_1}}{\hbar}\sin(\varphi_g - \varphi_I) - \frac{E_{J_2}}{\hbar}\sin(\varphi_I) \end{cases} \tag{D.13}$$

$$\begin{cases} \dot{\varphi}_{\mathrm{g}} = \frac{8E_{C_1}}{\hbar}(n_{\mathrm{g}} - \mathcal{N}) + \frac{8E_{C_2}}{\hbar}(n_I + n_g - \mathcal{N}) \\ \dot{\varphi}_{\mathrm{I}} = \frac{8E_{C_2}}{\hbar}(n_I + n_g - \mathcal{N}) \end{cases} \tag{D.14}$$

The explicit dependence of the EOMs on the rescaled Lagrangian multipliers $\mathcal{N}$ can be avoided by reintroducing the voltage constraint $\dot{\phi}_{\mathrm{g}} = V_{\mathrm{g}}$. Explicitly:

$$\begin{aligned} \frac{2\pi}{\phi_0}V_{\mathrm{g}} =& \dot{\varphi}_{\mathrm{g}} = \frac{8}{\hbar}[E_{C_\Sigma}n_{\mathrm{g}} + E_{C_2}n_I - E_{C_\Sigma}\mathcal{N}] \Longrightarrow \\ \mathcal{N} =& -\frac{(2e)V_{\mathrm{g}}}{8E_{C_\Sigma}} + n_g + \frac{E_{C_2}}{E_{C_\Sigma}}n_I, \end{aligned} \tag{D.15}$$

where $E_{C_\Sigma} = E_{C_1} + E_{C_2}$. Inserting the latter expression in Eqs. (3.26) the EOMs take the form

$$\begin{cases} \dot{\varphi}_{\mathrm{g}} = \frac{2\pi}{\Phi_0} V_g \\ \dot{\varphi}_I = \frac{2\pi}{\Phi_0} \frac{E_{C_2}}{E_{C_\Sigma}} V_{\mathrm{g}} + \frac{8 E_{C_1} E_{C_2}}{\hbar E_{C_\Sigma}} n_I. \end{cases} \tag{D.16}$$

The first EOM in Eq.(D.16) can be integrated

$$\dot{\varphi}_{\mathrm{g}} = \omega_{\mathrm{g}} \to \varphi_{\mathrm{g}}(t) = \varphi_{g0} + \omega_{\mathrm{g}} t, \tag{D.17}$$

where $\omega_{\mathrm{g}} = \frac{2\pi V_{\mathrm{g}}}{\Phi_0}$ The second EOM in Eq.(D.16) can be differentiated again with respect to the time, giving

$$\ddot{\varphi}_I = \frac{8 E_{C_1} E_{C_2}}{\hbar E_{C_S}} \dot{n}_I, \tag{D.18}$$

which, inserting the EOMs of the charge given by Eq.(D.13) and assuming that the two JJs are physically identical, i.e. their superconducting currents are essentially described by the same Josephson energy $E_{\mathrm{J}} = E_{\mathrm{J1}} = E_{\mathrm{J2}}$, becomes

$$\ddot{\varphi}_I = -\frac{8 E_{C_1} E_{C_2} E_J}{\hbar^2 E_{C_S}} \left[\sin\left(\varphi_{\mathrm{I}}\right) - \sin\left(\varphi_{\mathrm{g}} - \varphi_{\mathrm{I}}\right)\right]. \tag{D.19}$$

The expression within the square brackets simplified exploiting the trigonometric formula $\sin(\alpha) - \sin(\beta) = 2\cos\left(\frac{\alpha+\beta}{2}\right)\sin\left(\frac{\alpha+\beta}{2}\right)$, whereas the capacitance contribution in the prefactor can be recast as

$$\frac{E_{C_1} E_{C_2}}{E_{C_S}} = e^2 \left(\frac{1}{2C_{J1}} \cdot \frac{1}{2C_{J2}}\right)\left(\frac{1}{2C_{J1}} + \frac{1}{2C_{J2}}\right)^{-1} = \frac{e^2}{2(C_{J1} + C_{J2})} = E_C \tag{D.20}$$

Inserting all these arguments and recalling $\varphi_\Delta = \varphi_I - \frac{\varphi_{\mathrm{g}}}{2}$, the final version of the equation of the superconducting phase is written as

$$\ddot{\varphi}_\Delta = -2\Omega_J^2 \cos\left(\frac{\varphi_{\mathrm{g}}(t)}{2}\right)\sin(\varphi_\Delta) \tag{D.21}$$

recognizing the Josephson plasma frequency $\Omega_J = \frac{\sqrt{8 E_J E_C}}{\hbar}$.

It is convenient to recast the Eq. (D.21) in its dimensionless form. Considering that φ is already dimensionless, rescaling time is enough to achieve a dimensionless equation. The natural time length for rescaling is the period T_{g} of the oscillatory term $\cos(\frac{\omega_{\mathrm{g}}}{2} t)\sin(\varphi_\Delta)$, provided by the inverse of the frequency $T_{\mathrm{g}} = 2\frac{2\pi}{\omega_{\mathrm{g}}} = \frac{2\Phi_0}{V_{\mathrm{g}}}$. The explicit rescaling with dimensionless derivatives is

$$\tau = \omega t = 4\pi \cdot t / T_{\mathrm{g}} \tag{D.22}$$

$$\frac{\partial}{\partial t} \to \frac{\omega_{\mathrm{g}}}{2}\frac{\partial}{\partial \tau} \qquad \frac{\partial^2}{\partial t^2} \to \frac{\omega_{\mathrm{g}}^2}{4}\frac{\partial^2}{\partial \tau^2} \tag{D.23}$$

The application of the rescaling above to Eq. (D.21) gives

$$\frac{d^2}{d\tau^2}\left(\varphi_\Delta\right) = \bar{\epsilon}\cos(\tau)\sin(\varphi_\Delta), \tag{D.24}$$

where the rescaled parameter in front of the oscillatory term is defined as the dimensionless Josephson frequency

$$\bar{\epsilon} = 8\frac{\Omega_{\mathrm{J}}^2}{\omega_{\mathrm{g}}^2} = \frac{64E_{\mathrm{C}}E_{\mathrm{J}}}{(2e)^2V_{\mathrm{g}}^2}. \tag{D.25}$$

The latter is only a function of the external voltage V_{g}, given that the physical dimensions of the JJs fix all the other quantities.

Appendix E

RCSJ model

The RCSJ model introduces in the SC a resistive component which can model the emergence of some linear dissipation processes occuring in the JJs of the circuit, such as quasi-particle or thermal excitations. Thus, two resistors are joint in parallel with the canonical CJ representation of the JJs. The starting point of the mathematical treatment is that the two JJs are respectively crossed by the currents I_1 and I_2, each of which is then split into three different contributions: one is purely resistive, one is due to the capacitance and the last is the Josephson element's supercurrent. Recalling the Josephson relations (2.1) and (2.2), the super-currents have the expressions

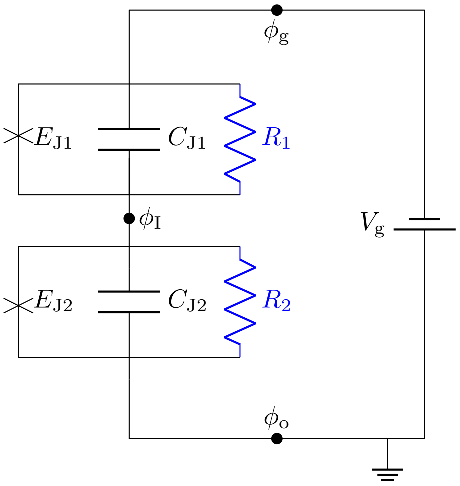

Figure E.1: RSCJ description of the voltage-biased series of two JJs depicted in Fig.D.1. To each JJ in the circuit is added a resistor to the capacitor-Josephson's element parallel.

$$I_{\mathrm{J1}} = I_{\mathrm{C1}} \sin\left(\varphi_{\mathrm{g}} - \varphi_{\mathrm{I}}\right), \tag{E.1}$$

$$I_{\mathrm{J2}} = I_{\mathrm{C2}} \sin\left(\varphi_{\mathrm{g}} - \varphi_{\mathrm{I}}\right), \tag{E.2}$$

while the current flowing through the capacitors

$$I_{C_1} = C_1\left(v_{\mathrm{g}} - v_{\mathrm{I}}\right) = \frac{\Phi_0}{2\pi} C_1\left(\ddot{\varphi}_{\mathrm{g}} - \ddot{\varphi}_I\right), \tag{E.3}$$

$$I_{C_2} = C_2\left(v_{\mathrm{I}} - v_{\mathrm{o}}\right) = \frac{\Phi_0}{2\pi} C_2\left(\ddot{\varphi}_I - \ddot{\varphi}_o\right), \tag{E.4}$$

$$\tag{E.5}$$

and the current through the resistors

$$I_{R_1} = \frac{1}{R_1}\left(v_{\mathrm{g}} - v_{\mathrm{I}}\right) = \frac{\Phi_0}{2\pi R_1}\left(\dot{\varphi}_{\mathrm{g}} - \dot{\varphi}_{\mathrm{I}}\right), \tag{E.6}$$

$$I_{R_2} = \frac{1}{R_2}\left(v_{\mathrm{g}} - v_{\mathrm{I}}\right) = \frac{\Phi_0}{2\pi R_2}\left(\dot{\varphi}_{\mathrm{I}} - \dot{\varphi}_{\mathrm{g}}\right). \tag{E.7}$$

$$\tag{E.8}$$

Summing up, the total currents flowing in the JJs are:

$$I_1 = I_{\mathrm{c}1}\sin\left(\varphi_{\mathrm{g}} - \varphi_{\mathrm{I}}\right) + \frac{\Phi_0}{2\pi R_1}\left(\dot{\varphi}_{\mathrm{g}} - \dot{\varphi}_I\right) + \frac{\Phi_0}{2\pi} C_1\left(\ddot{\varphi}_{\mathrm{g}} - \ddot{\varphi}_I\right) \tag{E.9}$$

$$I_2 = I_{\mathrm{c}1}\sin\left(\varphi_{\mathrm{I}} - \varphi_{\mathrm{o}}\right) + \frac{\Phi_o}{2\pi R_2}\left(\dot{\varphi}_I - \dot{\varphi}_{\mathrm{o}}\right) + \frac{\Phi_o}{2\pi} C_2\left(\ddot{\varphi}_{\mathrm{I}} - \ddot{\varphi}_{\mathrm{o}}\right) \tag{E.10}$$

The node o is grounded, $\varphi_{\mathrm{o}} = \dot{\varphi}_{\mathrm{o}} = \ddot{\varphi}_{\mathrm{o}} = 0$, giving that $\varphi_{\mathrm{g}}(t) = \varphi_{\mathrm{g}}(0) + \omega_{\mathrm{g}} t$. Since the two JJs are in series, the two currents have to be equal:

$$I_1 = I_2 \implies \tag{E.11}$$

$$\frac{4\pi^2}{\Phi_0^2} E_{\mathrm{J}}\left[\sin\left(\varphi_{\mathrm{g}} - \varphi_{\mathrm{I}}\right) - \sin\left(\varphi_{\mathrm{I}}\right)\right] + \frac{1}{R}\left(\dot{\varphi}_{\mathrm{g}} - 2\dot{\varphi}_I\right) - \left(C_{\mathrm{J}1} + C_{\mathrm{J}2}\right)\ddot{\varphi}_{\mathrm{I}} = 0, \tag{E.12}$$

Exploiting the trigonometric formula $\sin(\alpha) - \sin(\beta) = 2\cos\left(\frac{\alpha+\beta}{2}\right)\sin\left(\frac{\alpha+\beta}{2}\right)$ and defining $E_{\mathrm{C}} = \frac{e^2}{C_{J1} + C_{J2}}$

$$\ddot{\varphi}_{\mathrm{I}} = -2\frac{8E_{\mathrm{J}}E_{\mathrm{C}}}{\hbar^2}\cos\left(\frac{\varphi_{\mathrm{g}}}{2}\right)\sin\left(\varphi_{\mathrm{I}} - \frac{\varphi_{\mathrm{g}}}{2}\right) - \frac{2}{R(C_{\mathrm{J}1} + C_{\mathrm{J}2})}\left(\varphi_{\mathrm{I}} - \frac{\varphi_{\mathrm{g}}}{2}\right), \tag{E.13}$$

which can be finally recast in

$$\ddot{\varphi}_{\Delta} = -2\Omega_J^2\cos\left(\frac{\varphi_{\mathrm{g}}(t)}{2}\right)\sin\left(\varphi_{\Delta}\right) - \Gamma\dot{\varphi}_{\Delta}, \tag{E.14}$$

where the dissipative coefficient $\Gamma = \frac{2}{R(C_{\mathrm{J}1} + C_{\mathrm{J}2})}$. Time rescaling through Eqs. (D.22)-(D.23), the dissipative superconducting phase equation becomes

$$\frac{d^2\varphi_{\Delta}}{d\tau^2} = \bar{\epsilon}\cos(\tau)\sin(\varphi_{\Delta}) - \gamma\frac{d\varphi_{\Delta}}{d\tau} \tag{E.15}$$

Appendix F

Computational methods

A code written in Julia environment is used for the numerical simulation of Eq. (E.15), which corresponds to Eq. (5.1) in the main text. The timespan of the integration has been taken long in order for the dissipation to take place and eventually stabilize the solutions. Once the trajectories are obtained, the data related to the intermediate transient time are discarded, highlighting only the behavior of such trajectories in the long-time regime, where their specific attractors show up. From the numerical point of view, finding the attractor of a solution can be done by fixing some criteria, whose thresholds have been fixed empirically from direct observation trajectories in the phase-space. Thus, by choosing the threshold value for the phase $\varphi_{th} = 10^{-2}$ and for the phase derivative $\dot{\varphi}_{th} = 5 \cdot 10^{-3}$, the following criteria have been used for the classification of the solutions and implemented in the function `state_flag` in the code reported below:

- π-stable (label -3 in the code) : a solution for which $|\max \varphi_\Delta - \pi| < \varphi_{th}$ and $|\max \dot{\varphi}_\Delta| < \dot{\varphi}_{th}$;
- 0-stable (label -2 in the code): a solution for which $|\max \varphi_\Delta - 0| < \varphi_{th}$ and $|\max \dot{\varphi}_\Delta| < \dot{\varphi}_{th}$;
- cycle limit (label -1 in the code): a solution for which $|\max \varphi_\Delta - \pi| < \frac{\pi}{2}$ (or $|\max \varphi_\Delta| < \frac{\pi}{2}$ for limit-cycles around the downward fixed point) and $|\max \dot{\varphi}_\Delta| > \dot{\varphi}_{th}$;
- unstable (label -1 in the code): a solution for which $|\max \varphi_\Delta| > 2\pi$.

where $\max \dot{\varphi}_\Delta$ and $\max \varphi_\Delta$ are `valP` and `valV` in the code.

```
#= State_Type collects s (type of
asymptotic attractor) and f (number
of nods if its a cycle =#

mutable struct State_Type
    f::Int64
    s::Int64
end
```

```
# Classification
function state_flag(y::Vector{Float64},
yp::Vector{Float64}, epsilon_b::Real,
phi_I0::Real, t::Vector{Float64})
    #= classification of points =#
    #= state flag, depending on the solution type=#
    valP = maximum(y)
    valV = maximum(yp)
    State_fl = State_Type(0, 0)
    if abs(valP) > 2
        #=unstable solution=#
        State_fl.f = -3
        State_fl.s = -3
    elseif (abs(valV) > 5e-3) & (abs(valP - 1) < 1 / 2)
        #= cyclic solution =#
        cycl = cyclezeros(t, y, yp, epsilon_b, phi_I0)
        State_fl.f = cycl
        State_fl.s = 1
    elseif (abs(valV) < 5e-3) & (abs(valP - 1) < 1e-2)
        #=pi-stable=#
        State_fl.f = -1
        State_fl.s = -1
    else
        #=0-stable=#
        State_fl.f = -2
        State_fl.s = -2
    end
    return State_fl
end
```

The output of the function is a variable defined through the struct `State_Type`, having fields `.s` (attractor label) and `.f` (number of nods if the solution is a limit-cycle or the attractor label otherwise). At the first stage, the classification criteria have been applied to a set of solutions coming from a parameters space composed by 1024 × 1024 points $(\varphi_\Delta(0), \bar{\epsilon})$, where $\varphi_\Delta(0) \in [\frac{\pi}{2}, \pi]$ and $\bar{\epsilon} \in [0.01, 0.6]$. Such a large number of simulations have been chosen because the higher the number of labelled solutions, i.e. the larger the number of parameters space's points, the better the resolution and the accuracy of the stability diagram. However, computing such a high number of integrations could be computationally costly. Thus, since the chosen parameters space is comprised of almost 10^6 simulations, an optimized computational method has been implemented to, at least slightly, reduce the computational cost of the simulations. Step zero of this procedure is integrating a 2 × 2 square parameters space composed by couples $(\varphi_\Delta(0), \bar{\epsilon})$ taking as values the edges of the intervals of the definition of the parameters. Then, the first step is to bisect each of the two parameters' intervals, generating one more point in addition to the extreme ones already present, giving a 3 × 3 parameters space and a stability diagram composed of 9 points, where exactly 4 of them have been already integrated in the previous step of the procedure: the bisection can be repeated at each subsequent step, until the parameters space of 1024 × 1024 points is produced and a accurate stability diagram is obtained. At the generic n_{th} step of this procedure, the parameters space has a length $\delta_n = 1+2^n$ and the number of new integrations scales as $\Delta_n = 2^n\left(1+\frac{3}{4}2^n\right),\ n \geq 2$. From the latter expression, it is possible to see that the number of integrations still grows exponentially with the number of steps. Still, the implemented method can avoid performing one-quarter of the calculations needed with a naive method: this can be shown by computing the ratio between the integration performed at each step in the two methods $\simeq \frac{4}{3}\left[1+\frac{2}{3}2^{-n}\right]$. Figures 5.5 and 5.6 are the stability diagrams resulting from the abovementioned procedure, whereas the stability diagram reported in Fig. F.1 represents several steps of the optimized numerical method.

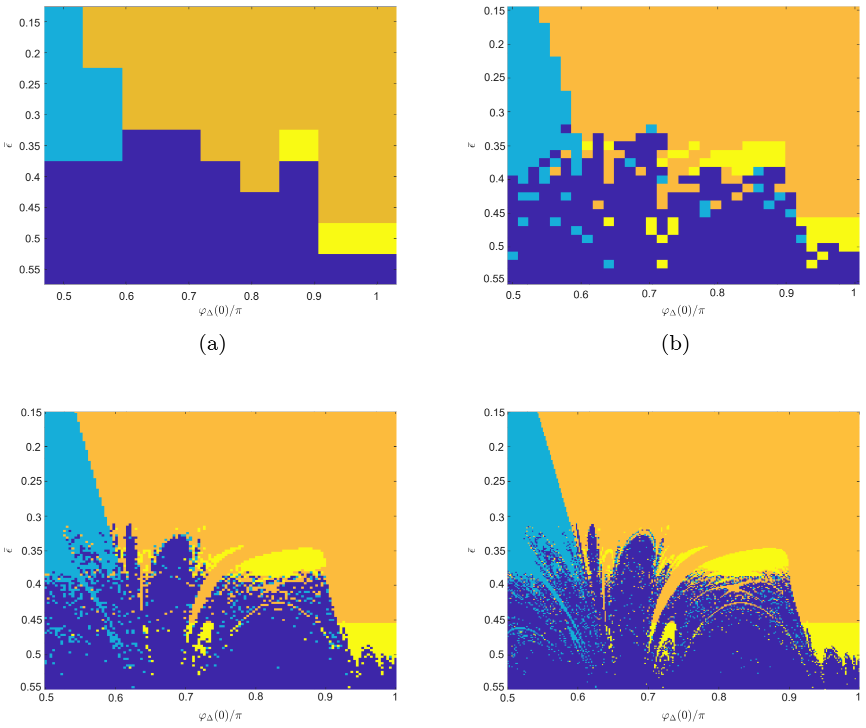

(a)

(b)

(c)

(d)

Figure F.1: Four different steps of the optimized method to obtain the stability diagram having a parameters space of 1024 × 1024 points, in Fig. 5.5. These stability diagrams have parameters space (a) 8 × 8, (b) 32 × 32, (c) 128 × 128 and (d) 256 × 256. The resolution of the attractors region increases when the parameters space points are increased.

What has been done then, is to investigate the multiple-nodding behavior of the limit-cycles emerging from the dynamical equation. It is worth recalling that a nod, in the definition of this work, is a point in the phase-space in which the trajectory has zero-derivative. In particular, the function `state_flag` recalls another function, called `cyclezeros`, which carries out two tasks: first, it computes the period of the cyclic oscillation and, second, it counts the total number of nods $2n$ within this period.

```
#=function that determines the
number of "nods",
first the period of the function T, then finds
the number of zeros in one period
(tfinal-T to tfinal)=#

function cyclezeros(t::Vector{Float64}, y::Vector{Float64},
                    yp::Vector{Float64}, epsilon_b::Real,
                    phi_I0::Real)

    pi = 3.1415
    y = pi .* y
    dt = t[2] - t[1]
    fty = FT(y .- Statistics.mean(y), t[end] - t[1], dt)
    ftpks=Peaks.argmaxima(fty.A[round(Int64, end / 2)+1:end])
    #= find maxima in the second half of the
    fourier transform =#

    idxft,valsft =
    Peaks.peakproms(ftpks,fty.A[round(Int64, end / 2)+1:end];
    minprom=1)
    #= idxft position of peaks, valsft
    the prominence =#

    if (idxft[1] == 2) #=eliminates a spurious peak
    near \omega=0 =#
        idxft = idxft[2:end]
    end

    adiacent = [idxft[1] - 10, idxft[1] + 10]
    Th = 2 * pi / fty.w[round(Int64, end / 2) + adiacent[1]]
    Tl = 2 * pi / fty.w[round(Int64, end / 2) + adiacent[2]]
    idxT = [round(Int64, Tl / dt), round(Int64, Th / dt)]
    #= upper and lower bound of the period =#

    idx = []
    for i in 1:length(adiacent)
        try
            idx1 = findall(isless.(0.5, abs.(gradN(convert.(
            Int64, isless.(0, yp[end-idxT[i]:end])))))
            .& isless.(abs.(yp[end-idxT[i]:end]), 5e-2))
            #= findall finds all the true =#
            push!(idx, length(idx1))
        catch
            println("epsilon_b=", epsilon_b,
            " phi_I0=", phi_I0, " idx=", idx)
        end
    end
    return sum(idx) / 2
    #= returnig the average between upper
```

```
    and lower estimation =#
end
```

The first block of the function computes the Fast Fourier Transform of the discrete mean-centred trajectory $\varphi_\Delta(t) - \bar{\varphi}_\Delta$

$$\varphi_\Delta(\omega) = \sum_{t=0}^{t_{end}} \left(\varphi_\Delta(t) - \bar{\varphi}_\Delta\right) e^{-i\omega t}. \tag{F.1}$$

The frequency spectrum of the trajectories exhibits several components which represent all the harmonic of the oscillations. Among all of them, the positive peak ω^* is related to the full-oscillation period $T^* = \frac{\omega^*}{2\pi}$. In order to increase the accuracy in the period determination, two equidistant symmetric peaks arounf the prominence are selected, giving respectively an upper and lower bound `Th` and `Tl` of the true period T^*. The second block counts the phase-space points having a zero derivative `yp` with a tolerance of $\simeq 5 \times 10^{-2}$: this essentially measures the nods number of the trajectories for the upper and lower periods. The output of the function is then the average of this two estimated numbers.

The estimation of Hausdorff's dimensions of the attractors regions and limit-cycles subregions in the stability diagrams in Figs. 5.6-5.7 have been implemented through the numerical function `fractal_dimension`, where the process of counting of boxes covering the border is repeated up to the limit imposed by finit resolutions, i.e. the last counting step involves `subreg` comprised of 4 points of the stability diagram. The stability is converted in a binary map, having 1 in the point where there is the desired attractor and 0 in all the other cases. The counting criterion sum over all the boxes in which at least one point is labelled by 1, i.e. region where all the points are ones or zeros are inside the regions and not at the borders.

```
function fractal_dimension(region, cycle)
#=It computes the number of boxes crossing the border
in function of the scale
scale = number of interval in which both axis
are divided =#

scale_iniy = 2 #largest boxes' size
scale_finy = round(Int64, 2049/2)
#= smallest boxes' size =#

function count_boxes(scale)

    X = round.(Int64, LinRange(1,2049, scale))

    N_boxes = 0
    for i in 1:length(X)-1
        for j in 1:length(X)-1
            subreg = view(region, X[i]:X[i+1],
                                  X[j]:X[j+1])
            if 1 in subreg && 0 in subreg
                #= only boxes in which there
                are both 1s and 0s belong
```

```
                    to the border =#
                    N_boxes += 1
                end
            end
        end
        return N_boxes
    end

    scale = collect(scale_iniy:2:scale_finy)
    number_boxes = count_boxes.(scale)

    return scale, number_boxes
end
```

In conclusion, the plots of the linear best fit for the estimation of the Hausdorff's dimension of the attractors — 0-stable, π-stable, unstable and limit-cycle — regions are reported in Fig.F.2-F.3.

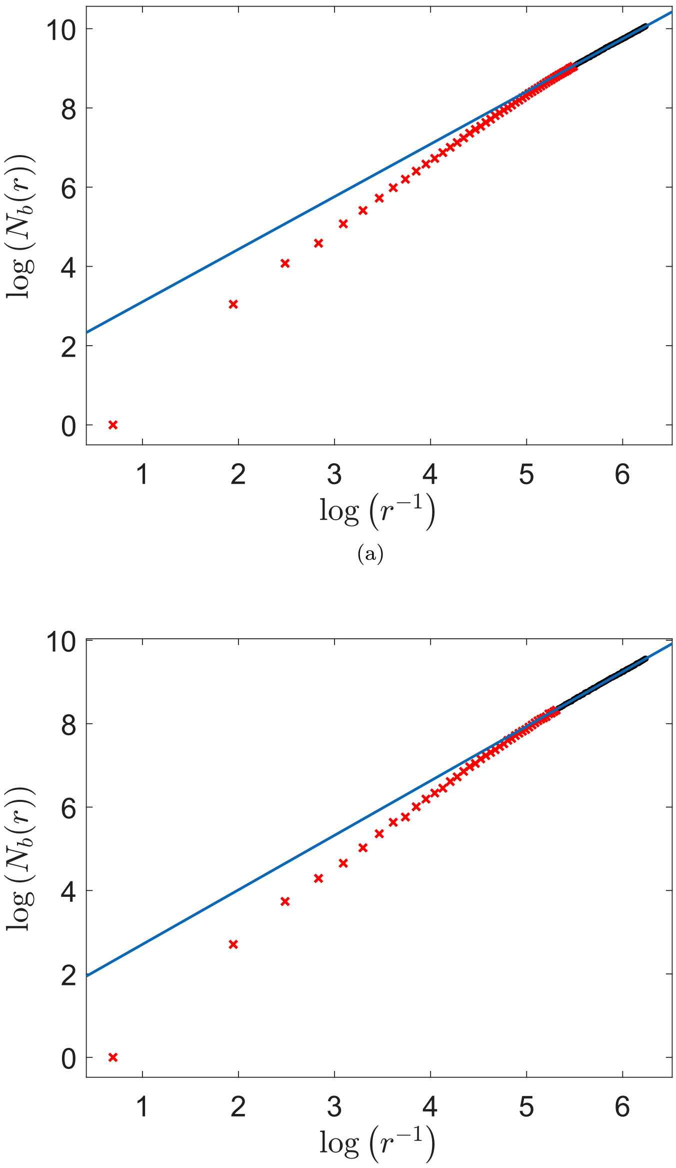

(a)

(b)

Figure F.2: Determination of the fractal dimensions via linear best fits (blue lines) of the 0-stable and π-stable regions in Fig. 5.6. The different linear fits correspond to (a)$[\log\left(\mathcal{N}_{\mathcal{B}}(r)\right)] = 1.327\left[\log\left(r^{-1}\right)\right] + 1.778$ for $0-$stable solutions, (b) $[\log\left(\mathcal{N}_{\mathcal{B}}(r)\right)] = 1.307\left[\log\left(r^{-1}\right)\right] + 1.402$ for $\pi-$stable solutions.

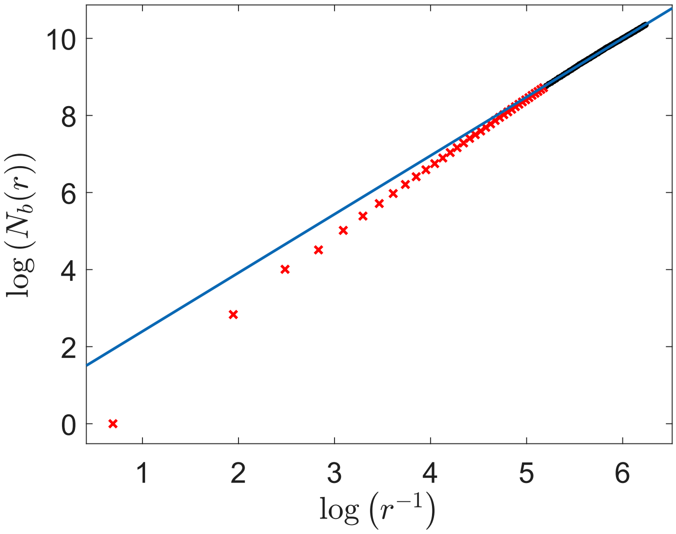

(a)

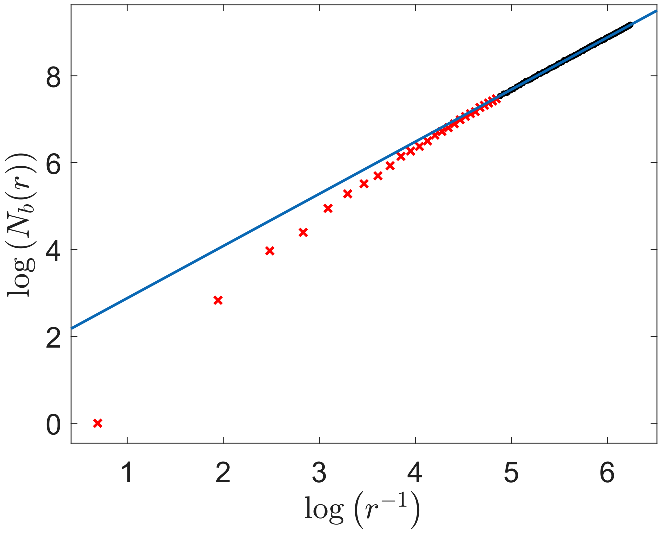

(b)

Figure F.3: Determination of the fractal dimensions via linear best fits (blue lines) of the unstable and limit-cycle regions in Fig. 5.6. The different linear fits correspond to (a) $[\log(\mathcal{N}_{\mathcal{B}}(r))] = 1.520\left[\log\left(r^{-1}\right)\right] + 0.876$ for unstable solutions, (b) $[\log(\mathcal{N}_{\mathcal{B}}(r))] = 1.201\left[\log\left(r^{-1}\right)\right] + 1.679$ for limit-cycle solutions.

Bibliography

D. Acheson. Multiple-nodding oscillations of a driven inverted pendulum. *Proceedings of the Royal Society of London. Series A: Mathematical and Physical Sciences*, 448(1932):89–95, 1995.

Y. Aharonov and D. Bohm. Significance of electromagnetic potentials in the quantum theory. *Physical Review*, 115(3):485, 1959.

V. Ambegaokar and A. Baratoff. Tunneling between superconductors. *Physical Review Letters*, 10(11):486, 1963.

F. Arute, K. Arya, R. Babbush, D. Bacon, J. C. Bardin, R. Barends, R. Biswas, S. Boixo, F. G. Brandao, D. A. Buell, et al. Quantum supremacy using a programmable superconducting processor. *Nature*, 574(7779):505–510, 2019.

J. Bardeen, L. N. Cooper, and J. R. Schrieffer. Theory of superconductivity. *Physical review*, 108(5):1175, 1957.

M. Bartuccelli, G. Gentile, and K. Georgiou. On the dynamics of a vertically driven damped planar pendulum. *Proceedings of the Royal Society of London. Series A: Mathematical, Physical and Engineering Sciences*, 457(2016):3007–3022, 2001.

M. V. Bartuccelli, G. Gentile, and K. V. Georgiou. On the stability of the upside-down pendulum with damping. *Proceedings: Mathematical, Physical and Engineering Sciences*, 458(2018):255–269, 2002. URL `http://www.jstor.org/stable/3067344`.

J. A. Blackburn, M. Cirillo, and N. Grønbech-Jensen. A survey of classical and quantum interpretations of experiments on josephson junctions at very low temperatures. *Physics Reports*, 611:1–33, 2016.

A. Blais, S. M. Girvin, and W. D. Oliver. Quantum information processing and quantum optics with circuit quantum electrodynamics. *Nature Physics*, 16 (3):247–256, 2020.

V. Bouchiat, D. Vion, P. Joyez, D. Esteve, and M. Devoret. Quantum coherence with a single cooper pair. *Physica Scripta*, 1998(T76):165, 1998.

E. I. Butikov. Subharmonic resonances of the parametrically driven pendulum. *Journal of Physics A: Mathematical and General*, 35(30):6209, 2002.

E. I. Butikov. An improved criterion for kapitza's pendulum stability. *Journal of Physics A: Mathematical and Theoretical*, 44(29):295202, 2011.

R. M. Carbo, R. W. Smith, and M. E. Poese. Stability of the parametrically excited damped inverted pendulum: Theory and experiment. *The Journal of the Acoustical Society of America*, 128(4):1623–1631, 2010.

F. S. Cataliotti, S. Burger, C. Fort, P. Maddaloni, F. Minardi, A. Trombettoni, A. Smerzi, and M. Inguscio. Josephson junction arrays with bose-einstein condensates. *Science*, 293(5531):843–846, 2001.

I. Chiorescu, Y. Nakamura, C. M. Harmans, and J. Mooij. Coherent quantum dynamics of a superconducting flux qubit. *Science*, 299(5614):1869–1871, 2003.

S. K. Dana, D. C. Sengupta, and K. D. Edoh. Chaotic dynamics in josephson junction. *IEEE Transactions on Circuits and Systems I: Fundamental Theory and Applications*, 48(8):990–996, 2001.

T. Duty, D. Gunnarsson, K. Bladh, and P. Delsing. Coherent dynamics of a josephson charge qubit. *Physical Review B*, 69(14):140503, 2004.

R. Fagaly. Superconducting quantum interference device instruments and applications. *Review of scientific instruments*, 77(10), 2006.

H. Fröhlich. Theory of the superconducting state. i. the ground state at the absolute zero of temperature. *Physical Review*, 79(5):845, 1950.

V. L. Ginzburg, V. L. Ginzburg, and L. Landau. *On the theory of superconductivity*. Springer, 2009.

S. M. Girvin. Superconducting qubits and circuits: Artificial atoms coupled to microwave photons. *Lectures delivered at Ecole d'Eté Les Houches*, 2011.

T. Golod, A. Rydh, and V. M. Krasnov. Application of nano-scale josephson junction as phase sensitive detector for analysis of vortex states in mesoscopic superconductors. *Physica C: Superconductivity*, 470(19):890–892, 2010.

X. Gu, A. F. Kockum, A. Miranowicz, Y.-x. Liu, and F. Nori. Microwave photonics with superconducting quantum circuits. *Physics Reports*, 718:1–102, 2017.

E. Gwinn and R. Westervelt. Fractal basin boundaries and intermittency in the driven damped pendulum. *Physical Review A*, 33(6):4143, 1986.

L. N. Hand and J. D. Finch. *Analytical mechanics*. Cambridge University Press, 1998.

T. T. Heikkilä. *The physics of nanoelectronics: transport and fluctuation phenomena at low temperatures*, volume 21. Oxford University Press, USA, 2013.

M. Hita-Pérez, G. Jaumà, M. Pino, and J. J. García-Ripoll. Three-josephson junctions flux qubit couplings. *Applied Physics Letters*, 119(22), 2021.

F. Hoehne, Y. A. Pashkin, O. V. Astafiev, M. Möttönen, J. P. Pekola, and J. Tsai. Coherent superconducting quantum pump. *Physical Review B*, 85 (14):140504, 2012.

M. Iansiti, Q. Hu, R. Westervelt, and M. Tinkham. Noise and chaos in a fractal basin boundary regime of a josephson junction. *Physical review letters*, 55(7): 746, 1985.

B. D. Josephson. Possible new effects in superconductive tunnelling. *Physics letters*, 1(7):251–253, 1962.

P. L. Kapitza. Dynamic stability of the pendulum with vibrating suspension point. *Sov. Phys. JETP*, 21(5):588–597, 1951. doi: 10.3367/UFNr.0044.195105b.0007. URL `https://ufn.ru/ru/articles/1951/5/b/`.

S.-Y. Kim and B. Hu. Bifurcations and transitions to chaos in an inverted pendulum. *Physical Review E*, 58(3):3028, 1998.

J. Koch, M. Y. Terri, J. Gambetta, A. A. Houck, D. I. Schuster, J. Majer, A. Blais, M. H. Devoret, S. M. Girvin, and R. J. Schoelkopf. Charge-insensitive qubit design derived from the cooper pair box. *Physical Review A*, 76(4):042319, 2007.

A. F. Kockum and F. Nori. Quantum bits with josephson junctions. *Fundamentals and Frontiers of the Josephson Effect*, pages 703–741, 2019.

L. D. Landau and E. Lifschic. *Course of theoretical physics. vol. 1: Mechanics.* Oxford, 1978.

F. London and H. London. The electromagnetic equations of the supraconductor. *Proceedings of the Royal Society of London. Series A-Mathematical and Physical Sciences*, 149(866):71–88, 1935.

J. M. Martinis. Superconducting phase qubits. *Quantum information processing*, 8:81–103, 2009.

J. M. Martinis, S. Nam, J. Aumentado, and C. Urbina. Rabi oscillations in a large josephson-junction qubit. *Physical review letters*, 89(11):117901, 2002.

P. Martinoli and C. Leemann. Two dimensional josephson junction arrays. *Journal of Low Temperature Physics*, 118:699–731, 2000.

W. Meissner and R. Ochsenfeld. Ein neuer effekt bei eintritt der supraleitfähigkeit. *Naturwissenschaften*, 21(44):787–788, 1933.

M. A. Nielsen and I. L. Chuang. *Quantum computation and quantum information.* Cambridge university press, 2010.

A. O. Niskanen, J. P. Pekola, and H. Seppä. Fast and accurate single-island charge pump: Implementation of a cooper pair pump. *Physical review letters*, 91(17):177003, 2003.

A. O. Niskanen, J. M. Kivioja, H. Seppä, and J. P. Pekola. Evidence of cooper-pair pumping with combined flux and voltage control. *Physical Review B*, 71 (1):012513, 2005.

T. Orlando, J. Mooij, L. Tian, C. H. Van Der Wal, L. Levitov, S. Lloyd, and J. Mazo. Superconducting persistent-current qubit. *Physical Review B*, 60 (22):15398, 1999.

H. Paik, D. I. Schuster, L. S. Bishop, G. Kirchmair, G. Catelani, A. P. Sears, B. Johnson, M. Reagor, L. Frunzio, L. I. Glazman, et al. Observation of high coherence in josephson junction qubits measured in a three-dimensional circuit qed architecture. *Physical Review Letters*, 107(24):240501, 2011.

Y. A. Pashkin, O. Astafiev, T. Yamamoto, Y. Nakamura, and J. Tsai. Josephson charge qubits: a brief review. *Quantum Information Processing*, 8:55–80, 2009.

D. Pegg and S. Barnett. Phase properties of the quantized single-mode electromagnetic field. *Physical Review A*, 39(4):1665, 1989.

J. P. Pekola, O.-P. Saira, V. F. Maisi, A. Kemppinen, M. Möttönen, Y. A. Pashkin, and D. V. Averin. Single-electron current sources: Toward a refined definition of the ampere. *Reviews of Modern Physics*, 85(4):1421, 2013.

R. Sobolewski, D. R. Dykaar, T. Y. Hsiang, C. Vanneste, and C.-C. Chi. Chaos in pulse-driven josephson junctions. *Physical Review B*, 37(7):3778, 1988.

M. Steffen, M. Ansmann, R. McDermott, N. Katz, R. C. Bialczak, E. Lucero, M. Neeley, E. M. Weig, A. N. Cleland, and J. M. Martinis. State tomography of capacitively shunted phase qubits with high fidelity. *Physical Review Letters*, 97(5):050502, 2006.

A. Stephenson. Xx. on induced stability. *The London, Edinburgh, and Dublin Philosophical Magazine and Journal of Science*, 15(86):233–236, 1908. doi: 10.1080/14786440809463763. URL `https://doi.org/10.1080/14786440809463763`.

L. Susskind and J. Glogower. Quantum mechanical phase and time operator. *Physics Physique Fizika*, 1(1):49, 1964.

D. Tomaszewski, P. Busz, R. López, M. Lee, J. Martinek, et al. Aharonov-bohm and aharonov-casher effects in a double quantum dot josephson junction. *Physical Review B*, 98(17):174504, 2018.

D. Vion, A. Aassime, A. Cottet, P. Joyez, H. Pothier, C. Urbina, D. Esteve, and M. H. Devoret. Manipulating the quantum state of an electrical circuit. *Science*, 296(5569):886–889, 2002.

U. Vool and M. Devoret. Introduction to quantum electromagnetic circuits. *International Journal of Circuit Theory and Applications*, 45(7):897–934, 2017.

A. Wallraff, D. I. Schuster, A. Blais, L. Frunzio, R.-S. Huang, J. Majer, S. Kumar, S. M. Girvin, and R. J. Schoelkopf. Strong coupling of a single photon to a superconducting qubit using circuit quantum electrodynamics. *Nature*, 431(7005):162–167, 2004.

C. Wasshuber. *About single-electron devices and circuits.* PhD thesis, 1997.

G. Wendin. Quantum information processing with superconducting circuits: a review. *Reports on Progress in Physics*, 80(10):106001, 2017.

L. Zhang, L. Cai, and C. Feng. Quantitative calculation and bifurcation analysis of periodic solutions in a driven josephson junction including interference current. *Physica C: Superconductivity*, 471(5-6):150–155, 2011.